AN ABSTRACT OF THE DISSERTATION OF

Hossein Faraji for the degree of Doctor of Philosophy in Robotics and Mechanical Engineering presented on November 28, 2018.

Title: Geometric Motion Planning for Inertial Systems

Abstract approved: ____

Ross L. Hatton

The locomotion of robotic systems is often complex. In order to enable better visualization and understanding of the effect of the robot's geometry and inertia on the robot's trajectories, this thesis proposes to use geometric mechanics to bridge the gap between the physical motion of a robot and its mathematical structure. The main focus of this research is to investigate the system geometry and inertia and their relationship with the curves and acceleration that produce the most efficient trajectories or gaits. This thesis' approach has an advantage over the state-of-the-art method, which uses numerical forward dynamic simulations. Such numerical simulations are computationally expensive and dependent on starting parameters. The proposed geometric motion planning framework allows the user to design a trajectory with respect to the requirements without any need for forward simulation. Furthermore, the proposed framework enables the user to understand the system's movement from its mathematical model rather than computing the

results and exploring the outputs. Unlike previous works that were focusing on the system geometry to gain insight about the system's movement, this thesis uses the geometry and inertia to describe the system's movement. This is achieved using two tools to gain insight into the underlying locomotion: constructing *geodesics* and constructing *metric fields*. The geodesic illustrates the robots geometric structure of the natural dynamic path which is defined as the straightest path. The metric field in mechanical systems is obtained from the system's inertia which illustrates where it is easier to move in parameterized space. In this research we consider four classes of systems: (1) fixed base systems such as robotic arms, (2) crawling systems in an inertial based environment such as floating snakes, (3) flying object with abrupt change in momentum such as casting manipulator, and (4) system with fast energy release such as jumping robots.

Geometric Motion Planning for Inertial Systems

by

Hossein Faraji

A DISSERTATION

submitted to

Oregon State University

in partial fulfillment of
the requirements for the
degree of

Doctor of Philosophy

Presented November 28, 2018
Commencement June 2019

Doctor of Philosophy dissertation of Hossein Faraji presented on November 28, 2018.

APPROVED:

Major Professor, representing Robotics and Mechanical Engineering

---

Director of the School of Mechanical, Industrial and Manufacturing Engineering

---

Dean of the Graduate School

Hossein Faraji, Author

ACKNOWLEDGEMENTS

I would like to express my sincere gratitude to my advisor Prof. Ross L. Hatton for the continuous support of my PhD study and related research, for his patience, motivation, and immense knowledge. His guidance helped me in all the time of research and writing of this dissertation. I could not have imagined having a better advisor and mentor for my PhD study. I also would like to thank my lovely parents for supporting me spiritually throughout my whole PhD.

TABLE OF CONTENTS

Page

TABLE OF CONTENTS (Continued)

Page

TABLE OF CONTENTS (Continued)

LIST OF FIGURES

LIST OF FIGURES (Continued)

LIST OF FIGURES (Continued)

LIST OF FIGURES (Continued)

Figure | Page

LIST OF FIGURES (Continued)

LIST OF APPENDIX FIGURES

Chapter 1: Introduction

In locomotive path planning, many methods exist for trajectory optimization. The focus of these optimizers is to introduce a precise, fast and easy-to-implement method finding the system's optimal trajectory according to a particular metric. [3, 4, 5, 6]. However, in these optimizers the trajectory integration is treated as a black box and don't provide an intuitive understanding on how the movement are related to the system's mechanical features including mass, mass distribution, and moment of inertia.

To understand the movement characteristics of the system, we need to know the natural dynamic path of that system. The natural dynamic path is important because a robot uses the least energy along that path. The geodesic illustrates the geometric structure of the natural dynamic path which is defined as the straightest path. The shape of the natural dynamic path depends on the system's inertia where inertia is the resistance of any physical objects to any change of its current state (including change in speed and its direction). The ultimate goal in this research is to use the concepts of inertia and geodesic to provide an intuitive understanding of a robot's motion by creating a link between its physical motion and the fundamental mathematical structure [7]. Intuition about the physics of the system can help the user quickly design a path or gait for the robot in a short time. Intuition about the physics also helps the user to understand the

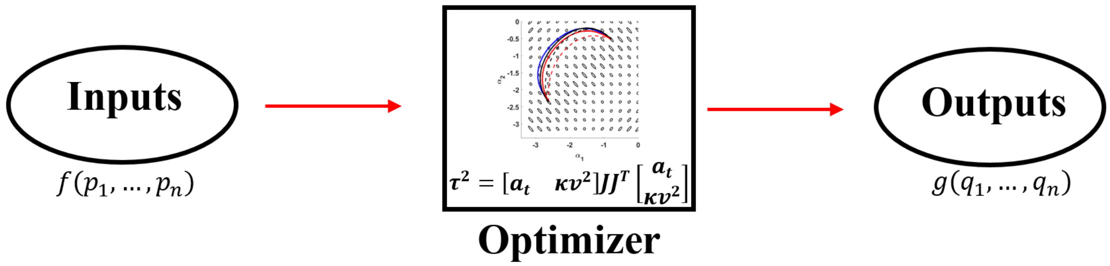

Figure 1.1: Proposed framework provides an intuitive understanding between mathematical structure and the robot's motion for inertial systems, by defining the complex equations in fewer and meaningful terms.

relationship between system's movement characteristics and mechanical properties of the system. Furthermore, it provides the understanding of the solution structure of the optimal trajectory.

This thesis approach provides an advantage over the state-of-the-art method for trajectory generation. Specifically, the current method to understand a system is to change a variable in the input of optimizer, compute the system's equations, evaluate the outputs, and repeat this process over and over. [8, 9, 10, 11, 12]. This process is tedious and computationally expensive and won't provide an complete view of the system's movement. Unlike existing methods in motion planning, the focus of our proposed method is to provide an intuition of the relationship between the geometry and inertia of the system and the optimum way of moving. Therefore, the user can design a trajectory and observe the effectiveness of different gait patterns without integrating the complete dynamics (Fig. 1.1).

Overall, prior works including our own work have only considered trajectory generation for non-inertial systems and that is only for systems called moving base system in viscous environments [13]. Specifically, in the moving base systems, the robot's locations in state space don't matter. In the fixed base systems, the robots location is fixed and the end effector's trajectory between two points is important (manipulator arms robots). Part of the reason they did not consider the robots with a fixed base is because, their focus was on systems interacting in drag dominated environment due to the simplicity of equations. Therefore, there have been limited works explicitly dealing with inertial systems. This thesis goes beyond the state-of-the-art by considering the inertia for moving base and fixed base systems.

In this context, there are some unanswered questions that this thesis will focus on:

- How does the optimal curve for inertial systems depend on a system's geometry? How is it different from systems in viscous environments?
- How does a system with a fixed base move when the end effector is constrained to move between two points? What is the structure for the optimal solution?
- How does the geometry and inertia of a system help us to predict a bounce in impact dynamics problems?
- How does the system geometry in jumping robots channel the fast energy release in a desired direction?

This thesis addresses these questions by introducing a mathematical framework for gaining intuition of system's motion with two key features. The first feature is that the framework should work regardless of the robot's morphology. The second feature is that it should clarify the relationship between the mathematical structure and the physical motion of a robot. We argue that the second aspect is crucial and helps the user generate a trajectory according to the need.

The approach to achieve these features will include three steps. The first step is to develop insight of what inertia means for mechanical systems. Specifically while, we have a good understanding of how inertia behaves on a point mass object and can predict its motion, when the object is more complex such as a robot, our understanding is much more limited. The second step is to develop the concept of a minimum energy path using the geodesic curvature which provides a physically meaningful interpretation of the natural dynamic path with respect to the inertia. The third step is to use the concept of the geodesic path and inertia to generate a minimum torque-squared path which provides an intuitive understanding of the minimum torque with respect to the acceleration and curvature of the path. The scope of the thesis is to develop this framework and focus on four classes of systems: robotics arms, crawling robots, casting manipulators and jumping robots. First, we investigate the optimal trajectory solution for robotics arm in which one end of the robot is fixed and only the trajectory of the end-effector is important. Second, we consider the locomotion of the systems that use the environment to create reaction forces to push their body forward such as high Reynolds snake robots where the effect of inertia is important. Then we consider the casting manipulator robots that can control the end-effector by changing end-effector momentum by the tether attached to it. Finally, we consider systems with fast energy release such as jumping robots in which jumping is an efficient locomotion over rough terrain. It can be also considered as launching at a target.

The main contributions of this work are listed below:

- **Contribution 1**: Developed an inertia based insight that describes the most efficient gaits and trajectories of the system.
- **Contribution 2**: Developed an inertia-based geometric motion planning gait optimizer for inertial crawling systems such as the floating snake.
- **Contribution 3**: Developed a framework for impact controllability based on systems geometry and inertia.
- **Contribution 4**: Developed a model prediction framework for impact dynamic on flying object.
- **Contribution 5**: Developed an inertia-based geometric motion planning tool for the class of jumping robots with fast energy release such as jumping spider.

The structure of this dissertation is as follows:

- *Chapter 2*: The structure of natural dynamic path from a geometric mechanics point of view as well as the effect of inertia on robot's movement are considered.
- *Chapter 3*: A trajectory motion planning for fix based systems such as manipulator's arms are considered. The torque equation is derived as a function

of curvature and acceleration to be related to the geodesic path to create a pattern for optimal trajectories between two given points.

- *Chapter 4*: The geometric motion planning from the last chapter is extended to be suitable for moving based systems where the displacement of the robot is also important.

- *Chapter 5*: The concept of inertia and natural dynamic is used to develop a framework for bounce prediction in impact dynamics problems.

- *Chapter 6*: The effect of inertia and geometry of a jumping spider is studied for the targeted jump.

- *Chapter 7*: Snake robot locomotion over granular surfaces via an empirical-geometric approach that is amenable to analysis and optimization is considered.

Chapter 2: Background

This chapter covers the concept of passive dynamics path from a geometric mechanics point of view and geometrically illustrates the terms in dynamic equations. We use the two fundamental concepts in differential geometry to gain insight into the underlying motion of the system: *geodesics* and *metric fields*. The geodesic illustrates the robots geometric structure of the natural dynamic path which is defined as the straightest path. The metric field in mechanical systems is obtained from the system's inertia which illustrates where it is easier to move in parameterized space. Using these concepts, we develop a cost function that describes the natural dynamic path in meaningful mathematical terms which can be easily visualized.

2.1 Passive-Dynamic Path

The standard equations of motion for a system with inertial dynamics are

$$\tau = M(q)\ddot{q} + C(\dot{q}, q)\dot{q}, \tag{2.1}$$

where M is the inertia matrix, q is the vector of generalized coordinates, and C is the centrifugal and coriolis matrix. The natural dynamic trajectories for this system are those for which no torque is applied to the system, and the configuration evolves along the differential equation

$$\ddot{q} = M(q)^{-1}C(\dot{q}, q)\dot{q} \tag{2.2}$$

for given initial conditions.

If the configuration space is shaped into a surface such that a point mass moving on the surface has the same kinetic energy as the system moving with the corresponding parameter trajectory, then the torque-free motions are the geodesics of the surface, moving with constant speed and without "turning" except to follow the surface. The geometry of this surface is defined by the mass matrix M (which serves as its *metric tensor*), with the curvature of the surface encoded in the partial derivatives of M with respect to the configuration variables.

Geodesics are the generalization of Euclidean straight lines to arbitrarily shaped manifolds (spaces which may have intrinsic curvature) and are defined as the straightest paths on these manifolds, traversed at constant speed. Additionally, the paths traced out by geodesics are typically the shortest paths connecting points on the manifold as measured by distance along the surface.[1]

By the least action principle, the straightest path minimizes the line integral of kinetic energy over the path [14]. For instance, given a unit point mass object moving on the surface, the kinetic energy for this object can be written as

[1]More completely, geodesics are local *extrema* of the length of paths connecting two points. In some cases, e.g., the path that goes the "wrong way" around the great circle on the globe, a geodesic can be locally the longest path connecting two points.

$$\mathcal{T} = \frac{1}{2}\left\|\frac{\partial\gamma}{\partial t}\right\|^2 \tag{2.3}$$

where $\frac{\partial\gamma}{\partial t}$ is the velocity of the particle along the path. Minimizing the integral of this kinetic energy over the duration of the trajectory results in movement with a constant speed (because the cost penalty for moving faster than average is greater than the benefit for moving slower than average), which means no tangential forces are applied to the system. If the particle moves on other paths other than the straight path, the path will be longer than the straightest path (shortest path) which requires higher speed to complete the path in a given time. This minimum kinetic energy path is the geodesic path.

To find the geodesic path, we define the energy of the $\gamma(t)$ curve [15], ε, as the time-integral of the system's kinetic energy,

$$\varepsilon = \int_0^t \left\|\frac{\partial\gamma}{\partial t}\right\|^2 dt = \int_0^t \dot{\alpha}^T\mathcal{M}\dot{\alpha}^2 dt, \tag{2.4}$$

where $\mathcal{M}$ is the metric tensor representing the manifold's *Riemannian metric*, and $\dot{\alpha}$ is the velocity in local coordinate, then minimize this energy over candidate paths γ. This minimization is equivalent to minimizing the pathlength,

$$s = \int_0^t \left\|\frac{\partial\gamma}{\partial t}\right\| dt = \int_0^t \sqrt{\dot{\alpha}^T\mathcal{M}\dot{\alpha}}dt = \int_\gamma \sqrt{d\alpha^T\mathcal{M}d\alpha} \tag{2.5}$$

and selecting a constant-speed traversal of the path, but the energy equation is generally preferable as an optimization criterion, because its quadratic nature makes it more robust in variational formulations [15].

The curve resulting from minimizing (2.4) satisfies [15] the equation

$$\frac{d^2\alpha_l}{dt^2} - \sum_{i,j} \Gamma_l^{ij} \frac{d\alpha_i}{dt}\frac{d\alpha_j}{dt} = 0, \tag{2.6}$$

where the Γ_l^{ij} terms are called Christoffel symbols and are given by the formula

$$\Gamma_l^{ij} = \frac{1}{2}\sum_k (\mathcal{M}^{-1})_{lk} \left\{ \frac{\partial \mathcal{M}_{jk}}{\partial \alpha_i} + \frac{\partial \mathcal{M}_{ik}}{\partial \alpha_j} - \frac{\partial \mathcal{M}_{ij}}{\partial \alpha_k} \right\}. \tag{2.7}$$

Christoffel symbols are the derivatives of the Riemannian metric, capturing how the metric changes with respect to the parameterized coordinates. The first term in equation (2.9) corresponds to the curvature of the trajectory in parameter space and the second term corresponds to the curvature of the manifold. A path is a geodesic when the parameter curvature matches the manifold curvature, such that the difference between them is zero. In the case that the object is a point-mass the second term in equation (2.9) is zero, indicates that the manifold is a flat surface.

2.2 Inertial Objective Function for a Point Mass Object

For a point mass system, the cost of the system to move depends on the acceleration of the system over the path. The acceleration composed of two different parts namely as tangential acceleration and normal acceleration. The tangential acceleration corresponds to speed change and normal acceleration corresponds to direction change over the path. Therefore, the cost can be formulated as a function of curvature and acceleration to be related to the geodesic concept:

$$IC_F = \int ((\kappa v^2)^2 + a_t^2)dt. \tag{2.8}$$

where κ is the curvature of the path, v is the speed, and a_t is the tangential acceleration over the trajectory. Since the object is point mass and surface is flat, the equation (2.9) can be simplified to

$$\frac{d^2\alpha_l}{dt^2} = 0. \tag{2.9}$$

This equation states that the manifold is flat and the geodesics are straight lines.

A simple example for such a system is racetrack which consists of two curved parts and two straight parts as illustrated in Fig. 2.1 (a). When a point mass object is moving on a racetrack, the total cost is the cost associated for staying in semicircle parts as well as the cost for changing the speed which can occur in transition points between the semi-circle and straight parts. Fig. 2.1 (b) shows the instantaneous cost is pathlength which results in constant speed with zero acceleration. According to the definition of inertial cost, the optimal solution for moving over racetrack occurs when the object is moving faster in straight parts and slower in parts with curvature (Fig. 2.1 (c)) which results in the reduction of overall cost. As it is shown in Fig. 2.1 (c) the optimal solution has spiky cost at transition points. That is because it switches abruptly between two states. Mathematically, there might be no problems, but in reality it causes oscillating

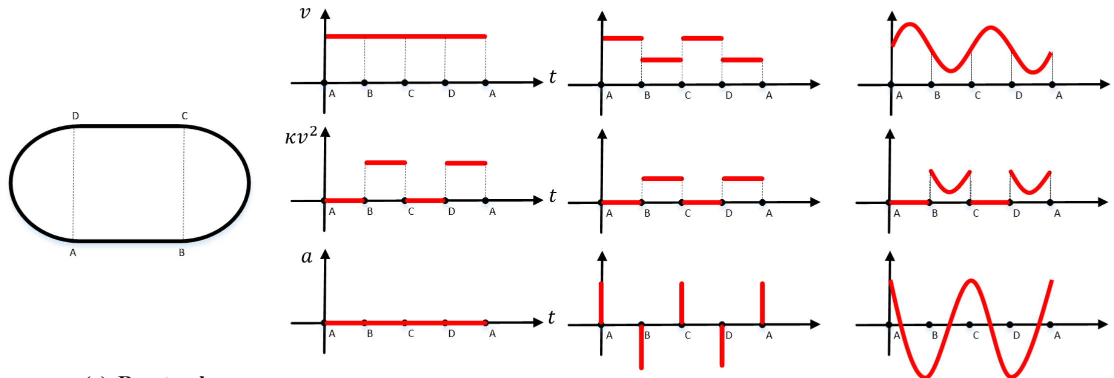

(a) Racetrack **(b) Cost as pathlength** **(c) Cost as acceleration and curvature (Dirac Delta)** **(d) Cost as squared acceleration and curvature**

Figure 2.1: (a) shows a racetrack. (b) the cost is considered as path-length which results in constant speed and zero acceleration. (c) the cost is considered as a combination of normal and tangential acceleration. (d) is the combination of squared normal and tangential acceleration.

error around desired set point value. Furthermore, this abrupt changes in speed, draw high electrical current which results in overheating the motor that leads to metal fatigue or other wear and tear effects.

To fix this problem we consider the cost as squared cost in which it generates acceleration over a distributed amount of time rather than only a point which results in removing the spikes in the optimal solution (Fig. 2.1 (d)).

2.3 Inertial Objective Function for a Multi-body System

When the object is not a point mass, the manifold is not flat but rather it has a curvature. To take the curvature of the manifold into the account, the Riemannian metric is used to capture the curvature.

For such systems, the Coriolis and centripetal forces exist and their effects are captured by the curvature of the space. Hence, the straight line between two points doesn't look straight since it is defined over the surface of a manifold. For instance, as illustrated in Fig. 4.2 (a) and (b) the straightest path on the globe is not the straight line in the latitude-longitude map due to the curvature of the globe. To deal with curve surface, it is required to understand the *Riemannian metric*.

A distance metric on a configuration space is a function that captures the distance between a pair of configurations as a single-valued real number [16]. On a Riemannian manifold, the curve connecting two points locally has the smallest length. The local distance ds is referred to as the line element or unit infinitesimal length element for the manifold, and its square is the *first fundamental form* of the space. This form can be represented quadratically as

$$ds^2 = d\alpha_1^2 + d\alpha_2^2 = \begin{bmatrix} d\alpha_1 & d\alpha_2 \end{bmatrix} \overbrace{\begin{bmatrix} 1 & 0 \\ 0 & 1 \end{bmatrix}}^{\mathcal{M}} \begin{bmatrix} d\alpha_1 \\ d\alpha_2 \end{bmatrix}, \tag{2.10}$$

where $\mathcal{M}$ is the metric tensor representing the manifolds Riemannian metric and $d\alpha_1$ and $d\alpha_2$ are elements in parameterized space. The identity metric indicates that this is a Euclidean distance and only considers distances on a flat manifold. However, to consider the motion on a curved manifold, another metric is required. In other words, a metric is a way to put weights in the path-length. For instance, the fundamental form of distances and metric tensor on a unit sphere parameterized by longitude α_1 and latitude α_2 are:

$$ds^2 = \begin{bmatrix} d\alpha_1 & d\alpha_2 \end{bmatrix} \overbrace{\begin{bmatrix} cos^2(\alpha_2) & 0 \\ 0 & 1 \end{bmatrix}}^{\mathcal{M}} \begin{bmatrix} d\alpha_1 \\ d\alpha_2 \end{bmatrix}, \tag{2.11}$$

where this metric captures the tapering of the sphere at the poles. This explains why the straightest path in the globe doesn't look straight in the chart and vice versa in Fig. 4.2 (a) and (b) which is because of the metric. To represent the metric in configuration space the ellipses are utilized [17]. The ellipses demonstrate how the manifold is stretched in parameterized space. This metric was appeared in equation (2.9).

Since the surface for multi-body systems has curvature, the two terms a_t and a_n in equation (2.8) are defined on the manifold. To find the normal and tangential accelerations on the manifold we start by finding the relationship between joint velocities and the current tangential velocity of the point-mass on the manifold. This relationship is given by

$$\begin{bmatrix} v_t \\ v_n \end{bmatrix} = J \begin{bmatrix} \dot{\alpha_1} \\ \dot{\alpha_2} \end{bmatrix}, \tag{2.12}$$

where $\dot{\alpha_1}$ and $\dot{\alpha_2}$ are joint velocities, v_t and v_n are tangential and normal velocities on the manifold (the tangential velocity is defined as the rate of change of metric weighted path-length. The normal velocity is a basis vector in tangent space of the manifold which is orthonormal to the tangential velocity.) and J is the Jacobian that maps joint velocities to velocities on the manifold.[2] To find the Jacobian, we take the following steps:

Because the motion of the system for a given $\dot{\alpha}$ is by definition tangent to the geodesic the system is instantaneously following, the Jacobian into tangential-normal coordinates must map the $\dot{\alpha}$ motion to a purely-tangential motion with matched energy, satisfying

$$\begin{bmatrix} 2\sqrt{\mathcal{T}} \\ 0 \end{bmatrix}_{\parallel} = J \begin{bmatrix} \dot{\alpha}_1 \\ \dot{\alpha}_2 \end{bmatrix}_{\parallel}, \tag{2.13}$$

where $\mathcal{T}$ is the kinetic energy of the particle, $\dot{\alpha}_1$ and $\dot{\alpha}_2$ are joint velocities at the current time.

To find the complete Jacobian, we use a Gram-Schmidt process to identify a velocity $\dot{\alpha}_{\perp}$ that is perpendicular to $\dot{\alpha}_{\parallel}$ *with respect to the mass matrix*, such that its output is purely normal in the tangential-normal coordinates,

$$\begin{bmatrix} 0 \\ 1 \end{bmatrix}_{\perp} = J \begin{bmatrix} \dot{\alpha}_1 \\ \dot{\alpha}_2 \end{bmatrix}_{\perp} \tag{2.14}$$

Combining (2.13) and (2.14) results in a relationship

$$\begin{bmatrix} 2\sqrt{\mathcal{T}} & 0 \\ 0 & 1 \end{bmatrix} = J \begin{bmatrix} \dot{\alpha}_{1\parallel} & \dot{\alpha}_{1\perp} \\ \dot{\alpha}_{2\parallel} & \dot{\alpha}_{2\perp} \end{bmatrix} \tag{2.15}$$

[2]It should be noted that, the $J^T J$ forms the metric ($\mathcal{M}$) and many Js exist that satisfy this.

from which the Jacobian into tangential-normal coordinates can be calculated as

$$J = \begin{bmatrix} 2\sqrt{\mathcal{T}} & 0 \\ 0 & 1 \end{bmatrix} \begin{bmatrix} \dot{\alpha}_{1\parallel} & \dot{\alpha}_{1\perp} \\ \dot{\alpha}_{2\parallel} & \dot{\alpha}_{2\perp} \end{bmatrix}^{-1} . \tag{2.16}$$

Multiplying J from (5.16) to the geodesic equation (2.9), we can write the geodesic equation in the form of tangential and normal acceleration on the manifold.

$$\begin{bmatrix} a_t \\ a_n \end{bmatrix} = J \left[\begin{bmatrix} \ddot{\alpha}_1 \\ \ddot{\alpha}_2 \end{bmatrix} - \begin{bmatrix} \sum_{i,j} \Gamma_1^{ij} \frac{d\alpha_i}{dt} \frac{d\alpha_j}{dt} \\ \sum_{i,j} \Gamma_2^{ij} \frac{d\alpha_i}{dt} \frac{d\alpha_j}{dt} \end{bmatrix} \right] \tag{2.17}$$

Now we can form the inertial cost function as

$$IC_F = \int \begin{bmatrix} a_t & \kappa_g v^2 \end{bmatrix} \begin{bmatrix} a_t \\ \kappa_g v^2 \end{bmatrix} dt \tag{2.18}$$

where the integrand is a local expression of the geodesic acceleration in (2.9) with κ_g the geodesic curvature of the path at each time, v the speed at those times, and a_t the tangential acceleration at those times. Equation (2.18) states how far the path is from the natural dynamic path, including both the curvature and tangential acceleration. If an object moves along the geodesic path with constant speed, it has zero normal and tangential acceleration and as a result, experiences zero forces.

This equation has a similar analogy to the strain energy of an elastic beam. It can be thought as an elastic rod that is bent between two points. It will straighten to reduce the curvature and contract axially when it is curved in which is not similar to a normal rod. The first term a^2 corresponds to the beam's tension

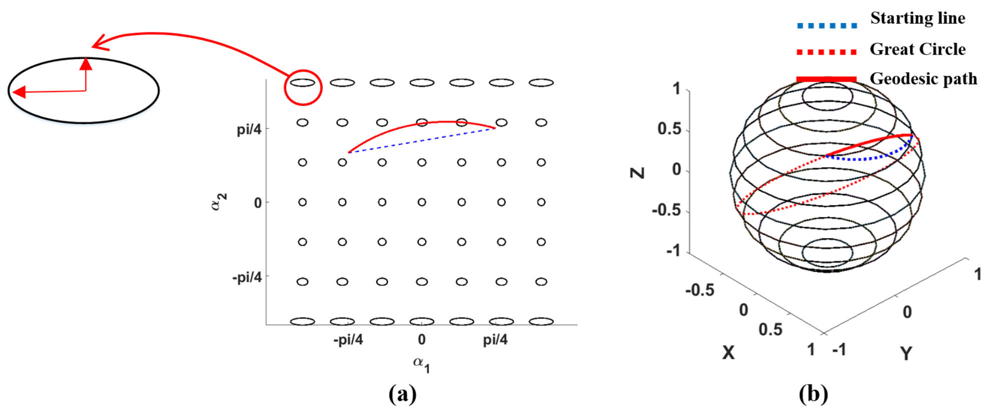

Figure 2.2: (a) shows the geodesic path in parameterized space (red curve). The ellipse indicates that the sphere is stretched in both hemisphere when it is wrapped up in plane coordinate (it shows moving in major axis direction is cheaper than minor axis one). (b) shows the geodesic line in embedded space. The red dashed line indicates the great circle of the sphere. α_1 and α_2 are parameterized coordinates in longitude and lateral directions respectively.

energy and the second term in the equation $(\kappa_g v^2)^2$ corresponds to the beam's bending energy.

To illustrate the relationship of geodesics path and Riemannian metric in parameterized space we consider a sphere. Two arbitrary points on the surface of the sphere and their corresponding points on the parametrized space coordinate frame (α_1 is longitude and α_2 is latitude) are considered. We start with the straight line between two points indicated with the dashed blue line to find the geodesic path. As expected the line move toward the north pole where the ellipses are bigger in one side as illustrated in Fig. 2.2 (a). The reason is the north and south hemisphere of the globe are stretched in the chart so moving in those regions are easier. Also, Fig. 2.2 (b) shows how the initial and final paths are on the sphere.

Chapter 3: Geometric Motion planning for fixed based systems

3.1 Introduction

The natural dynamics of a mechanical linkage (such as a robot arm) follow the geodesics of its inertia matrix. That is, if we take the linkage's configuration space as a manifold whose metric tensor is the generalized mass matrix with respect to its joints, then the system's free motion will be "straight lines at constant speed" over this manifold, with the effects of Coriolis and centripetal forces captured by the curvature of the space [18, 19, 20, 21]. For example, free motion of a point mass over a sphere follows Great Circles at constant speed.

A logical extension of this principle, employed in works such as [22, 23, 24, 11], is that least-effort start-stop trajectories[1] between points on the configuration space should lie along the images of those geodesics, overlaying them with an acceleration/deceleration profile. Because geodesics are both the straightest and shortest lines between points, such trajectories need no "steering" forces and require the least acceleration/deceleration to cover the distance in a given time. For example, the optimal start-stop paths of a thruster-driven system on a globe as shown in Fig. 4.2(b), also trace the Great Arcs of the globe. Therefore, the presence of acceleration/deceleration in the system only affects the speed, and not the path followed.

[1] Minimizing the time integral of squared actuator forces.

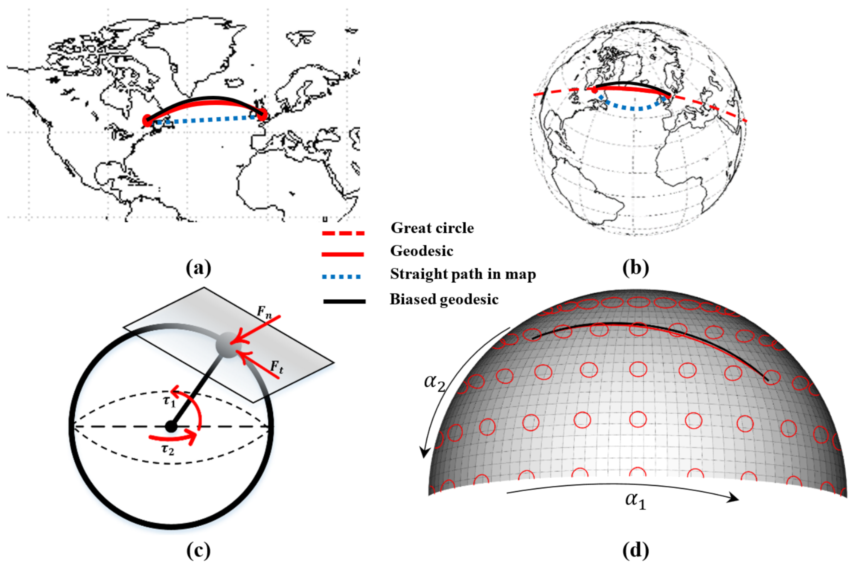

Figure 3.1: The shortest path on the globe (the geodesic) is not the straight line on a latitude-longitude map (a), because the globe is curved (b). The geodesic represents an optimal control path for moving a point-mass around the sphere when input forces are applied tangent to the sphere (c, top), but not when they are torques applied to a yaw-pitch mechanism at the center of the sphere (c, bottom). The force-to-torque relationship which biases the optimal control path away from the geodesic can be captured by a set of ellipses on the spherical surface (d), in which accelerations in the major direction require less torque. These ellipses are found by decomposing the system's metric tensor M into $J^T J$, where J is a Jacobian from the yaw-pitch coordinates to the sphere, and then everting the metric into the form JJ^T.

In our work on robotic systems, however, we observed that torque-optimal start-stop paths do *not* always (or even in general) trace out geodesics of the mass matrix. As an example, consider a point mass attached to a lightweight linkage (one leg taken from a Minitaur robot as illustrated in Fig. 3.2(a) [25]). Its natural dynamics (the mass geodesic path) are for the mass to move in a straight line at a constant speed in the direction of an initial velocity. Under the reasoning that

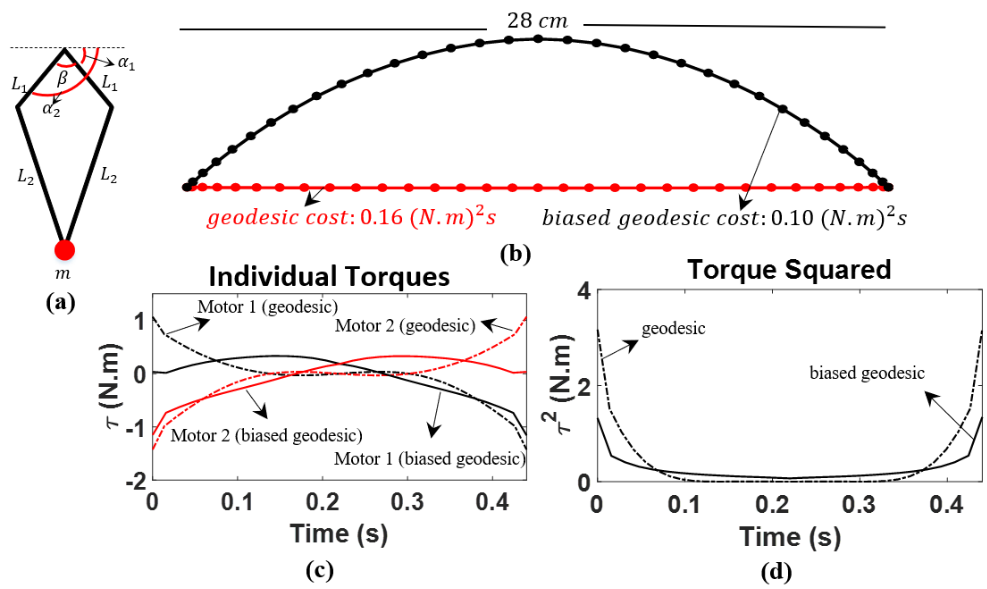

Figure 3.2: Biased and standard geodesics for a parallel actuator. The Minitaur leg (a) is a kite-shaped parallel actuator, to which we have added a large point mass at the toe. The geodesic motions for a point mass moving in task space are straight lines, and the biased geodesic trajectories are arches (b). The biased geodesic trajectory requires significantly less torque from Motor 1 at the beginning of the motion and from Motor 2 at the end of the trajectory (c), which reduces the overall torque squared requirement by 1.6 because the torque-squared reduction at the endpoints outweighs the additional torque required to curve the path near its midpoint.

torque-optimal start-stop trajectories between two points should likewise follow a straight line. Optimizing such trajectories, however, indicates that using the "arched" trajectory in Fig. 3.2(b) traverses the distance at 60% the cost of the best straight line acceleration profile over an equal time period.

What is missed in extending the geodesic concept from natural dynamics to forced trajectories is how the system's actuators project onto its configuration manifold. In many circumstances, this projection means that it is more efficient for the system to take on some "steering" cost, by moving away from the geodesic, in order to reach a region of configuration space where tangential acceleration requires less actuator effort, for an overall reduced trajectory cost.

For example, if we consider a spherical pendulum actuated via a motorized yaw-pitch gimble at the center instead of tangential forces at the surface of the sphere, the yaw motor has more leverage when the pitch is large, and the optimal start-stop path is drawn away from the great circles and toward the poles.

In the case of the Mintaur leg example, accelerating along the line requires the motors to apply torques in opposite directions. Pulling the mass inward allows one of the motors to "get out of the way" of the second motor (as seen in the comparative behavior of Motor 1 in the left plot of Fig. 3.2. Therefore, the overall torque squared cost decreases even though the total acceleration experienced by the mass increases. A symmetry in system dynamic means that it is likewise better in a torque-squared sense to decelerate while extending the leg even though this path is both curved and longer; this is illustrated in Fig. 3.2 by the torque in Motor 2 becoming small at the end of the motion.

In this chapter, we used a notion of *biased geodesic curvature* derived in previous chapter, which incorporates the projection of the actuators into the configuration manifold (Fig. 3.2). This biased curvature geometrically captures the costs of curving away from the current geodesic or accelerating along it in different parts of the space. Minimizing this biased geodesic curvature over all paths between two endpoints is equivalent to minimizing the torque-squared cost of motion between them. Considering this biased curvature as the "strain energy" of the curve allows us to create "biased geodesic spline" that connects a set of waypoints with the least torque cost. We demonstrate on the Minitaur leg that the biased geodesic motion plan outperforms geodesic plans even in the presence of friction and absence of feed-forward control.

3.2 Literature Review

Our analysis in this chapter draws on prior research efforts regarding geodesics as optimal paths for humanoid robots, human arm dynamics, and minimum energy splines in computer graphics.

3.2.1 Geodesics as Optimal Paths

In [18], the kinematic and dynamic properties of a mechanism are extracted from from geometrical properties. To illustrate the geodesic nature of natural dynamic paths, the surface whose metric is the inertia tensor was plotted together with the natural paths of their mechanism. In [19, 20, 21] the geometric characteristics of geodesics were used to find the optimal trajectory of robot manipulators, based on the premise that the geodesic is the optimal kinetic energy gait. In [26], the geodesic approach was used as an method for finding the energy efficient paths for a humanoid robot. They showed that the geodesic path planning is more energy optimized than spline interpolations in the parameter space. However, in the all aforementioned works, changes in speed over the path were not taken into the account and the kinetic energy was considered constant.

3.2.2 Human Arm Dynamics

An important problem in human arm dynamics is understanding the fundamental principles underlying the achievement of natural movements [27]. In order to consider the problem associated with central nervous system in the control of multi-joint movements, some researchers have focused on understanding the movement control in human arms and the variables that are controlled during the movement [28].

Biess et al. found that moving along the geodesic paths required less muscular effort than any other candidate non-geodesic path [10, 11]. Biess et al. in [10] conducted an empirical experiment on a robotic arm with different paths and postures and observed that the arm path and arm posture are independent of movement speed, suggesting that the geometric and temporal properties of movements are decoupled. They hypothesized that the spatial properties are obtained from the geodesic path in configuration space and the temporal characteristics are determined by minimization of squared tangential jerk along the path. Furthermore, they found that the geodesic path requires less effort compared to the paths calculated from minimum-total-jerk and minimum torque-change models.

3.2.3 Minimum Energy Spline

A spline is most generally a "shortest/smoothest" path that is obtained by minimizing bending/tension energy of a curve [29]. A Bezier curve is a type of spline which is defined by control points, with applications in fields such as computer graphics [30]. Motivated by the application of motion design, Ravani in [31] explored Bezier curves on Riemannian manifolds, and studied how the choice of coordinates affects the behavior of the curve in relation to the intrinsic solution. In [32] and [33] Hofer focused on the extrinsic formulation of energy-minimizing curves in embedded manifolds with application in computer graphics.

As an extension of spline problems, some research has been done on dynamic interpolation for control systems, in which certain dynamic variables of state trajectories are forced to pass through specific points by suitable choices of controls [34, 35, 36]. In this method, the spline paths are obtained by solving a dynamical control system, rather than being given a priori by polynomials.

Borum et al. in [37] studied the shape estimation of an elastic rod which is deformed by a robot. To find the smooth configuration based on minimum strain energy, they considered the equilibrium of elastic rod as a local solution to a geometric optimal control problem. They considered all the configurations of the rod as a smooth three-dimensional manifold so that they could work with a continuous description of the rod rather than a discretization.

3.3 Biased Geodesic Curvature

In the last chapter, we considered geodesics, identified as trajectories with constant speed. In this section, we investigate paths with *start-stop* motion. Consider a point-mass object moving over a manifold with start-stop end conditions. Since the geodesic is the straightest path and the shortest path on the manifold, no steering forces are required for the object to move and it requires the least acceleration/deceleration to cover the distance in a given time as compared to nearby paths [11].

Now assume that the point-mass object is connected to the center of the sphere with a massless rod which turns the system to the yaw-pitch gimble. Minimizing the torques on the rod's joint at the center of the sphere results in a different trajectory, which is away from the geodesic path as shown in Fig. 4.2(b) with the black line. This is due to the fact that, the yaw motor has more leverage when the pitch is large, therefore, the optimal start-stop path is drawn away from the great circles and toward the poles. To explore the reason the geodesic and minimum torque paths are different for the start-stop motion, we derive a minimum-torque-squared model as a function of geodesic curvature and acceleration over the dynamic manifold space to provide a meaningful relationship between the geodesic and minimum torque equations.

3.3.1 Torque-Squared Measure of Distance from Passive-Dynamic Paths

Minimizing the geodesic inertial cost defined in (2.18) corresponds to minimizing the tangential and normal forces on the sphere's surface indicated by F_t and F_n in Fig. 4.2(c). However, for systems analogous to the spherical pendulum, the torques on the joints are more important than forces on the end-effector as they are directly related to the effort needed to move the pendulum as shown in Fig. 4.2(c). Hence, it is required to take a step further and find a relationship between forces on the manifold and torques on joints space.

The equation (2.1) can be expressed geometrically as

$$\tau = M(\ddot{q} - c(\dot{q})) \tag{3.1}$$

where $M = J^T J$. Therefore, rewriting the equation again we have

$$\tau = J^T J(\ddot{q} - c(\dot{q})) \tag{3.2}$$

where the $J(\ddot{q} - c(\dot{q}))$ is equivalent to the equation (2.17) which leads the equation (3.2) to

$$\tau = J^T \begin{bmatrix} a_t \\ a_n \end{bmatrix} \tag{3.3}$$

These normal and tangential acceleration on the manifold are equivalent to the forces on the surface of the manifold as shown by F_t and F_n in Fig. 4.2. On the other hand, based on principle of virtual work, the relationship of torques and forces is [38]

$$\tau = J^T \begin{bmatrix} F_t \\ F_n \end{bmatrix} \tag{3.4}$$

which is equivalent to equation (3.3). Torque squared can thus be written as

$$\|\tau\|^2 = F_{tn}^T J J^T F_{tn}, \tag{3.5}$$

here F_{tn} is the column-vector of forces on the manifold in the tangential-normal coordinates. and finally from equation (2.18) and (3.5) we have a torque squared cost of

$$IC_\tau = \int \|\tau\|^2 dt = \int \begin{bmatrix} a_t & \kappa_g v^2 \end{bmatrix} J J^T \begin{bmatrix} a_t \\ \kappa_g v^2 \end{bmatrix} dt \tag{3.6}$$

where the subscript τ indicates the inertial cost that minimizes the torques. The quadratic mappings encoded by JJ^T are represented as ellipses in Fig. 4.2 (d) and 3.4 (b), with the major axes of the ellipses illustrating directions that require less torque for acceleration over the manifold.[2]

[2] To the best of our knowledge, the JJ^T structure has not been explored in the geometric mechanics literature, though its relationship to the metric tensor does bear some similarity to the relationship between Cauchy-Green and Finger deformation tensors considered in elastica theory. We suggest the name "everted metric" to describe this structure, corresponding to JJ^T being an "inside out" reorganization of the J^TJ structure that forms the standard metric on the space. Note that everted metrics are not equal to the inverse of the metric; they are also not

3.3.2 Trajectory generation

To find the optimal trajectories for both geodesic and biased geodesic, we utilize the basic variational principle that functions reach their extrema when their derivatives go to zero. Therefore, taking the gradient of equations (2.18) and applying Leibniz rules for gradient under the integral sign yields

$$\begin{aligned} \nabla_p IC_F &= \nabla_p \int ((\kappa_g v^2)^2 + a_t^2) dt \\ &= \int \nabla_p \kappa_g \; \kappa_g v^4 + \nabla_p v \; v^3 \kappa_g^2 + \nabla_p a_t \; a_t \end{aligned} \tag{3.7}$$

in which the above equation measures how changes in curvature and tangential acceleration affect the geodesic curvature. Likewise taking the gradient of (3.6) under integral sign yields

unique to the metric, as their construction depends on the coordinate basis in which the torque costs are taken as orthonormal.

$$
\begin{aligned}
\nabla_p IC_\tau &= \nabla_p \int ||\tau||^2 dt \\
&= \nabla_p \int \begin{bmatrix} a_t & \kappa_g v^2 \end{bmatrix} JJ^T \begin{bmatrix} a_t \\ \kappa_g v^2 \end{bmatrix} dt \\
&= \int 2 \begin{bmatrix} \nabla_p a_t & \nabla_p(\kappa_g v^2) \end{bmatrix} JJ^T \begin{bmatrix} a_t \\ \kappa_g v^2 \end{bmatrix} dt \\
&\quad + \int 2 \begin{bmatrix} a_t & \kappa_g v^2 \end{bmatrix} \nabla_p JJ^T \begin{bmatrix} a_t \\ \kappa_g v^2 \end{bmatrix} dt
\end{aligned} \tag{3.8}
$$

which measures how the changes in curvature and tangential acceleration as well as changes in JJ^T affect the biased geodesic curvature. We implement the (3.7) and (3.8) as the gradient for `fmincon` optimizer in `Matlab` utilizing the interior-point algorithm. More details in this section can be found in next chapter.

3.3.3 Biased Geodesic Spline

In the previous sections, the geodesic and biased geodesic were discussed as methods to connect two waypoints. In many cases more than two points need to be connected. Several methods can be used to connect the points: (1) minimizing the length of the path between points, (2) splines in parameter space, (3) splines based on geodesic curvature, and (4) a spline based on our biased geodesic curvature.

As an illustration of the methods above, we consider the cost of moving the

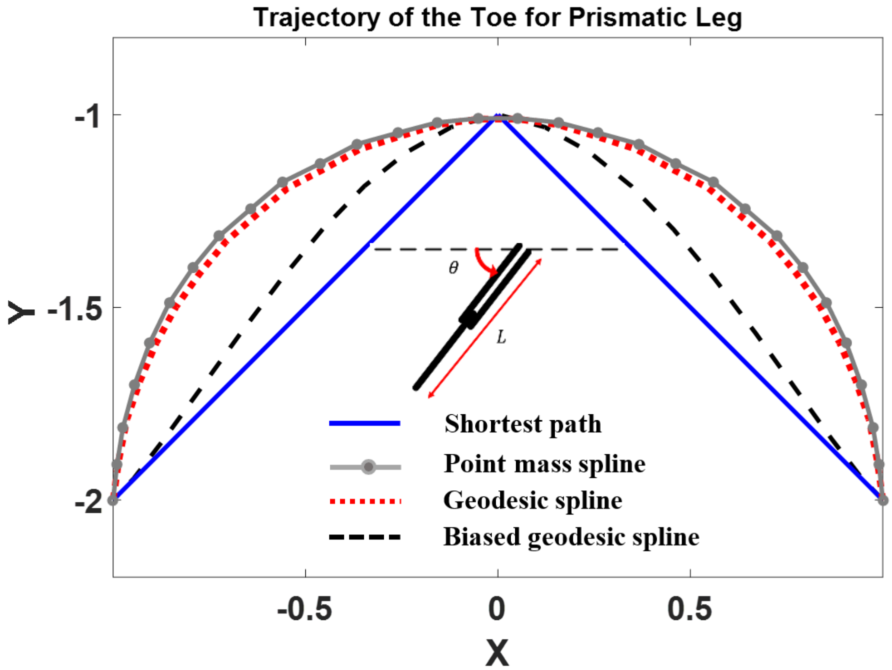

Figure 3.3: Various interpolations for a prismatic linkage moving its tip between three points. Minimizing pathlength results in a sequence of straightline segments, whereas splines that use curvature of the end-effector path or the path through the kinetic-energy manifold produce very round paths. The biased geodesic path concentrates its curvature near the peak, where the moment of inertia is smallest and the actuators have the most leverage.

end of a prismatic leg with two degrees of freedom (translational and rotational) by these methods among three points in the task space (xy coordinates of the end effector), where all the mass of the system is concentrated at the end effector.

The first method finds the geodesic between each pair of points. That means once more than one point exists, it finds the shortest path between each pair of points. This definition of the geodesic corresponds to the "shortest line" and is defined as

$$s = \int ds = \int \sqrt{dr^T \mathcal{M} dr}, \tag{3.9}$$

where dr is the infinitesimal changes in local coordinates [15]. As shown in Fig. 3.3 using this method, the path obtained is a triangle indicated with the solid blue line. If the acceleration is an important consideration along the path, this method is not suitable, as it has a high cost at the midpoint due to its high (infinite) curvature.

Splines in the extension-rotation space minimize the strain energy of the path to create smooth paths in these parameters while satisfying waypoints. The cost of these motions is defined from the first term in (2.9),

$$E_s = \int \left(\frac{d^2\alpha}{dt^2}\right)^2 dt, \tag{3.10}$$

which ignores the effects of Coriolis forces on the cost of motion. Using this method for the prismatic leg finds a semicircle running through the points (the grey line with circle markers).

Geodesic splines take into account the Coriolis forces, and thus minimize the in-manifold inertial cost function

$$IC_F = \int \begin{bmatrix} a_t & \kappa_g v^2 \end{bmatrix} \begin{bmatrix} a_t \\ \kappa_g v^2 \end{bmatrix} dt \tag{3.11}$$

while satisfying the constraints on points through which the path must path. Using this method on our example system results in a path which is away from the

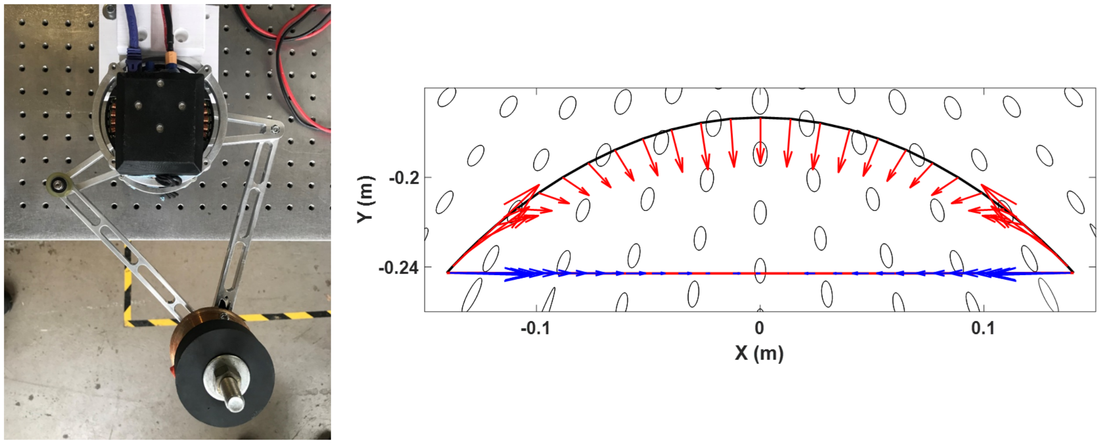

(a) **(b)**

Figure 3.4: Minitaur leg and input trajectories. (a) The physical Minitaur leg, mounted to move in a horizontal plane with a large point mass at the distal joint. The link lengths (as labeled in Fig. 3.2) are $L_1 = 0.1m$ and $L_2 = 0.2m$. The end effector mass is $m = 730g$. (b) The minimum torque geodesic accelerates and decelerates along the line connecting the start and end points. Because this line is closely aligned with the minor axes of the JJ^T ellipses, this trajectory costs more than the arched trajectory, whose accelerations are aligned with the major axes of the ellipses, even though the geodesic path is shorter and has no curvature. The arrows show the acceleration direction along the path.

semicircle path due to the existence of the Riemannian metric. This metric has the information regarding the physical characteristics of the system, and the path moves in the direction where according to the inertia, less effort is required, with the result that the trajectory is “pulled in” from the spline that was not aware of Coriolis forces.

The biased geodesic spline incorporates the leverage that the actuators have on acceleration through the manifold, with a cost function

$$IC_\tau = \int \|\tau\|^2 dt = \int \begin{bmatrix} a_t & \kappa_g v^2 \end{bmatrix} JJ^T \begin{bmatrix} a_t \\ \kappa_g v^2 \end{bmatrix} dt. \tag{3.12}$$

Using the biased geodesic spline method on the prismatic leg pushes the path away from the geodesic path to decrease the squared torque on the motors as shown in Fig. 3.3. Although the cost due to curvature increases (the curvature is more concentrated, the overall cost decreases.

3.4 Hardware Demonstration

To demonstrate the principle that the optimal start-stop paths do not follow geodesics, we conducted an experiment using a leg from the Minitaur robot [25]. In this experiment, we measured the torque required for a 2-DoF parallel manipulator to follow two given trajectories. Both trajectories are start-stop trajectories. One trajectory follows a geodesic in the manipulator's configuration space with minimum squared tangential acceleration along the path, and the second trajectory was generated through the biased geodesic optimizer to be torque-squared-optimal. Both trajectories are followed using PD control around the motor angle.

3.4.1 Testing apparatus

We used the direct-drive, kite-shaped parallel linkage (a Minitaur leg). This leg is shown in Fig. 3.4 fixed rigidly to a heavy base and operated in a horizontal plane normal to gravity. The two proximal links are each actuated relative to ground by a high-torque motor with no gear reduction.

The linkage itself has very little inertia. We attached a point mass to the end of the manipulator. The point mass is heavy enough to dominate the system dynamics. By comparison, the links of the manipulator are negligible, so the system's inertia is approximated as a simple point mass in the plane.

3.4.2 Trajectory commands

The manipulator was commanded to follow start-stop trajectories between two points in the plane. Using a dynamic model of the mechanism, we derived the nominal motor trajectories for two trajectories between the same endpoints. One trajectory follows the mechanism's geodesic path with least squared acceleration along the geodesic, which is a straight line because the system dynamics are dominated by the point mass. The second trajectory follows an arched least-torque path found through torque squared optimization, illustrated in Fig. 3.2. Each trajectory traverses between following given points:

$$x_i = +0.14\ m \qquad x_f = -0.14\ m$$
$$y_i = -0.24\ m \qquad y_f = -0.24\ m$$

We used our optimizer to find both the geodesic and biased geodesic path. Then we calculated the required torques for the system to move between the points. Fig. 3.5 (b) shows that the geodesic path has a higher torque value at the starting point than the biased geodesic which is due to the fact that the projection of acceleration of the path into the actuators space has higher acceleration/deceleration at endpoints. We also plotted the torque-squared in Fig. 3.5 (e) that once again depicts that the biased geodesic path requires less torque to traverse between given points.

3.4.3 Experimental Results

To run the experiment, both the geodesic and biased geodesic trajectories were discretized into 384 points over a $T = 0.42$ second period between two end points. At each timestep, the manipulator received motor angle commands then applied motor torque based on a PD controller around each motor's error. The PD control was tuned with $K_P = 0.9$ and $K_D = 0.025$ gains.

Fig. 3.5 shows the motor torques for both geodesic and biased geodesic in the start-stop trajectory. The motion has been repeated for multiple times, the torque profile for each motor was captured through each cycle, and the results from the trials were overlaid on each other. In Fig. 3.5 (a) and (c), torques obtained from both the simulation and experimental results are plotted. The results demonstrate that the torques obtained from experimental results are in agreement with simulation. The Fig. 3.5 (d) and (f) illustrate that the torque squared for the biased geodesic path is smaller than the geodesic path, which corroborates that deviating from geodesic is beneficial for the system. This observation shows that, although the geodesic paths are known as natural trajectories, start-stop trajectories do not follow the geodesics. Instead, moving away from the geodesic the acceleration in the joint space leads to a total decrease in squared torque.

3.5 Discussion

In this chapter, we have demonstrated that start-stop paths following geodesics are not in general torque-squared-optimal for robotic manipulators. We introduced a novel "biased geodesic curvature" takes into account the leverage that the actuators have on the system motion via their projection on the system's dynamic manifold, such that the minimum-torque-squared trajectories for the manipulator are those that minimize the biased geodesic curvature.

To demonstrate the principle that start-stop motion along geodesic paths is not torque-optimal, we conducted an experiment using a parallel actuator (a Minitaur leg). For the sake of simplification, we added a point-mass to the end-effector of a lightweight parallel mechanism, making the geodesics simple straight-line motions. For start-stop motions, moving in an arc that used the biased geodesic curvature to take into account leverage of the motors on the system dynamics required less torque-squared than did moving along the geodesic.

Beyond clarifying the relationship between geodesics and optimal control policies, we see the key impact of this work as providing an intuitive understanding of a link between mathematical models of a robot's dynamics and its physical motion, building on past efforts such as [18]. These intuitive understandings facilitate discussions about the structure of the solution equations and dissemination of this knowledge into fields such as engineering and biology. In our own work, we are incorporating the biased geodesic formulation into our locomotion dynamics framework [16], extending [1, 39] to handle systems with inertially-dominated dynamics such as swimmers at high reynolds numbers.

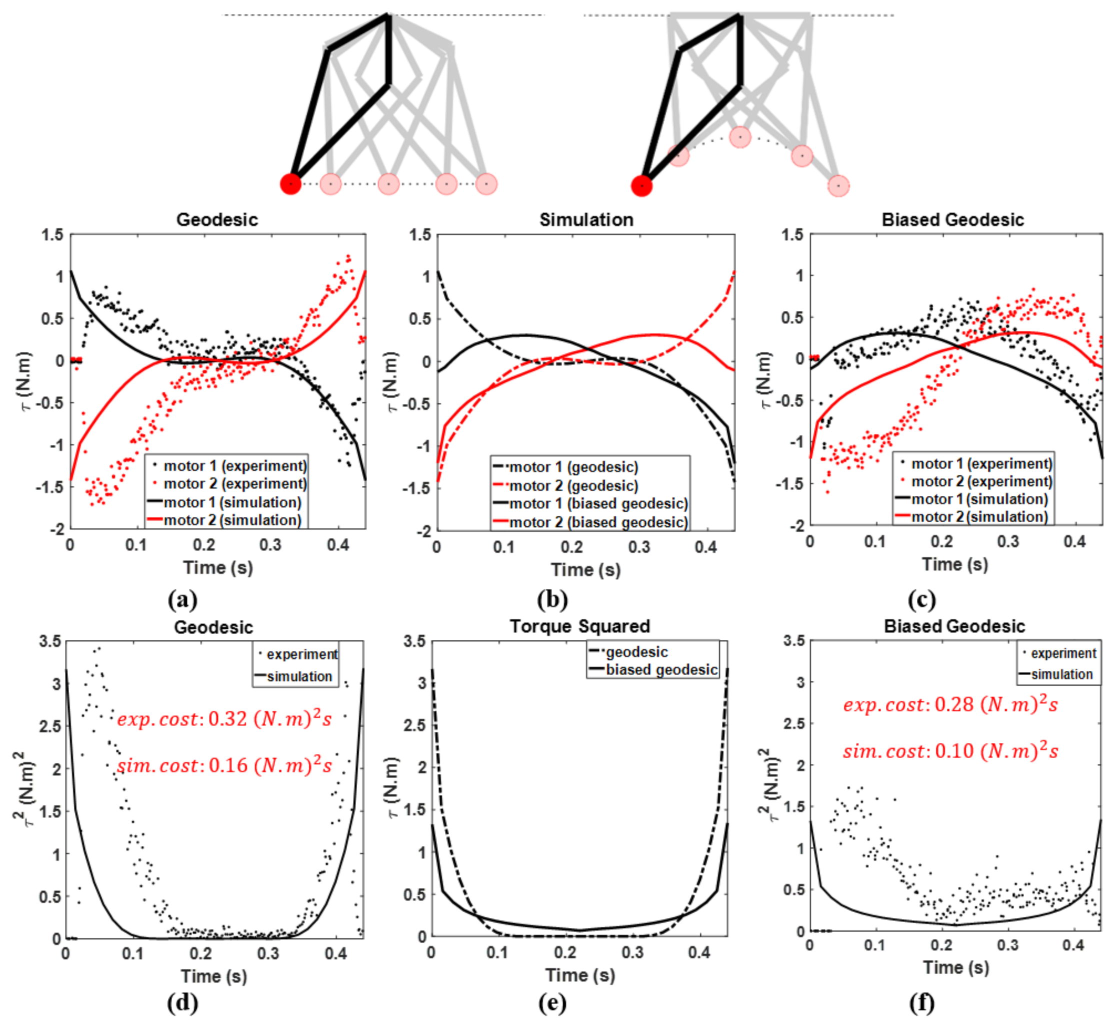

Figure 3.5: Torque profiles for the geodesic and biased geodesic trajectories in simulation and experiment. (a) and (c) show the torques for each motor for both the simulation and experimental results. In (b) the torque inputs for both geodesic and biased geodesic are plotted. (d) and (f) illustrate the torque squared in the start-stop trajectory for geodesic and biased geodesic respectively. In (e) torque squared for both geodesic and biased geodesic curvature are plotted.

Chapter 4: Geometric Motion planning for Moving based systems

4.1 Introduction

Robot locomotion is a method that a robot uses to move from one point to another point and consists of interaction forces, constraints, mechanism and actuator that generate forces. Hence, it is a challenge to find the relationship of body deformations coupled with an environment.

A general method for gait generation for multiple-link crawling robotic systems is to change a variable in the input of the optimizer, compute the system's equations, evaluate the outputs, and repeat this process over and over. [8, 9]. This process is a tedious work and computationally expensive and won't provide an complete view of the system's movement.

To address this issue, the geometric community has been developed a tool that uses Lie bracket of system dynamics to identify shape changes that produce net displacements in world coordinate. Lie Bracket can be plotted as curvature function which provides a good visualization of the systems motion for any gait whose topographies identify good placements for gait trajectories [7].

Overall, prior works including our own work have only considered trajectory generation for non-inertial systems and that is only for systems called moving base system in viscose environments [13].

Our group in soap bubble paper collected these observation into a formula for the efficiency of the system in a drag-dominated environment in which the most efficient gait obeys from dynamic analogous to a soap bubble [1]. They encoded the geometric insight into a variational gait optimizer. The optimizer is a gradient ascent/descent algorithm that pushes the cycle to enclose a large sign-definite region of the Lie bracket to maximize the net displacement it generates. A cost function is based on a Riemannian distance metric that limits the growth of the gait cycle. To balance the perimeter of the gait, the optimizer evenly-spaces the waypoints in the trajectory that causes stability of solution and provides an efficiency-optimal parameterization gait. However, the insights afforded by this optimizer is restricted to the drag-dominated system including viscous swimmers [13, 40, 41, 42].

Unlike existing methods in motion planning, the focus of our proposed method is to provide an intuition of the relationship between the geometry and inertia of the system and the optimum way of moving. Therefore, the user can design a gait and observe the effectiveness of different gait patterns without integrating the complete dynamics.

This class of interaction is inertially dominated system, such as system floating in space, and swimmer interacting in environment with large Reynolds numbers where the inertial effect is important. Cost as path-length seems reasonable to find the optimum path for the drag-dominated system where the effort required to change shape is the path-length. However, closer consideration raises question regard to the systems with inertia. What is the cost for such a system? How to

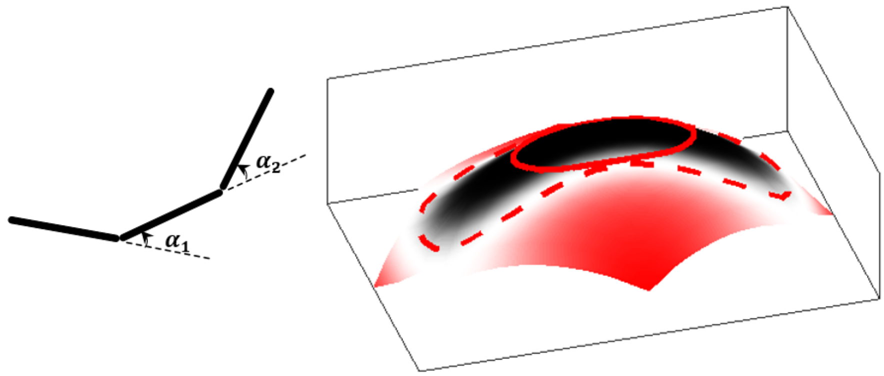

Figure 4.1: The maximum displacement and optimal gaits for the three-link swimmer at high Reynolds over the manifold. The solid line is the optimal gait and the dashed line is the maximum displacement

formulate the cost?

Taking the cost of motion as squared-torque on the joints, the inertial contribution to this cost is proportional to the squared-acceleration of the system -changes in speed and direction of its trajectory- weighted by the system's inertia term. For an isolated inertial locomotion system, the trajectory can be reduced to the trajectory through its shape space, using the coupling between shape and position velocity to define an effective inertia with respect to the shape variables. The acceleration of the system used to calculate the cost is its acceleration relative to the "free motion" of the system. If the effective inertia changes as a function of the system shapes, then these free motion - the *geodesics* of the inertia matrix - are not constant speed, straight lines in the parameter space, in the same way the moving forward on a globe doesn't look straight line in latitude-longitude space, but instead traces out a great circle. The acceleration relative to these natural dynamics geodesics can be found by substituting out the Coriolis terms (Christoffel symbols) from the parameter acceleration. If the gait trajectory has curvature (the Coriolis-curvature acceleration is not everywhere parallel to the velocity) then optimal trajectories slow down in the curved parts (and speed up in straight parts) to minimizes the overall acceleration.

Fig. 4.1 illustrates the maximum displacement and optimal gaits for the high Reynolds three-link swimmer over the manifold which is formed based on configuration space. It shows the relation of the curvature of the path, the curvature of the manifold and curvature of the constraints.

In this chapter, we take four steps.

- The first step is to develop insight of what inertia means for mechanical systems and how inertia affects on the optimal trajectory.
- The second step is to develop the concept of a minimum energy path using the geodesic curvature concept which provides a physically meaningful interpretation of the natural dynamic path with respect to the inertia.
- Third step is to use the concept of the geodesic path and inertia to generate a minimum torque path which provides an intuitive understanding of the minimum torque with respect to the acceleration and curvature of the path.
- In forth step, we develop a variational principle based on system geometry and inertia to find the efficient gait.

The proposed framework provides a good insight of the gait patterns. The gait patterns are required to translate and rotate the robot in different directions.

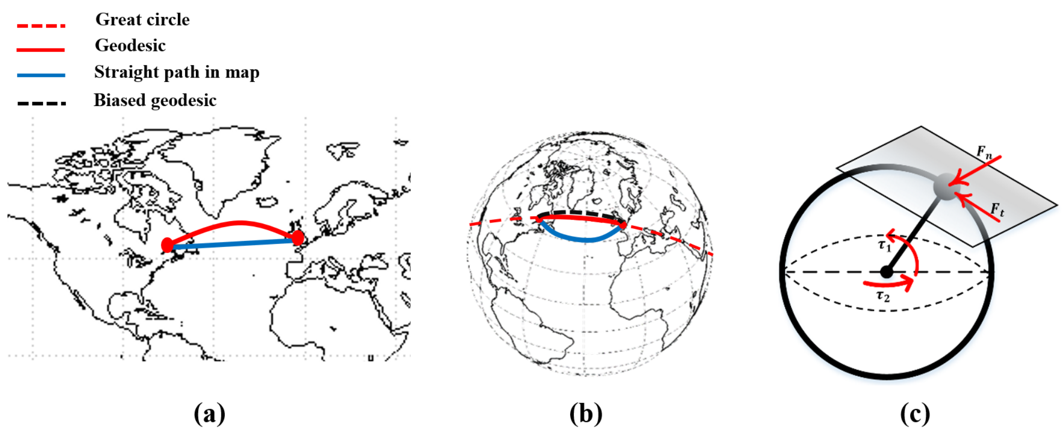

Figure 4.2: The shortest path in the globe is not the straight line since surface has a curvature. (a) shows the shortest path in chart of the globe (b) shows shortest path in globe. (c) this plot depicts that, the topological space of inverted pendulum is sphere and shows that the the cost as geodesic equation minimizes the forces on the surface of the sphere (forces on end effector) whereas, the cost as minimum torque minimizes the forces on the center of sphere (joint of pendulum).

This geometric visualization conveys a concise understanding of the relationship between 1) gait amplitude and 2) the size and efficiency of the displacement it induces. This understanding helps users to design a controllable gait for robots. We start by first discussing the meaning of straight line. We will show that the straightest path on the globe is not the straight path on the map and vice versa but rather it depends on the curvature of the manifold. The cost is defined as how much the path bend from the curvature of the manifold (Fig. 4.2 (a) and (b)). Furthermore, we will modify the minimum torque squared cost obtained in last chapter to be appropriate for moving based systems.

4.2 Literature Review

Our work builds on the body of locomotion literature that uses geometric mechanics. Geometric mechanics is a powerful mathematical framework for analyzing locomotion [43, 44, 45].

Walsh and Sastry [46, 47] studied the dynamics of a planar three-link robot floating in space. They derived a specific form of the Lagrangian to generate gaits for the planar three-link snake robot. They have proposed sinusoidal gaits and then computed the geometric phase shift produced by these gaits.

Kanso and Melli [48, 42] studied the locomotion of solid bodies submerged in an ideal fluid. They used this model to analyze the coupling between their shape changes and the fluid dynamics in their environment. They showed that the hydrodynamically decoupled model produces smaller net motion than the coupled model, indicating that it is important to consider former one.

Ostrowski and Burdick [49] and Ostrowski et al. [50], took advantage of the idea of translational symmetry from physics and projected the entire dynamics of the system onto the joint space. They introduced a relationship between the body velocity and shape variables using the reconstruction equation. This allowed the systems dynamics to be represented as an affine non-linear control system. Furthermore, they combined the reconstruction equation with Lie bracket theory to generate sinusoidal gaits. These translate and rotate a variety of snakelike systems. Using this approach, they intuitively developed and the analyzed gaits for principally kinematic and dynamic systems with non-holonomic constraints.

Shammas et al. [51, 52, 53] combined the idea of Stokes theorem with the reconstruction equation to define height functions on the shape space of their three-link robots. This allowed the design of gaits that resulted in specified rotations. This allowed them to depict all of the shape parameters of the suggested curves, which reduced the need for deeper intuition to manually or empirically setting these parameters. Hatton and Choset [7] addressed the limitation that for general macroscopic (non-infinitesimal) gaits, the height functions could only be used to determine the net rotations over the gaits. They introduced a choice of coordinates that reduced the error by making appropriate choices of system parameterization. Additionally, this converted much of the systems non-commutativity into non-conservativity, which is amenable to finite-scale integration.

In [13] we used the concept of geometric mechanics to simplify the problem of controlling a snake robot moving across a granular surface. We showed that geometric mechanics provide a deep understanding of the relationship between gait amplitude and the size and efficiency of the displacement it induces. We also identified a turn-in-place gait that has not previously appeared in the snake robot literature. In recent work, Ramasamy and Hatton applied Lie bracket methods to a gradient-based optimizer for drag-dominated environments [1]. To find the optimized gait, they built a gradient ascent/descent component that push the gait cycle to enclose a large sign-definite region of the Lie bracket to maximize the net displacement it generates. The cost component that was used was based on a Riemannian distance metric that limits the growth of the gait cycle and a component to evenly spaces the way points on the gait. These components together form a dynamical system analogous to a soap bubble, whose boundary (here, the gait curve) is pushed outward by internal pressure (here, the Lie bracket) and is constrained by surface tension (here, the metric-weighted path-length).

All of the related works, help the user obtain a geometric intuition of the system to design a gait. However, there has been no work done for finding the optimal solution for a system with inertia which is very important since most of the systems in real world have inertia. In our work, we are aiming to build upon prior work and introduce an optimizer to deal with inertia based systems as well as providing geometric intuition of the systems.

4.3 Geometric Locomotion Model and Local Connection

To model the locomotion system we divide the configuration space $q = (g, r) \in Q$ into a position space G and shape space M, such that the position $g \in G$ locates the system in the world, and the shape $r \in M$ gives the relative arrangements of its bodies. As an example, the position of the three-link swimmer as shown in Fig. 4.3 is the average location and orientation of the links, $g = (x, y, \theta) \in SE(2)$, and its shape is parameterized by two joint angles, $r = (\alpha_1, \alpha_2)$. This separation is a means that demonstrates that how the change in shape effects on the displacement of the body.

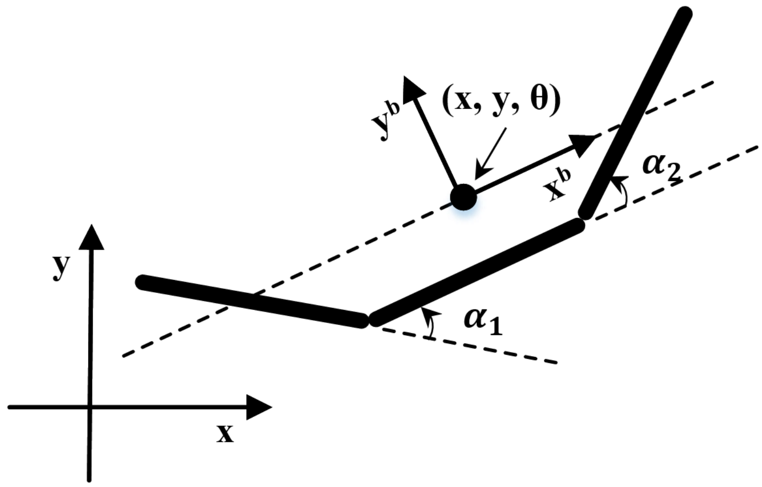

Figure 4.3: Three-link swimmer geometry.

4.3.1 Local Connection

In geometric mechanic, there exists a linear relationship between changes in shape velocity $\dot{r}$ and body velocity $\mathring{g}$,

$$\mathring{g} = -\mathbf{A}(r)\dot{r} \tag{4.1}$$

where $\mathbf{A}(r)$ is the local connection matrix and acts like a Jacobian that maps shape velocity to the body velocity [7]. This can be used as a tools to find an optimize gate for the snake robot. This equation is a reconstruction equation in which it can be integrated to reconstruct the position trajectory from given shape changes.

The local connection for inertial systems can be calculated from kinetic energy equation. For the system with conservative of momentum, Lagrangian is equal to its kinetic energy that is isolated from external forces (energy can only be added or removed from the system through generalized forces applied to the internal shape variables). The kinetic energy can be expressed as

$$T(\mathring{g}, r, \dot{r}) = \frac{1}{2} \begin{pmatrix} \mathring{g} & \dot{r} \end{pmatrix}^T \mathcal{M}(r) \begin{pmatrix} \mathring{g} \\ \dot{r} \end{pmatrix} \tag{4.2}$$

where $\mathcal{M}$ is the inertia matrix and of the form

$$\mathcal{M}(r) = \begin{pmatrix} I & -I\mathbf{A} \\ -I\mathbf{A}^T & m \end{pmatrix} \tag{4.3}$$

where I is the local form of the locked inertia tensor [1], m is a square matrix that depends only on the base variables and $\mathbf{A}$ is the local connection and can be easily extracted.

4.3.2 Constraint Curvature Functions

Geometric mechanics community (including our own) have utilized the structure of the systems Lie bracket (a measurement of non-commutivity of the system) to identify the oscillation that produces maximum displacement and also the structure of optimal solutions to the system equation of motion [7]. By an extension of Stokes theorem [55], the net displacement over a closed loop ϕ can be approximated by an area integral of the curvature $D(A)$ of the local connection (total Lie bracket [55]) over a region enclosed by the loop.

[1]Locked inertia is the instantaneous moment of inertia in which all the joints in the system are considered to be fixed [54].

$$
\begin{aligned}
g_\phi &= \oint_\phi g\mathbf{A}(r)\,dr \\
&\approx \iint_{\phi_a} \underbrace{d\mathbf{A} + [\mathbf{A}_1, \mathbf{A}_2]}_{D(\mathbf{A})\ \text{total Lie bracket}}\ dr
\end{aligned}
\tag{4.4}
$$

where $d\mathbf{A}$ is the curl of local connection which is taken row-wise and the local Lie bracket term evaluates (on SE(2)) as

$$
[\mathbf{A}_1, \mathbf{A}_2] = \begin{bmatrix} \mathbf{A}_1^y\mathbf{A}_2^\theta - \mathbf{A}_2^y\mathbf{A}_1^\theta \\ \mathbf{A}_2^x\mathbf{A}_1^\theta - \mathbf{A}_1^x\mathbf{A}_2^\theta \\ 0 \end{bmatrix}
\tag{4.5}
$$

We can plot the curvature terms as a constraint curvature function on shape space as shown in Fig. 4.4. Gaits that produce net displacement in (x, y, θ) direction are located in sign-definite area of the corresponding constraint curvature function. For instance x-direction gaits enclose the center of the shape space for high-Reynolds swimmer, whereas θ-direction for floating snake is produced by cycles in the corners of the shape space.

4.3.3 Efficiency of the Gait

For a mobile robots the efficiency of the optimal gaits is a way to evaluate design and performance of the system. An appropriate way to look at the efficiency of the locomotion is the *cost of transport*. It allows for fair comparisons between

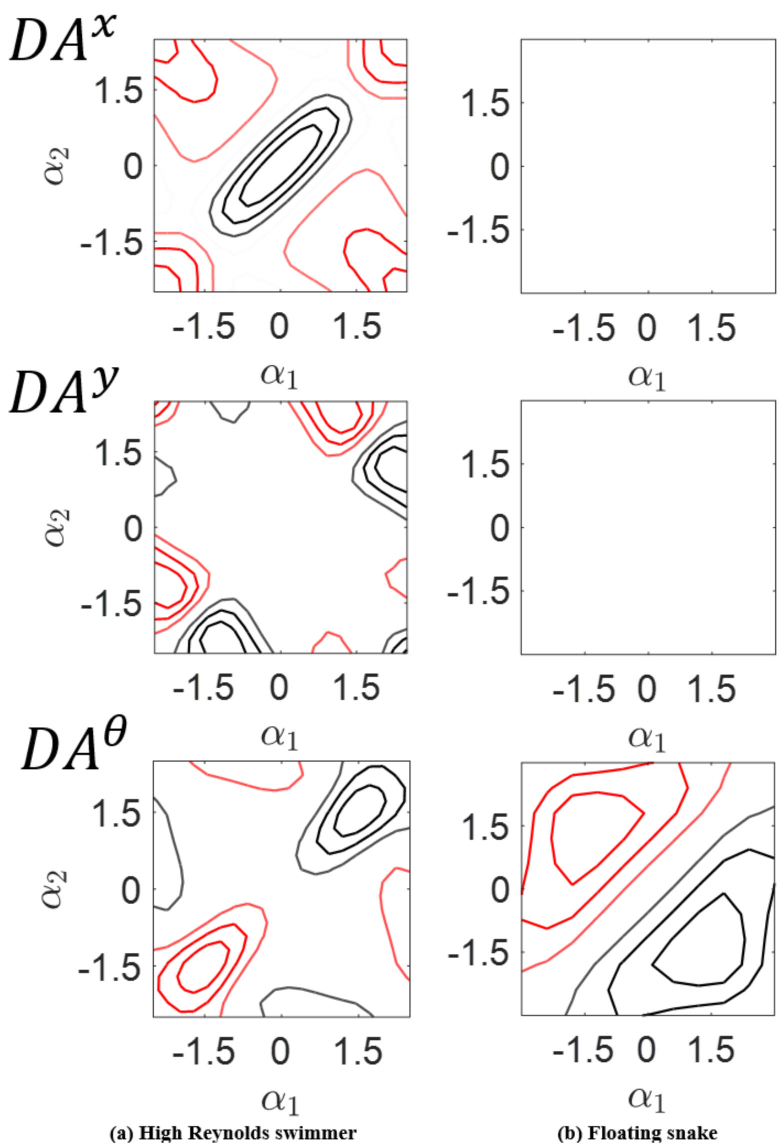

Figure 4.4: Curvature constraint function (plots of the Lie bracket DA) for the three link swimmer (a) at high Reynolds and (b) floating in space are shown. The conservation of momentum for floating snake results in zero displacement, therefore the CCF in x and y directions has zero curvature.

different gaits within and across systems with different morphologies. Our measure of efficiency, $\frac{g_\phi}{cost}$ is equivalent to the inverse of the cost of transport.

Previous works [1, 13] were focusing on the systems moving in viscous environment. For such systems, cost is defined as the dissipative power. The dissipative power through the join is the dot product of the velocities and torques ($p = \dot{\alpha}\tau$) where $\tau = f(\alpha)\dot{\alpha}$. Therefore, the power can be turned into Riemannian metric in which the path-length measures the effort required by a shape trajectory [17].

The maximum displacement gait over the cycle for such systems follows the zero-contour of the curvature constraint function. Therefore, the maximum-efficiency gait for drag-dominated systems is obtained by giving up low-yield regions at the ends of the cycle and crosses slightly outside the zero contour [1].

However, if the system has inertia and inertia is considerable, the Riemannian metric is induced by the inertia matrix of the system rather than power dissipation, and effort corresponds to measurement of torques on the joints. Therefore, the first step is to find the Riemannian metric for such systems. Metric weights the components of coordinate in the length calculation. To find the Riemmanian metric for purely mechanical systems and conserved systems the kinetic energy need to be calculated and the inertia matrix is the Riemmanian metric as calculated in (5.8). In order to make the metric function of shape velocity (base bundle), the energy equation can be rewritten as

$$T(g, r, \dot{r}) = \frac{1}{2}\dot{r} \begin{pmatrix} -A(r) & I \end{pmatrix}^T \begin{pmatrix} I & IA \\ IA^T & m \end{pmatrix} \begin{pmatrix} -A(r) \\ I \end{pmatrix} \dot{r} \tag{4.6}$$

Then, the metric can be written as below:

$$M = \begin{pmatrix} -A(r) & I \end{pmatrix}^T \begin{pmatrix} I & IA \\ IA^T & m \end{pmatrix} \begin{pmatrix} -A(r) \\ I \end{pmatrix} \tag{4.7}$$

Now the equation (4.7) depends only on base variables (α_1, α_2) and can be used for finding the optimal gait.

4.4 Inertial Cost of Motion

Unlike the drag-dominated system [1], in inertia-dominate based system, the cost as path-length doesn't directly matter and it cannot capture the effort required for the system dynamic to move in natural dynamic path. In inertia-dominate based system, the cost is based on the natural dynamics of a mechanical linkage (such as a robot arm) that follow the geodesics of its inertia matrix. That is, if we take the linkage's configuration space as a manifold whose metric tensor is the generalized mass matrix with respect to its joints, then the system's free motion will be "straight lines at constant speed" over this manifold, with the effects of Coriolis and centripetal forces captured by the curvature of the space [18, 19, 20, 21]. For example, free motion of a thruster-driven system over the sphere follows Great Circles at a constant speed, during which the only force acting on the system is the centripetal force due to the circular motion. However, considering the start-stop trajectories for multi-body systems the geodesic paths cannot capture the minimum torque required for the system to traverse over the path as it was demonstrated in §3.3.1. In this chapter, we will modify the cost as torque squared in order to use it for moving based systems.

4.5 Analyzing Gaits Behavior

Two important effects in gait optimization may occur: *scaling effect* and *squashing effect*. The squashing effect was described in §2.2 where the effect of curvature and acceleration on the cost was considered and it was shown how by accelerating/decelerating in different regions of the path that has different curvatures can reduce the overall cost. In this section, we consider the scaling effects and its relation with both drag cost and inertial cost.

4.5.1 Scaling Effect

In this section, the gait's scaling effect on the cost is considered. When a gait scales up/down, the total length of the gait increases/decreases which changes the curvature of the gait. This change may also affect on the speed, but the acceleration remains unchanged. Therefore, we are allowed to remove the tangential acceleration from inertial cost equation (3.6) and write it in simple form as

$$IC_F = \int (\kappa v^2)^2 dt \tag{4.8}$$

Now we set the instantaneous cost constant

$$(\kappa v^2)^2 = 1 \tag{4.9}$$

Therefore, the equation (4.8) takes the below form

$$IC_F = \int 1dt \tag{4.10}$$

dt is obtained from equation (4.9) as below:

$$\kappa(\frac{ds}{dt})^2 = 1 \Rightarrow dt = \sqrt{\kappa}ds \tag{4.11}$$

and then substituting (4.11) into the equation (4.10) results in:

$$IC_F = \int \sqrt{\kappa}ds \tag{4.12}$$

The above equation demonstrate how the cost is changing due to the gait's change. To illustrate the structure of the gait a comparison is made. As mentioned previously, the drag cost is defined as path-length and it is equivalent to the perimeter of the gait. Therefore, as the gait scales up/down the cost changes proportionally. For instance, if the gait is a circle with radius r, the path-length is equal to the perimeter of the circle which is $2\pi r$ therefore, $Drag\ Cost \propto r$. On the other hand, for inertial cost as it is shown in equation (4.13) is equivalent to $\sqrt{\kappa}s$ which means the cost scales cheaper than the drag cost. For example, since $\kappa \propto \frac{1}{r}$, and the $s \propto r$ therefore $Inertial\ Cost \propto \sqrt{r}$.

The equation (4.11) can be written in time format

$$IC_F = \int \sqrt{\kappa} ds \Rightarrow \int \sqrt{\kappa} v dt \Rightarrow \int (\kappa^2 v^4)^{\frac{1}{4}} dt \tag{4.13}$$

The term $\kappa^2 v^4$ equals to the squared of normal acceleration (a_n^2) and has the same unit as of squared tangential acceleration (a_t^2), therefore, we can write equation (3.6) in the right format that conforms with the change of gait's size.

$$(IC_\tau)^{\frac{1}{4}} = IC_{\tau_g} = \int (\begin{bmatrix} a_t & \kappa v^2 \end{bmatrix} JJ^T \begin{bmatrix} a_t \\ \kappa v^2 \end{bmatrix})^{\frac{1}{4}} dt. \tag{4.14}$$

where the subscript τ_g indicates the torque squared cost for the gait.

4.6 Optimizer

In 4.3.3, we introduced the measure of efficiency cost. In this section we encode the geometric principles and the cost function described in previous sections into the inertia based gait optimizer algorithm.

We want to find the extrema of the cost function when the derivative goes to the zero. As described in [1], the maximum-displacement for gait parameterization p, occurs when the gradient of net displacement of the cycles with respect to the parameters is zero.

$$\nabla_p g_\phi = 0 \tag{4.15}$$

and maximum-efficiency cycles (normalizing displacement by the inertial cost, $\eta =$

$\frac{g}{IC_{\tau_g}}$) similarly satisfy the condition that the gradient of this efficiency ratio is zero,

$$\dot{p} = \nabla_p \frac{g_\phi}{IC_{\tau_g}} = \frac{1}{IC_{\tau_g}} \nabla_p g_\phi - \frac{g_\phi}{IC_{\tau_g}^2} \nabla_p IC_{\tau_g} = 0 \tag{4.16}$$

Now utilizing the geometric principles described in (4.4) and (3.6), we can evaluate $\nabla_p g_\phi$ and $\nabla_p IC_{\tau_g}$ as a function of Lie bracket DA, curvature and tangential acceleration. This differential equation now is searching for maximum displacement as well as pushing the path in the direction that minimizes the strain energy and tension energy of the curve.

Factoring out a coefficient of $\frac{1}{IC_{\tau_g}}$ from equation (4.16), our algorithm thus finds the maximum-efficiency gait as the equilibrium of

$$\dot{p} = \nabla_p \frac{g_\phi}{IC_{\tau_g}} = \nabla_p g_\phi - \frac{g_\phi}{IC_{\tau_g}^2} \nabla_p IC_{\tau_g} = 0. \tag{4.17}$$

this differential equation is analogous to the equations governing the shape of a soap bubble [1]. $\nabla_p g_\phi$ takes the Lie bracket as an internal pressure seeking to expand the gait cycle to fully encircle a sign-definite region, $\frac{g_\phi}{IC_{\tau_g}} \nabla_p IC_{\tau_g}$ is the bending stiffness that constrains the growth of the bubble.

In the following subsections, we explore each of the terms in (4.17), discussing both their fundamental geometric definitions and how they can be implemented in a direct transcription solver that parameterizes the gait as a sequence of waypoints.

4.6.1 Internal Pressure from the Lie Bracket [1]

The first term in (4.17), $\nabla_p g_\phi$, push the gait towards maximum-displacement cycles. By substituting the approximation from (4.4) into this expression as

$$\nabla_p g_\phi \approx \nabla_p \iint_{\phi a} D(A), \tag{4.18}$$

and noting that variations in the gait parameters p affect the gait curve ϕ but not the systems underlying constraint $D(A)$, we can convert $\nabla_p g_\phi$ into gradient of an area integral with respect to variations in its boundary. We can then invoke a powerful geometric principle, which states "The gradient of an integral with respect to variations of its boundary is equal to the gradient of the boundary with respect to these variations, multiplied by the integrand evaluated along the boundary".

Formally, this multiplication is the interior product of the boundary gradient with the integrand,

$$\nabla_p \iint_{\phi a} D(A) = \oint_\phi (\nabla_p \phi) \lrcorner D(A), \tag{4.19}$$

which contracts D(A) (a differential two-form) along $\nabla_p \phi$ to produce a differential one-form that can be integrated over ϕ.

Implementation of the internal pressure Each waypoint p_i forms a triangle with its neighboring points. whose base defines a local tangent direction $e_\parallel$ as

$$p_{i+1} - p_{i-1} = l e_\parallel \tag{4.20}$$

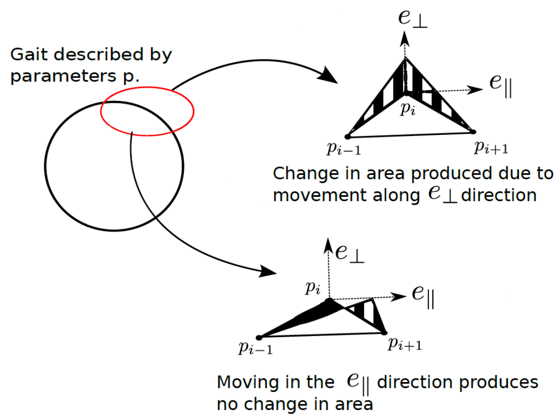

Figure 4.5: This figure illustrates the changes in area caused by moving in the two coordinate directions in the local frame. Moving in the tangential direction $e_\|$ produces no change in area, as the area of the triangle given by half the product of base length and height remains the same.

and a local normal direction $e_\perp$ orthogonal to $e_\|$.

As illustrated in Fig. 4.5, the gradient of the enclosed area with respect to variations in the position of p_i in the $e_\|$ and $e_\perp$ directions is the change in triangles area as p_i moves. Because the triangles area is always one half base times height (regardless of its pitch or the ratio of its side lengths), this gradient evaluates to

$$\nabla_{p_i}\phi a = \begin{bmatrix} e_\| & e_\perp \end{bmatrix} \begin{bmatrix} 0 \\ l/2 \end{bmatrix}. \tag{4.21}$$

4.6.2 Bending Stiffness from the Curvature:

The second term of equation (4.17) takes $\nabla_p IC_{\tau_g}$ as a measure of how acceleration of the gait influence the cost of executing gait.

$$\nabla_p IC_{\tau_g} = \nabla_p \int (\begin{bmatrix} a_t & \kappa v^2 \end{bmatrix} JJ^T \begin{bmatrix} a_t \\ \kappa v^2 \end{bmatrix})^{\frac{1}{4}} dt. \tag{4.22}$$

Applying the Leibniz integral rule and then applying standard calculus operations, results in following equation

$$\nabla_p IC_{\tau_g} = \frac{1}{4} \int \nabla_p (\begin{bmatrix} a_t & \kappa v^2 \end{bmatrix} JJ^T \begin{bmatrix} a_t \\ \kappa v^2 \end{bmatrix})(\begin{bmatrix} a_t & \kappa v^2 \end{bmatrix} JJ^T \begin{bmatrix} a_t \\ \kappa v^2 \end{bmatrix})^{\frac{-3}{4}} dt. \tag{4.23}$$

The gradient component $\nabla_p \kappa$, is computed from curvature of the path which is captured by Reimannian metric. $\nabla_p v$ is related to the systems Riemannian metric by first incorporating the arc-length calculation. $\nabla_p \kappa$ and $\nabla_p v$ state that how the change of curvature and arc-length influence on the change of normal acceleration. Similar to the $\nabla_p v$, $\nabla_p a_t$ is related to the difference of consecutive arc-length. $\nabla_p a_t$ captures the change in tangential acceleration.

Implementation of the curvature: For each triangle the geodesic curvature can be obtained as well as the gradient of it. The gradient term $\nabla_p \kappa$ can be decomposed in

$$\nabla_p \kappa = \nabla_p \kappa_p - \nabla_p \kappa_s \tag{4.24}$$

To find the parameterized curvature (κ_p), we first normalized the coordinate with the metric associated with the waypoint p_i and then in normalized coordinate

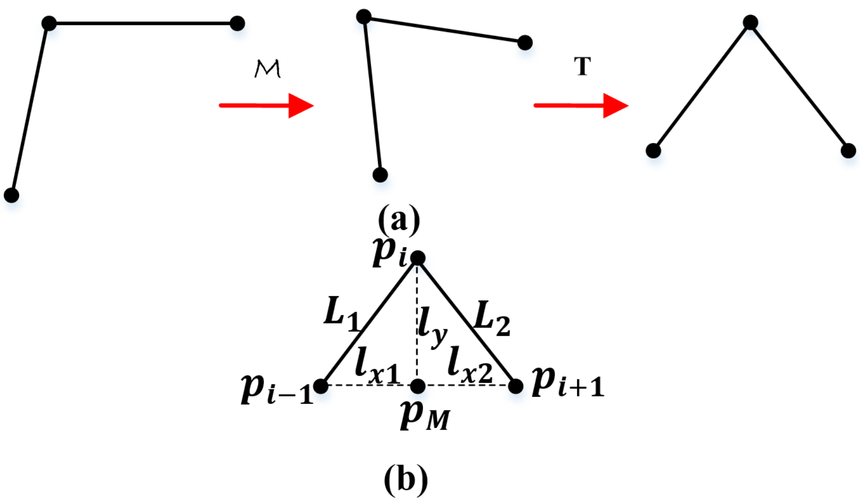

Figure 4.6: (a) Local normalization and rotation for finding the curvature. (b) it shows the normalized triangle with the edge's lengths.

the new triangle formed is rotated such that the two neighboring points are in the equal height (Fig. 4.6).

$$p^N = \begin{bmatrix} p_x & p_y \end{bmatrix} \mathcal{M}_i T \tag{4.25}$$

where N represents the normalized coordinate, p_x and p_y are vectors indicating the waypoints in x and y directions respectively. T is the transformation matrix as shown in Fig. 4.6.

We start with defining the following lengths on the obtained triangle as shown in Fig. 4.6.

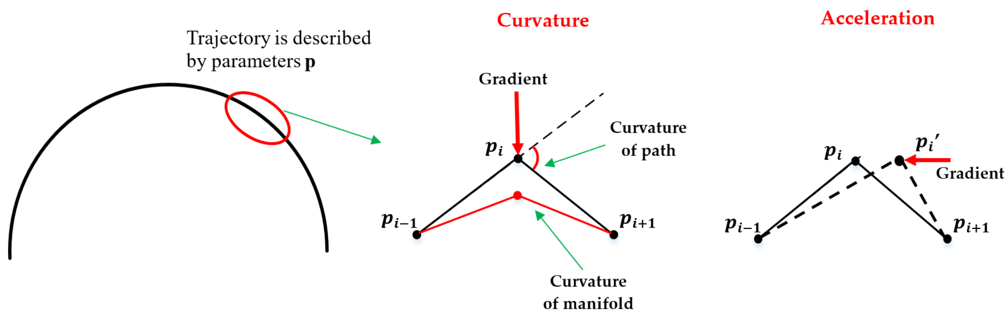

Figure 4.7: This figure illustrates the changes in curvature and acceleration caused by moving in the coordinate in horizontal and vertical directions in the local frame. Moving in vertical direction affect on the curvature and moving in horizontal direction changes the acceleration.

$$
\begin{aligned}
L_1 &= p_i^N - p_{i-1}^N \\
L_2 &= p_{i+1}^N - p_i^N \\
l_y &= (p_i^N - p_M^N) \\
l_{x1} &= (p_M^N - p_{i-1}^N) \\
l_{x2} &= (p_{i+1}^N - p_M^N)
\end{aligned} \tag{4.26}
$$

where p_M^N is the project of p_i^N on horizontal line. Now, the curvature the parameterized curvature can be written as

$$\kappa_p = \frac{\Delta\theta}{\Delta s} \tag{4.27}$$

in which Δs is the arclength and $\Delta\theta$ is the local tangent direction changes which can be obtained from following equations respectively

$$\Delta s = \frac{L_1 + L_2}{2} \tag{4.28}$$

$$\Delta\theta = \arctan(\frac{l_y}{l_{x1}}) + \arctan(\frac{l_y}{l_{x2}}) \tag{4.29}$$

The curvature of the surface is defined as

$$\kappa_s = \frac{dr^T \Gamma dr}{dr^T M dr} \tag{4.30}$$

where the denominator is the path-length such that dr and its gradient can be calculated as:

$$dr = p_i - p_{i-1} \tag{4.31}$$

$$\nabla_{p_i} dr = \begin{bmatrix} 1 \\ \\ 1 \end{bmatrix} \tag{4.32}$$

The metric of each segment is the average of the metrics of endpoints. Therefore, gradient with respect to changes in p_i is thus one half of its gradient over the underlying space,

$$\nabla_{p_i} M = \frac{1}{2} \nabla M \tag{4.33}$$

Similarly, the same calculation will take place for Christoffel symbols. Therefore, to find the geodesic curvature, the κ_s need to be transformed to the same coordinate frame. By taking the gradient from equation (4.27) and (4.30) with respect to the variations in the position of p_i and the differences of the gradient of these two equations produce the final gradient as shown in Fig. 4.7.

The next term is $\nabla_p v$ which is a measure of how pacing in gait affect the cost of executing it. The gradient component can be written as

$$\nabla_p v^2 = \nabla_p \oint_\phi (\frac{dr}{dt}^T \mathcal{M} \frac{dr}{dt}) \tag{4.34}$$

and then applying the standard calculus operations results in

$$\nabla_p v^2 = \oint_\phi (2\nabla_p \frac{dr}{dt}^T \mathcal{M} \frac{dr}{dt} + \frac{dr}{dt}^T \nabla_p \mathcal{M} \frac{dr}{dt}) \tag{4.35}$$

where these gradient ($\nabla_p \frac{dr}{dt}$ and $\nabla_p \mathcal{M}$) are calculated similarly as were shown in equations (4.31) to (4.33).

Implementation of surface tension from the tangential acceleration: For each triangle, the tangential acceleration corresponds to to the difference in the tangential distance from that waypoint to each of its neighbors,

$$\nabla_p a_t = \nabla_p \frac{\Delta v}{\Delta t} = \nabla_p \frac{v_i - v_{i-1}}{\Delta t} = \nabla_p \frac{s_i - s_{i-1}}{\Delta t^2} \tag{4.36}$$

whose gradient with respect to the position of p_i is proportional to difference of gradient of s_i and s_{i-1} relative to p_i as explained in equations (4.31) to (4.33). (Fig. 4.7)

$$\nabla_{p_i} a_t = \frac{\nabla_{p_i} s_i - \nabla_{p_i} s_{i-1}}{\Delta t^2} \tag{4.37}$$

where Δt is the evenly spaced time of each segment.

4.7 Applying Geodesic Concepts to Mobile Robots

We consider purely mechanical systems, whose motion is governed solely by the conservation of momentum such as floating snake and high Reynolds swimmer.

4.7.1 Calculating the Body Velocities

The systems we are dealing with are three-link swimmer as shown in Fig. 4.3. Therefore, we start with calculating the body velocities as it is needed for our systems we are exploring in this chapter. The body velocity of each link which can be calculated from below equations:

$$\overset{\circ}{g}_1 = \begin{bmatrix} \cos(\alpha_1) & -\sin(\alpha_1) & \frac{L}{2}\sin(\alpha_1) & 0 & 0 \\ \sin(\alpha_1) & \cos(\alpha_1) & -\frac{L}{2}(\cos(\alpha_1)+1) & \frac{L}{2} & 0 \\ 0 & 0 & 1 & -1 & 0 \end{bmatrix} \begin{bmatrix} \overset{\circ}{g}_x \\ \overset{\circ}{g}_y \\ \overset{\circ}{g}_\theta \\ \dot{\alpha}_1 \\ \dot{\alpha}_2 \end{bmatrix} \tag{4.38}$$

$$\overset{\circ}{g}_2 = \begin{bmatrix} 1 & 0 & 0 & 0 & 0 \\ 0 & 1 & 0 & 0 & 0 \\ 0 & 0 & 1 & 0 & 0 \end{bmatrix} \begin{bmatrix} \overset{\circ}{g}_x \\ \overset{\circ}{g}_y \\ \overset{\circ}{g}_\theta \\ \dot{\alpha}_1 \\ \dot{\alpha}_2 \end{bmatrix} \tag{4.39}$$

$$\mathring{g}_3 = \begin{bmatrix} \cos(\alpha_2) & \sin(\alpha_2) & \frac{L}{2}\sin(\alpha_2) & 0 & 0 \\ -\sin(\alpha_2) & \cos(\alpha_2) & \frac{L}{2}(\cos(\alpha_2)+1) & \frac{L}{2} & 0 \\ 0 & 0 & 1 & 0 & 1 \end{bmatrix} \begin{bmatrix} \mathring{g}_x \\ \mathring{g}_y \\ \mathring{g}_\theta \\ \dot{\alpha_1} \\ \dot{\alpha_2} \end{bmatrix} \tag{4.40}$$

where $\mathring{g}_x, \mathring{g}_y, \mathring{g}_\theta$ body velocities of the three-link and $dot\alpha_1, \dot{\alpha_2}$ are shape velocities.

4.7.2 Floating Snake

The floating snake is a classic example of systems that undergo the cyclic changes in shape space to achieve net motion [46, 47]. Because the system is not subjected to any external forces, if the system starts at rest, conservation of linear momentum ensures that the velocity of the center of mass remains zero for all time and there is no displacement in XY direction. The floating snake is governed by the inertia hence, the effort required for achieving the rotation can be captured by measuring the torque squared of the joints.

The kinetic energy associated with the three-link floating snake has the form of

$$T = \sum_{i=0}^{N} \frac{1}{2} \mathring{g}_i^T (I_i) \mathring{g}_i \tag{4.41}$$

where N is the number of links, I_i is the links inertia tensor, and $\mathring{g}_i$ is body

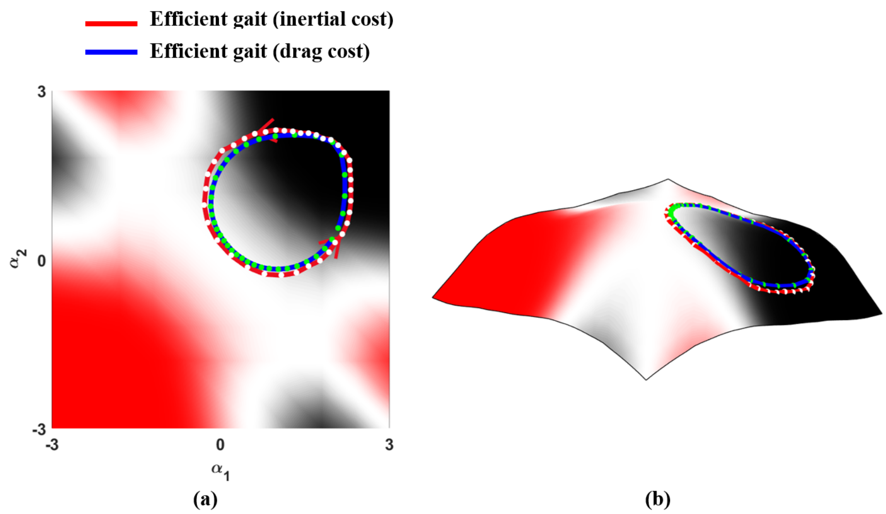

Figure 4.8: (a) shows, max-efficiency turning gait for floating snake. (b) max-efficiency gait is plotted over metric field and demonstrates the region where moving is easier for for the system to move). The black regions are negative and red regions are positive (The direction of rotation of the gaits is clockwise to produce positive displacement). α_1 and α_2 represents the two shape variable of the swimmer.

velocities. Substituting equations (4.38 - 4.40) into equation (4.41), it turns to the form of equation (4.6) and from there it is straight forward to calculate local connection and Riemannian metric. Once the metric is obtained, we can run the optimizer on floating three-link swimmer to find the maximum-efficient gait based on both inertial and path-length cost in the θ-direction over a single cycle. (Fig. 4.8).

As demonstrated in Fig. 4.8 (a), one can observe that the maximum turning gait occurs in either the top right corner or left the bottom corner. One can see the gait found based on the inertia cost is slightly bigger than the one found based on the path-length cost and this is in agreement with the analytical results described in §4.5.1 where states that the path-length cost is proportional to the size of the gait whereas the inertial cost is proportional to the square root of the size of the gait. Moreover, the waypoints on the gait demonstrate how speed changes over the path. Fig. 4.8 (b) shows the surface formed by inertia matrix.

As it is shown in Fig. 4.8 (b) the waypoints on the path found from path-length cost doesn't account for the curvature of the path. Whereas, the distribution of waypoints on the gait found from inertial cost is based on the curvature and acceleration. One can see the waypoints are closer in parts with more curvature which indicates the system moves slower in these parts and vice versa is true for the straight parts.

4.7.3 High Reynolds Three-links Swimmer

For systems interacting at very large Reynolds number, the effect of inertia dominates the viscosity. Kanso et al. in [48], showed that the net locomotion in fish body swimming in high Reynolds fluid occurs due to the transfer of momentum between the fish body and the fluid. This demonstrates that the forces and moments acting on the body by shed vortices are not the only solely contributing in net locomotion. Coupling between the shape dynamics and the surrounding fluid of a system is a key reason for a system to move. Therefore, it is assumed that the effects of viscosity and vortex shedding in the system interacting with high Reynolds fluid are negligible [56, 42].

The drag forces on the object are induced by the displacement and act as directional added masses $\mathcal{M}$ on the object that add with the inertia of the object to produce effective inertia. To do so, we assume that the submerged bodies are hydrodynamically decoupled. This assumption means that the added masses associated with a given body are not affected by the presence of the other bodies. Therefore the kinetic energy associated with three-link swimmer, can be obtained through

$$T = \sum_{i=0}^{N} \frac{1}{2} \overset{\circ}{g}_i^T (I_i + \mathcal{M}_i) \overset{\circ}{g}_i \tag{4.42}$$

where N is the number of links, I_i is the links inertia tensor, $\mathcal{M}$ its added mass and $\overset{\circ}{g}_i$ is body velocities.

Similar to floating snake substituting equations (4.38 - 4.40) into equation (4.42), it turns to the form of equation (4.6) and from there it is straight forward to calculate local connection and Riemannian metric.

We run the optimizer on the three link system to find the gait that maximizes the displacement in the x-direction over a single cycle and then to find the maximum efficiency cycle. Fig. 4.9 (a) depicts maximum displacement and maximum efficiency gait for three-link swimmer moving on the high Reynolds fluid. As one can see in Fig. 4.9 (b), the optimal gait has been shrunk to conform the curvature of the manifold and become closer to geodesic path. Once again, it is shown that the gait obtained using the inertial cost is slightly bigger as predicted in §4.5.1. Furthermore, the gait also is squashed to reduce the regions with higher curvature and increase the regions with lower curvature. As it was shown and discussed in

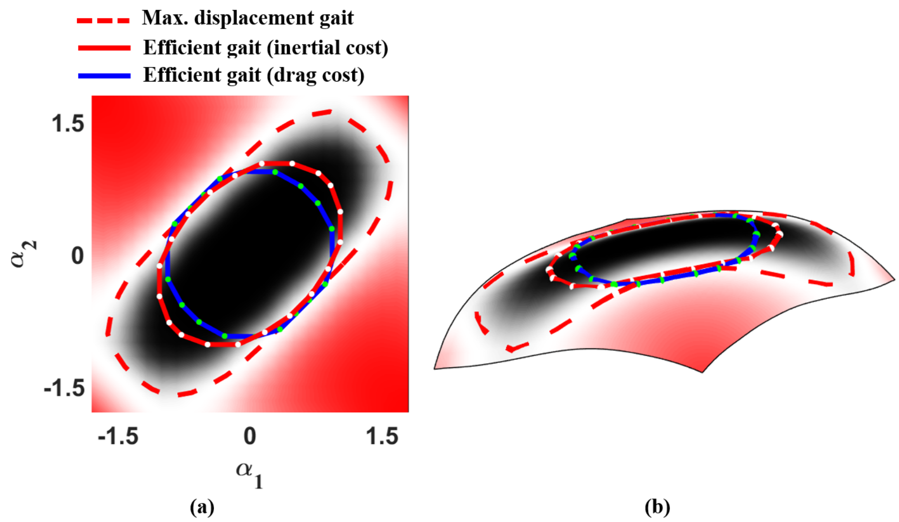

Figure 4.9: (a) shows, max-displacement and max-efficiency gaits for high-Reynolds snake. (b) max-efficiency gait is plotted over metric field and demonstrates the region where moving is easier for for the system to move). The black regions are negative and red regions are positive (The direction of rotation of the gaits is clockwise to produce positive displacement). α_1 and α_2 represents the two shape variable of the swimmer.

§2.2, this effect reduces the cost. In addition, it is shown that the concentration of the points are higher in region with higher curvature and lower in region with less curvature for the inertial gait which causes the system to move slower in region with higher curvature and faster in other parts to reduce the overall cost.

4.7.4 High Reynolds Three-links Swimmer-hydrodynamically coupled

The expressions above are appropriate for considering the motion of systems in which the individual links are hydrodynamically decoupled. This means the added mass associated with each link is independent of the position or velocity of the other links in the system. However, Kanso et al., [48] showed that this assumption is only useful for evaluating the qualitative behavior of the model and doesn't provide accurate numerical solution for the model.

To explore whether this assumption affect on the optimal gait solution, we obtain the motion of the system by solving the hydrodynamicallly coupled equations for submerged three-link swimmer body.

For such a system the kinematic energy of the system is equal to the kinetic energy of the fluid (T_f) and the kinetic energy of the body (T_b)

$$T = T_{\mathcal{F}} + \sum_{i=0}^{N} T_{b_i} \tag{4.43}$$

where N is the number of links and T_{b_i} and T_f are defined respectively as

$$T_{b_i} = \frac{1}{2} \mathring{g}_i^T (I_i^b) \mathring{g}_i \tag{4.44}$$

and

$$T_{\mathcal{F}} = \frac{1}{2} \int_{\mathcal{F}} \rho_{\mathcal{F}} |u|^2 dv \tag{4.45}$$

where I_b is the moment of inertia tensor of the system, $\rho_{\mathcal{F}}$ is the mass density of the fluid, u is its spatial velocity field, dv is the standard volume element on $\mathbb{R}^3$, and $\mathcal{F}$ is the region the fluid occupy. Considering that the flow is irrotational and has zero circulation, the velocity field can be written in form of a potential ϕ

$$u = \nabla\phi \tag{4.46}$$

Going through all the calculation according to [48], results in the form below

$$T = \frac{1}{2}\mathring{g}_i^T(I_{ij}^f)\mathring{g}_j \tag{4.47}$$

Therefore, the total inertia tensor of the system is the sum of the body mass and fluid mass

$$\mathbb{I}_{ii} = I_i^b + I_{ii}^f \tag{4.48}$$

where I_{ii}^f is the moment of inertia of the fluid. Similarly, substituting equations (4.38 - 4.40) into equation (4.47), it turns to the form of equation (4.6) and we can find the local connection and Riemannian metric.

Having the local connection and Riemannian metric, we can plot the curvature constraint function and find the optimal gaits as shown in Fig. 4.10. The results from hydrodynamically coupled and decoupled systems both reveal that although the decoupled solution (analytical) is not precise, it provides a good qualitative comparison of movement characteristic of the system.

4.7.5 High Reynolds Serpenoid Swimmer

Snake locomotion through lateral undulation or Serpenoid is based on a continuous interaction of the snakes entire body with its environment. In this section, we

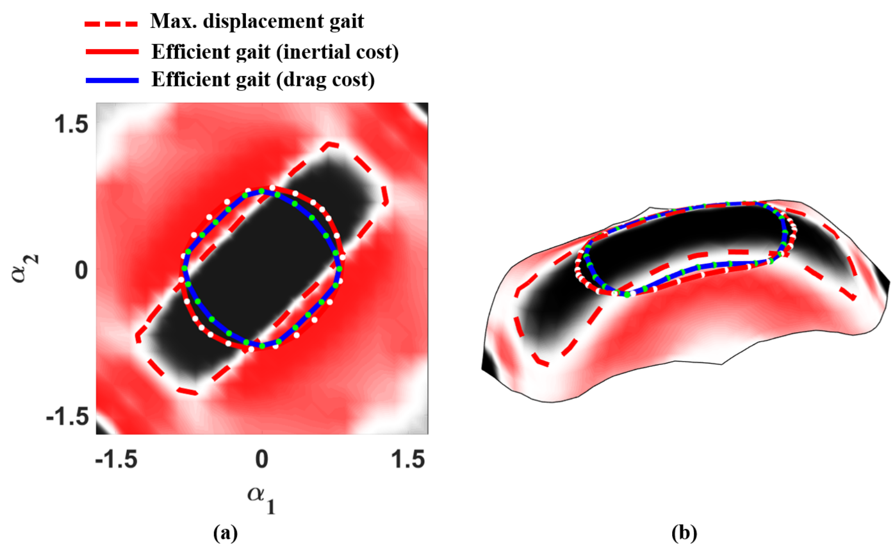

Figure 4.10: (a) shows, max-displacement and max-efficiency gaits for high-Reynolds snake. (b) max-efficiency gait is plotted over metric field and demonstrates the region where moving is easier for for the system to move). The black regions are negative and red regions are positive (The direction of rotation of the gaits is clockwise to produce positive displacement). α_1 and α_2 represents the two shape variable of the swimmer.

investigate the effect of inertia on locomotion of multiple links system interacting with fluid with high Reynolds number.

Before analyzing the high Reynolds serpenoid swimmer, we start with applying both inertial cost and pathlength cost on the low Reynolds serpenoid swimmer as a model which is already explored in our group under the pathlength cost to gain intuition of optimum pacing over the gait. To do so, we consider a circular gait shown in Fig. 4.11 (a) and keep the size of the gait fixed during the optimization so that the speed through the gait can be optimized to reduce the cost (as it was done for the racetrack §2.2). As is shown in Fig. 4.11 (b-d), for both inertial and

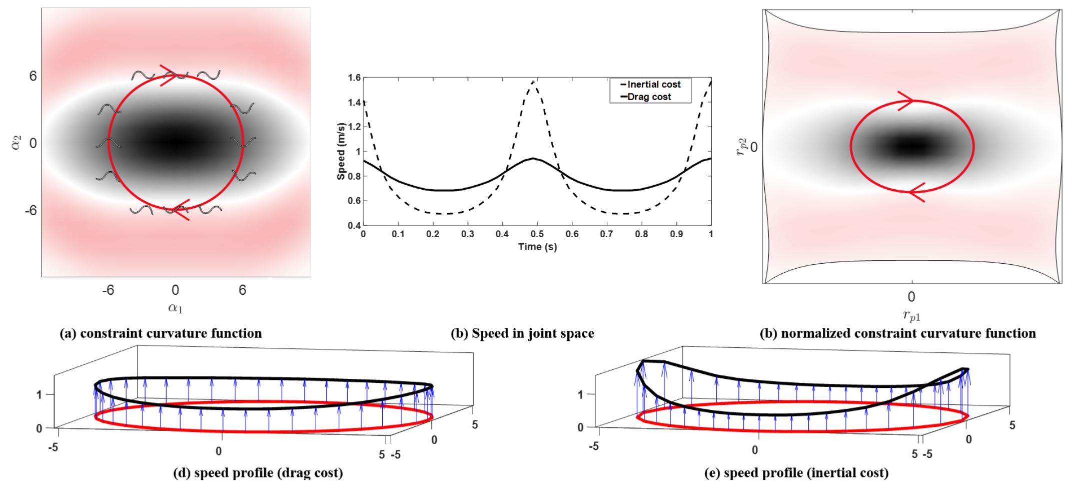

Figure 4.11: Comparison of optimized joints speed from inertial and pathlength costs for low Reynolds swimmer while the gait's size is kept fixed. (a) constraint curvature function for low Reynold swimmer with the circular gait encircling the black region. (b) shows that the joints speed for the pathlength cost has smaller change than the inertial cost in different region of the gait. (c) the illustration of the gait in normalized coordinate now corresponds closely to arclength and helps for better understanding the gait curvature. (d) and (e) demonstrate how the joints speed is changing in different regions of the circular gait for both pathlength and inertial cost respectively.

pathlength cost the speed of shape variables over the gait is not constant and it is varying in different regions causing a surge motion in those regions. However, the speed change for gait found from inertial cost is more significant (Fig. 4.11 (d)). That is because the gait as shown in normalized coordinate (manifold space) Fig. 4.11 (c) is not a circle with constant curvature ans the curvature is varying through the gait. Similar to the racetrack example, the speed is changing over the different region of the gait which is due to the curvature of the manifold (the curvature of the path is constant).

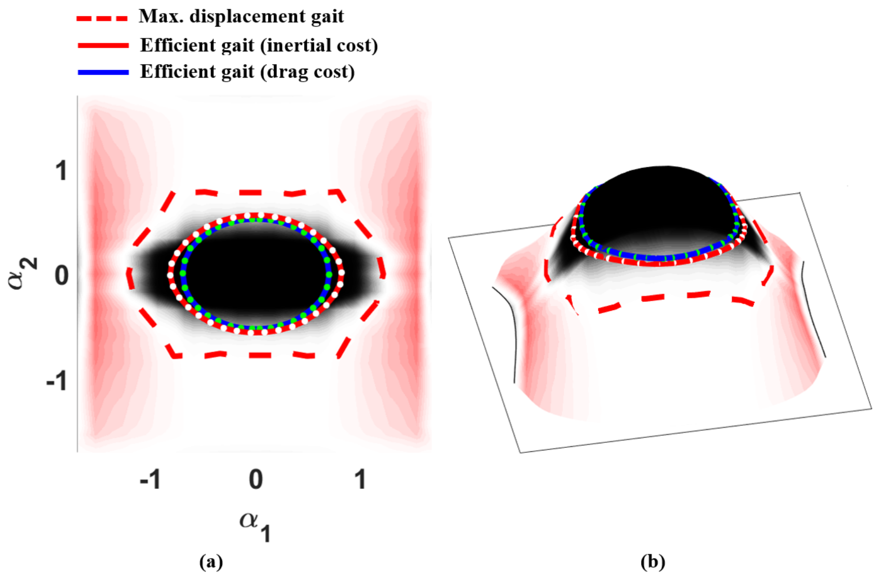

Figure 4.12: (a) shows, max-displacement and max-efficiency gaits for high-Reynolds serpenoid snake. (b) max-efficiency gaits are plotted over a manifold embedded in $\mathbb{R}^3$ and demonstrates the region where moving is easier for for the system to move. The black regions are negative and red regions are positive (The direction of rotation of the gaits is clockwise to produce positive displacement). α_1 and α_2 represents the two curvature modes of the serpenoid snake..

Now we can go further and find the optimal gait for serpenoid system interacting in high Reynolds fluid. Similar to the three-link swimmer, the submerged serpenoid body is assumed to be hydrodynamically coupled. Therefore, substituting equations (4.38) - (4.40) into equation (4.47), it turns to the form of equation (4.6) and we can find the local connection and Riemannian metric.

We run the optimizer on the serpenoid swimmer to find the maximum efficiency cycle based on both inertial and pathlength costs.

The dashed line shows the maximum-displacement gait that traces the zero contour, and the solid line shows the maximum-efficiency gait that captures a more compact area within the sign-definite region. Once again,one can see the gait obtained from inertial cost is bigger than the pathlength cost and the weightpoint distribution are denser in the regions with higher curvature.

4.8 Discussion

In this work, we have incorporated geometric insights to develop a framework for motion planning. This framework, is built to facilitate studying, understanding and designing a gait for robotic locomotion.

We built the cost function for inertial systems based on the concept of geodesic and metric in differential geometry to find an effective and efficient way for robots to move and show how the motion is connected to the system geometry. Then we extended the geodesic cost function to the minimum torque squared problem, which is crucial for systems where there is zero velocity at the start and end points. We showed that a meaningful structure for minimum torque trajectory exists. In fact, we introduced curvature and acceleration as general characteristics of the system that describe the properties of the system in a meaningful way and with fewer terms.

We demonstrated the results of our optimizer for floating snake, the three-link and Serpenoid swimmers in the high Reynolds fluid which has metric induced by inertia and compared the results with the results obtained from pathlength cost function. The results revealed that, the gaits found from the inertia based optimizer are a little greater than the gaits found by drag based optimizer which matches with the mathematical equation we derived (the inertial cost is proportional to square root of the size of the gait whereas the drag cost is proportional to the size of the gait). Furthermore, we demonstrated the pacing effect for inertial systems and how the weigh-points are distributed through the gait. The results revealed a structure for the optimal solution for these types of robots.

Chapter 5: Impact Bounce Prediction Using Geometric Mechanics

5.1 Introduction

In many high-speed processes including manufacturing equipment or robots, some part of bodies might be vulnerable to dynamic impact, therefore it is very crucial to understand the impact and determine the orientation and position of that in order to adjust the robot with the impact force (reduce the impact force) or even make use of the impact to reduce the power consumption. The effect of collisional contact on the motion is determined by the momentum balance equations and collisional constitutive relations. But there are still many questions need to be answered: how to construct a sensible and general law for the collision; are the existing method a good basis; can we make a prediction model of impact effect based on objects geometry? To understand the essence and necessity of impact dynamic, it is first necessary to understand the definition of the impact in the first place. Going through this process then guides us in a very natural fashion toward the various application of knowing the impact. One way of understanding the impact in a solid object is investigating the impact that occurs under the tension of the string attached to the free flight object.

The momentum of a moving object in free flight can be redirected by pulling on a tether connecting it to the ground or a heavier object. The application of this principle is used by jumping spiders [57] to maneuver while jumping and has been used by astronauts to maneuver during spacewalks [58].

As a step towards the goal of enabling robots to be able to move with this agility, we seek to understand how much and what kind of control authority can be achieved by bouncing against a cable, and in particular by setting up the right pre-bounce initial conditions so that no active feedback is needed during the moment of impact. In this chapter, we consider the fundamental case of planar object anchored by a tether attached to either its center of mass or an outboard point, as illustrated in Fig. 5.1. This tether is slack for most of the motion, then applies a short impulse when the distance between its anchor and attachment point to the body matches its actual length. This impulse can be considered as an impact of the body against a virtual wall that is perpendicular to the tether and passes through the attachment point.

We identify the space of post-bounce motions available by changing the angle of the tether relative to the body's initial motion or the position of the attachment point relative to the center of mass, and in particular consider the ways in which the alignment between the velocity, tether, and offset direction of the attachment point exchange energy between the translational and rotational modes of the body. Along the way, we also identify the accuracy of using an impulse equation that treats the bounce as instantaneous versus modeling the tether as deformable spring. A key result in this chapter is the identification of a tether configuration that converts an initial pure translational velocity of the puck into a pure rotational motion after the bounce.Moreover, we develop a visualization tool that demonstrates how energy is

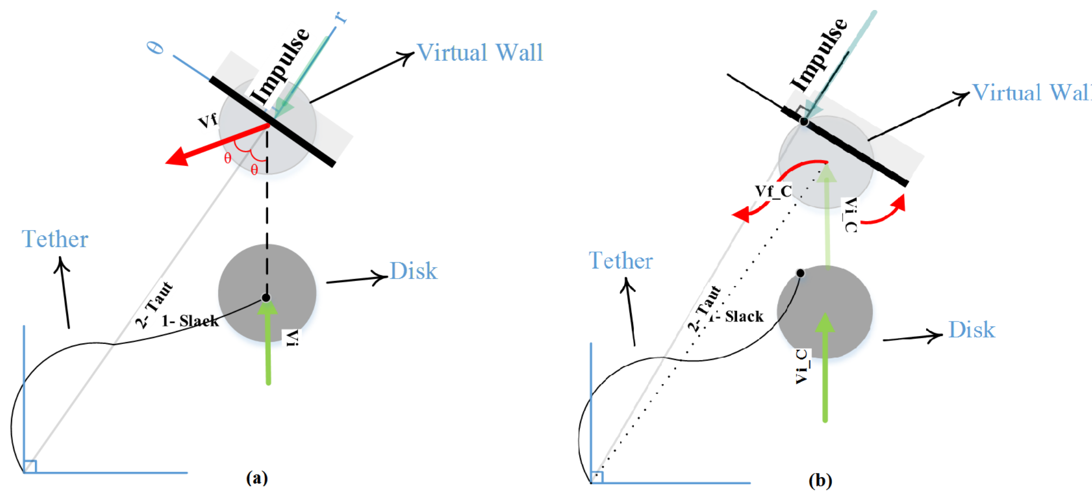

Figure 5.1: Bouncing a projectile against a tether (a) attached to the center of mass, and (b) attached to the outboard from the center of mass.

transferred from translational to rotational and vice versa. In addition, we explore the energy dissipation effect after the bounce using our developed vitalization tool.

This chapter is organized as follows: Section 2 puts our work into the context of previous studies on tethered systems. Section 3 describes the modeling of the system in terms of both the full dynamic equation and an impulse approximation. Section 4 considers several case studies of the system dynamics with different initial conditions. Section 5 introduces a visualization tool that can predict the change of energy after the bounce. Section 6 describes the experimental results that we implemented on a physical realization of our idealized system. Finally, Section 6 presents a discussion on the relevance of the results and highlights directions for future work.

5.2 Literature Review

Our analysis in this chapter draws on prior research efforts regarding modeling the impact, casting manipulators, string pendula, and balls bouncing against walls.

5.2.1 Modeling the impact

Our work builds on the body of the discontinuous model of impact. This approach assumes that impact happens in a very short time, therefore there is no significant change in the configuration of impacting bodies [59]. This approach is based on solving a set of algebraic impulse-momentum equations that account for discontinuities in the system velocities during the impact event. Thus, the generalized impulse-momentum equation for all the bodies in the system is derived. The solution of these equations produces a discontinuity in the joint reactions as well as in the velocities. This method is mostly used for impact between rigid bodies. This approach also referred to impulsemomentum or discrete methods [59].

Poisson defined the kinetic quantity that accounts for normal impulses and relates them in contact point during the impact. Whittaker [60] proposed a model based on Newtons model that defined the coefficient of restitution as a relationship between the normal components of the velocities before and after the impact at the contact point. Routh [61] defined the coefficient of restitution as a kinetic quantity that relates the normal impulses and restitution phases. He considered the change in slip direction during the impact. Brach [62] [63] proposed a ratio of the tangential and normal impulse component by modifying Newtons model. The tangential components are determined by frictional impulses and are a constant fraction of the normal impulse [62]. This coefficient is appropriate for the oblique impact problem and is an equivalent to the friction coefficient. In addition, he defined another parameter to relate the tangential velocities before and after impact and showed this coefficient and the coefficient between the tangential and normal impulse are related [63].

Keller [64] developed a differential equations to present the impact. Therefore, impact is considered as a normal component applying in finite time which helps to determine the events that happen during the impact. Also, Keller modified Poissons model and proved that an increase in energy during the impact is impossible. His study has also shown how the direction of sliding changes during impact and what effect it causes for determining the frictional force.

Wang and Mason [65] used Rouths graphical method to solve the impact problem. They classified the possible modes of impact and used Poissons and Newtons models of restitution to and derive analytical expressions for impulse. Also, they identified the impact conditions under Newtons and Poissons models give the same solution.

Hurmuzlu and Chang [66] developed a methodology to solve the impact problem where one end of a planar kinematic chain impact a horizontal surface while the other end is stationary on the surface. They developed their work based on Brach theorem where the rigid bodies do not contact each other before the collision. In Brach method, since the contact happens only in one point, separation would be at the same point. The advantages of their method over Brach method was, their method could successfully predict rebounds at both ends and yields physically consistent transitions among the various cases associated with lateral and horizontal motions at the contact points. Han and Gilmore [67] developed a similar approach, using an algebraic formulation of motion equations, Poissons model of restitution and Coulomb's law to define the tangential motion.

5.2.2 Casting Manipulation

In order for robots such as mobile robots to perform in uncertain and unstable environments, it is crucial to extend their workspace using their mobility. However, mobile robots such as legged and wheeled robot still have difficulty in moving in wasteland, steep slopes, etc. Casting manipulators are robots that can throw an end effector which is attached the robot by a tether. A key aspect of casting manipulation is midair control of the end-effector by applying an impulsive force through the tether that causes the end-effector to approach a desired target [68]. When the moving body is arrested by the tether during the flight, it rebounds. This phenomenon can be thought that there is a virtual wall perpendicular to the string. This idea has been experimented in Kendama game [69]. Also, [70, 71] considered the effects of bouncing with an off-center attached tether, but that they didn't examine the geometry of bounce direction and speed. In this research we utilize the idea of the virtual wall that happens in impact time and will consider the geometry and physics of the moving body with off-center attached tether after the impact.

5.2.3 String Pendulum

Our system is a special case of a string pendulum, a class of systems in which the element connecting the pendulum bob to the pivot can only provide tension, and acts as a high-stiffness spring when taut. Prior research on these systems mostly has focused on the periodic motion of such pendula, as in [72]. In our work here we focus on the transient response around the slack-taut transition, rather than the long-term dynamics.

5.2.4 Classic case of a bouncing ball

The dynamics of the system we are considering are very similar to those of a ball bouncing against a wall [73]. When modeled as a point mass, the ball's velocity normal to the wall changes signs while its velocity parallel to the wall is unaffected, so that its angles of incidence and reflectance are the same. For a ball with finite radius, the angle of reflection will in general be different from that of the point mass, as some of the ball's kinetic energy is transferred into or out of its spinning mode [74]. Our tethered-projectile model extends this concept by allowing the bounce point to be inside the perimeter of the moving object, opening up the potential for a wider variety of post-impact behaviors. Spong [75] investigated the controllability of an air hockey puck sliding on a frictionless table when it is struck by a mallet. He assumed the velocity of the mallet as the control input, then he used " Routh impact model" to show the reasonable set of velocities that depends on whether or not the relative sliding between the puck and mallet terminates during the impact which restricts the size of the reachable set.

5.3 Background

In this section, we cover some important definitions and concepts in impact dynamics.

5.3.1 The Definition of Impact

Impact happens in the collision of two or more bodies, that involves large acceleration, finite changes in velocities and small changes in position and orientation [76] [77]. Other effects are directly related to the impact phenomena including, vibration on the system, deformation at the point of contact zone and energy dissipation [78]. Moreover, while impact is happening, discontinuity in geometry occurs and material properties may altered by the impact itself [59].

5.3.2 Impact VS. Contact

Now it is important to note the difference between impact and contact. In impact, interactions between the bodies happens in a short period of time, therefore there is no significant change in the configuration of the bodies. On the other hand, in contact the interaction forces act in continuous manner [59].

5.3.3 Different Types of Impact

Basically, there are four types of impact can be defined between two bodies: (a) central or collinear, which is when the impact in alignment of center of mass of two bodies; (b) eccentric, is the case that, the impact direction is not in alignment of at least one of the body; (c) direct, if initial velocities of the bodies are in the same line of impact; (d) oblique, happens when at least the initial velocities of the body is not in the same line of impact [59].

5.3.4 Phases of Impact

Generally, any impact may be considered in two phases: The first phase is the compression phase. It starts when the body touch the surface or second body and then the body start deforming in the direction of the impact and the relative velocity will reduce until it reaches to zero. This phase is called maximum compression or maximum penetration. The second phase is referred as restitution phase. It starts from the end of first phase and ends when bodies separates from each other [78]. The restitution coefficient is introduced to account for dissipation of energy during impact process [79] [80]. The coefficient of restitution depends on many parameters including geometry of bodies in contact, velocity before contact, material properties, times in which contact takes place and friction [80] [59].

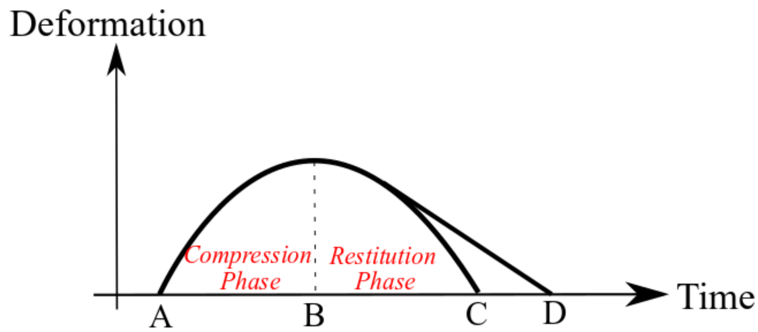

Figure 5.2: (a) perfectly elastic, line OAC, where no energy is lost;(b) perfectly plastic, line OA, where all energy is lost and the deformation is permanent;(c) partially elastic, line OAD, with energy loss but no permanent deformation;(d) partially plastic, line OAB, with energy loss and permanent deformation.

5.3.5 Impact Based on Coefficient of Restitution

Regarding the coefficient of restitution, impact can be considered as below: Elastic collision: In elastic collision between two bodies, the total kinetic energy between the two bodies after the impact is equal to the total kinetic energy of both bodies before the impact. In other word, the energy is conserved and there is no energy lost in the system. Inelastic collision: In inelastic collision, some part of energy converts to the other form of energy such as vibration, heat and e.g. This can be considered as a collision which energy is not conserved. It is worth to note that despite the fact that in inelastic collisions the energy is not conserved, they obey conservation of momentum [81].

5.3.6 Approaches to Calculate the Impact

The evaluation in contact forces can be considered from two different approaches which are namely, the *continuous* and *discontinuous* approaches.

The continuous approach, assumes that the impact forces happens in a continues manner during the impact [78]. To simulate the continuous behavior, the compliance or continuous contact models are used where the impact force is a function of local indentation. This method is suitable for long impact duration and returns more efficient and accurate results [78].

The *discontinuous approach* assumes that impact happens in a very short time, therefore there is no significant change in configuration of impacting bodies [59]. The discontinuous approach is based on solving a set of algebraic impulse-momentum equations that accounts for discontinuities in the system velocities during the impact event. Thus, the generalized impulse-momentum equation for all the bodies in the system is derived. The solution of these equations produces a discontinuities in the joint reactions as well as in the velocities. This method is mostly used for impact between rigid bodies.

5.4 Modeling of the System and Coordinates

Our model system for this study consists of a puck (a solid disk moving in the plane) anchored to the ground by a stiff, elastic, and massless tether. We consider this system under two conditions. In the first, simpler case, the tether is attached to the puck's center of mass;[1] in the second case the tether is attached to a point outboard from the center of mass. This outboard attachment allows for a variable moment arm between tether's line of action and the center of mass, and thus for different amounts of energy to be transferred between translational and rotational modes at impact.

Fig. 5.3 illustrates the coordinates we use to model this system, where x and y are the position of the puck with respect to the global reference frame and the puck's initial velocity is in the y direction. The tether is anchored to the origin of the global frame, and is at an angle β with respect to this frame; it has a base length L_0 when it is taut and not stretched. For a tether attached outboard from the puck's center of mass, the line connecting the attachment point and center of mass makes an angle φ with the direction of motion.

When using an impulse model of the bounce dynamics, as in §5.4.2, it is useful to transform the system dynamics into a frame whose axes are aligned with or orthogonal to the tether, as illustrated in Fig. 5.4, and to measure the tether angle with respect to the initial direction of motion, rather than the x axis of the global frame. It is also useful to introduce an "offset angle" α that represents the declination of the line from the tether attachment point to the center of mass, relative to the tether's line of action.

[1]The tether is out of the plane of the puck, and so is allowed to intersect with it.

5.4.1 Full Equations of Motion

The tethered-puck system described above exhibits hybrid dynamics, in that it obeys free-flight equations of motion

$$\ddot{x} = \ddot{y} = \ddot{\varphi} = 0 \tag{5.1}$$

when the tether is slack, we define Lagrangian, L which is a map from the tangent space of the configuration manifold to the reals. For mechanical systems, the Lagrangian is defined as the difference of kinetic energy and potential energy.

$$\mathcal{L} = \mathrm{KE} - \mathrm{PE} \tag{5.2}$$

where $\mathcal{L}$ is the Lagrangian term for a system and the kinetic energy is

$$\mathrm{KE} = \frac{1}{2}\begin{bmatrix} \dot{x} & \dot{y} & \dot{\varphi} \end{bmatrix} \begin{bmatrix} m & 0 & 0 \\ 0 & m & 0 \\ 0 & 0 & I \end{bmatrix} \begin{bmatrix} \dot{x} \\ \dot{y} \\ \dot{\varphi} \end{bmatrix} \tag{5.3}$$

relatively the potential energy is

$$\mathrm{PE} = \frac{1}{2}K(L - L_0)^2 \tag{5.4}$$

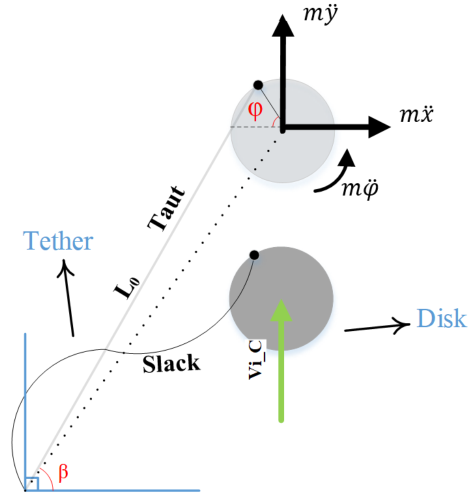

Figure 5.3: Coordinates of the dynamic model.

where

$$L = \sqrt{(x + R\cos(\varphi))^2 + (y + R\sin(\varphi))^2} \tag{5.5}$$

is the length of the spring, and L_0 is the neutral length of the spring. Now we can form the systems equations of motion, as Euler-Lagrange equations

$$\frac{d}{dt}\frac{\partial \mathcal{L}(q,\dot{q})}{\partial \dot{q}_i} - \frac{\partial \mathcal{L}(q,\dot{q})}{\partial q_i} = 0 \tag{5.6}$$

The motions considered in this chapter, starts with free-flight mode where the tether is slack and nominal tether length $L < L_0$. When it reaches to slack-taut transition condition of $L = L_0$, then the mode transitions to spring-mass dynamics with the tether stretching to $L > L_0$.

5.4.2 Impulse Approximation

In many situations involving impacts, the duration of contact is short enough that the forces applied to the moving system can be modeled as an impulse, allowing the final velocity to be determined by conservation of energy and momentum instead of evaluating the full dynamic equations over the contact period. For the puck-tether system, these conservation laws lead to four equalities relating the puck's velocity before and after the bounce. Three of these equations are given by the net change of momentum,

$$\begin{bmatrix} m & 0 & 0 \\ 0 & m & 0 \\ 0 & 0 & I \end{bmatrix} \begin{bmatrix} \Delta v_r \\ \Delta v_\theta \\ \Delta \dot{\varphi} \end{bmatrix} = \begin{bmatrix} J \\ 0 \\ \vec{J} \times \vec{R} \end{bmatrix} \tag{5.7}$$

where Δ indicate the difference of the velocity before and after the impact and $\vec{R}$ is the position of the center of mass relative to the attachment point as measured in the tether-aligned coordinates. The first equation means that the string applies an impulse $\vec{J} = J\hat{r}$ to the puck, changing the magnitude of its linear momentum along the tether by J. The second equation implies that the tether cannot apply any forces perpendicular to itself, so the center-of-mass's momentum (and thus velocity) in that direction is unchanged. Third, this linear impulse applies a moment to the system around the center of mass, so that its initial and final angular momenta are related.

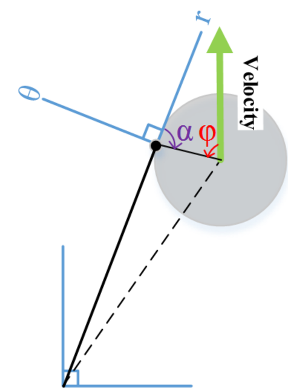

Figure 5.4: Extra coordinates useful for the impulse model.

Fourth and last, a perfectly-elastic tether dissipates no energy during the impact, so the system's initial and final kinetic energies are equal,[2]

$$\Delta \mathrm{KE} = \frac{1}{2}\begin{bmatrix}\Delta v_r & \Delta\dot{\varphi}\end{bmatrix}\begin{bmatrix} m & 0 \\ 0 & I \end{bmatrix}\begin{bmatrix}\Delta v_r \\ \Delta\dot{\varphi}\end{bmatrix} \tag{5.8}$$

Given these relationships, we can solve (5.7) and (5.8) as a set of simultaneous equations to extract the final translational and rotational velocities from a set of known pre-impact initial conditions. Note that we need never solve for the impulse J: it acts as a constraint on the dynamic equations that mandates a proportional change in linear and angular momentum, and can be factored out of the system by combining first and third row of (5.7). Additionally, because the exit condition for the impulse equations is that the tether has returned all of its elastic energy to

[2]This formula can be generalized to dissipative systems via a coefficient of restitution as discussed in §5.6.2.

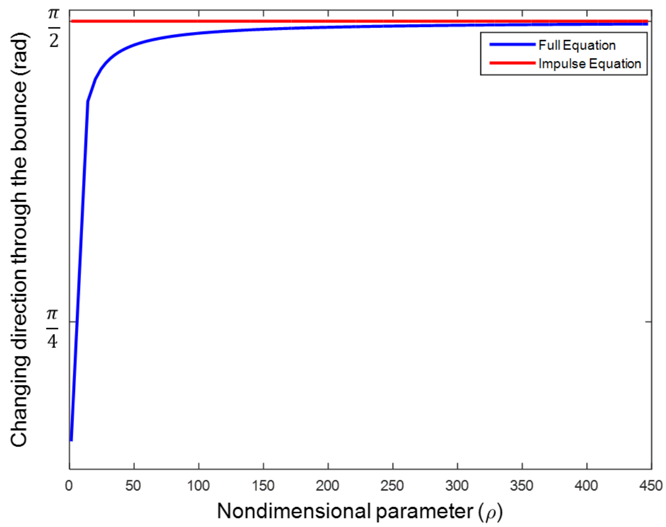

Figure 5.5: The post-bounce direction of velocity for a puck with a 45° tether attached at the center of mass, as a function of the system's characteristic parameter ρ from (5.9).

the puck and thus is at $L = L_0$, the equations automatically exclude any solution that would put the tether in compression.

5.4.3 Convergence Study on Impulse Equations

The impulse equations in §5.4.2 assume that the bounce duration is "small" relative to the time-scale of the system, and in particular that the angle of the tether with respect to the global frame changes very little during the impact. The accuracy of the impulse approximation therefore depends on a non-dimensional parameter ρ that is the ratio of natural frequency of the spring-mass mode of the system and

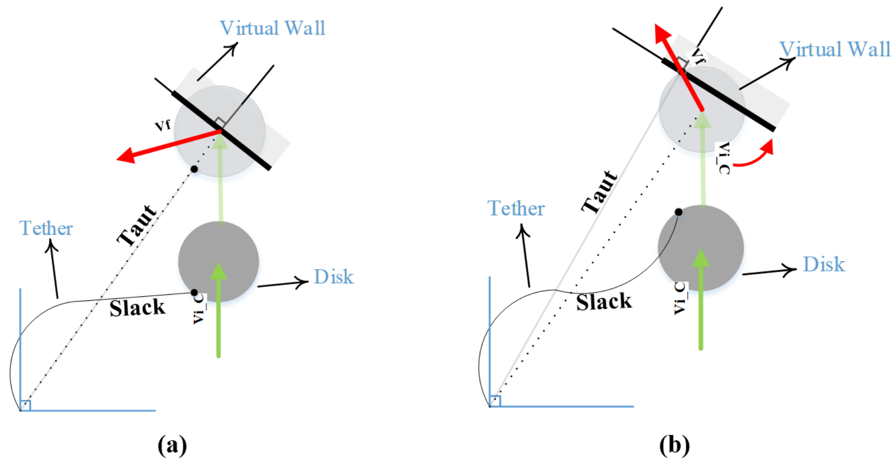

Figure 5.6: Bounce direction with outboard tether (a) when the tether's line of action passes through the center of mass, the puck's velocity is redirected in the same manner as seen when the tether is attached to the center of mass. (b) when the tether's line of action does not pass through the center of mass, it rebounds along a shallower angle.

the rate at which the tether is rotating at the start of the impact,

$$\rho = \frac{\omega_n}{\dot{\theta}} = \sqrt{\frac{k}{m}} \cdot \frac{L}{v^{\theta}}. \tag{5.9}$$

To validate our use of the impulse equations, we conducted a convergence study between their results and those of the full equations in (5.2)–(5.6), with a 45° tether attached to the center of mass with varying ρ. As illustrated in Fig. 5.5, the two equations have essentially converged for $\rho > 100$. Our experimental system (described in §5.8) has $\rho > 850$, well within the region of convergence.

5.5 Exploring Bounce Direction with the Impulse Equations

With the impulse model for tether-bounces in hand, we can now explore how the direction in which the system bounces depends on the orientation of the tether, where it is attached to the puck, and the mass distribution of the puck.

When the tether is attached to the center of mass, (5.7) and (5.8) have a simple solution: the velocity along the tether is reversed, and the velocity orthogonal to the tether stays the same. As illustrated in Fig. 5.1, this motion is equivalent to bouncing a point mass off of a virtual wall, with equal angles of incidence and reflection. Such reflections allow for some interesting trajectories, such as a 90° bank shot by placing the tether at 45°, but far more interesting phenomena occur when we consider pucks with outboard tether attachments.

As illustrated in Fig. 5.6, the bounce direction with an outboard tether is strongly influenced by the relative angle between the tether and the line between the attachment point and the center of mass: aligning these directions produces the same "reflected particle" bounce seen for a tether attached to the center of mass as in Fig. 5.6a , but the puck bounces by a shallower angle when the tether is at a different angle from the tether attachment as in Fig. 5.6b. From the standpoint of our momentum equations, this change in bounce direction originates in third row of (5.7), where the offset angle determines the effective moment arm in the rotational impulse, and thus the proportion of energy that is directed into spinning the puck instead of redirecting its translational velocity.

To further understand the bounce dynamics of this system, we consider how the system's velocity evolves for different offset angles under two conditions: When the tether is at a 45° angle to the initial velocity, and when it is directly inline with the velocity.

5.5.1 Outboard Attachment With 45° Tether

The bounce directions and relative translational output speed of the puck generated by a half-circle sweep of the attachment point and a fixed[3] tether angle of 45° are plotted in Fig. 5.7a. As expected, the puck makes a right-angle turn with zero change in speed when there is zero offset between the tether and attachment angles, mimicking a system with the tether attached at the center of mass. Likewise, it experiences the smallest change in direction when the tether is at right angles to the attachment, and thus provides the largest ratio of angular-to-linear impulse; this large ratio means that the system experiences a large rotational acceleration which slackens the tether before the linear momentum is fully redirected. Between these two points, however, we see that the greatest speed change does not occur at this configuration, and in fact corresponds to an offset angle of 45°.

The difference between the minimum-deflection and maximum-deceleration points is an impedance-matching effect between the system's translational and rotary inertias, in which the impulse applied by the tether most efficiently imparts rotational energy into the system when the moment-arm of the tether force

[3]On a physical system with a fixed tether length, the tether angle at impact would of course vary with the offset angle. For a sufficiently long tether, however, this change of angle is negligable.

around the center of mass is equal to the puck's radius of gyration, as illustrated in Fig. 5.8. This condition corresponds to case where the square of the ratio between the magnitudes of its linear and rotational components is equal to the the ratio between the puck's translational and rotational inertia,

$$\left(\frac{JR\sin\alpha}{J}\right)^2 = \frac{I}{m}. \tag{5.10}$$

For the puck, which has rotational inertia $I = \frac{1}{2}mR^2$, (5.10) is satisfied when $\sin^2\alpha = \frac{1}{2}$, leading to maximum energy transfer (and thus speed change) at $\alpha = \frac{\pi}{4}$ and $\alpha = \frac{3\pi}{4}$.

The offset angle that results in the maximum change in the puck's speed depends on its mass distribution. If we replace its solid-disk geometry with a thin ring of the same radius, for which $I = mR^2$, then (5.10) is satisfied for $\sin^2\alpha = 1$. This equation has only a single solution in our domain, $\alpha = \frac{\pi}{2}$. As illustrated in Fig. 5.7b, this means that the ring's maximum change in velocity is collocated with its minimum deflection.

The evolution of the maximum-deceleration points as a function of I/mR^2 from a pair of solutions evenly distributed about $\alpha = \frac{\pi}{2}$ into a single solution at $\alpha = \frac{\pi}{2}$ with a merge-point at $I = mR^2$ is plotted in Fig. 5.7c. Note that for pucks whose moment of inertia is greater than $I = mR^2$, (5.10) has no solution, indicating that the tether's impulse inefficiently applies energy to the rotational mode for any angle; however, the most efficient transfer of energy for these systems still occurs when $\alpha = \frac{\pi}{2}$.

5.5.2 Tether Inline with Velocity

The effects of offset between the tether and moment arm, and of changing the system's moment of inertia, are even more strongly demonstrated if we consider a tether anchored directly behind the puck. As such a tether is inline with the system's initial linear momentum, it cannot deflect the system at the bounce, and, as illustrated in Fig. 5.7d, any "change in direction" it produces can only be a complete 180° rebound, and there is a range of offset angles for which there is *no* change in direction: the puck continues moving in its pre-bounce direction, albeit at a slower speed.

An interesting effect appears at the offset angle where the puck transitions from rebounding to carrying on in its original direction: The puck goes to zero translational velocity and instead spins in place. This "deadspin" effect is a special case of the maximum-deceleration point we identified for the 45° tether, where placing the tether's effective moment arm at the puck's radius of gyration now completely transfers its kinetic energy into the rotational mode. The completeness of this energy transfer is enabled by the alignment of the puck's velocity with the tether; in the 45° degree case, the component of the puck's momentum that was orthogonal to the tether represented energy in the system that was unable to interact with the tether.

As was the case for the maximum-deceleration points for the 45° tether, the deadspin points of the 90° tether satisfy the condition $\sin^2\alpha = I/mR^2$, and merge into a single solution for $I = mR^2$ as illustrated in Fig. 5.7e–f. For moments of iner-

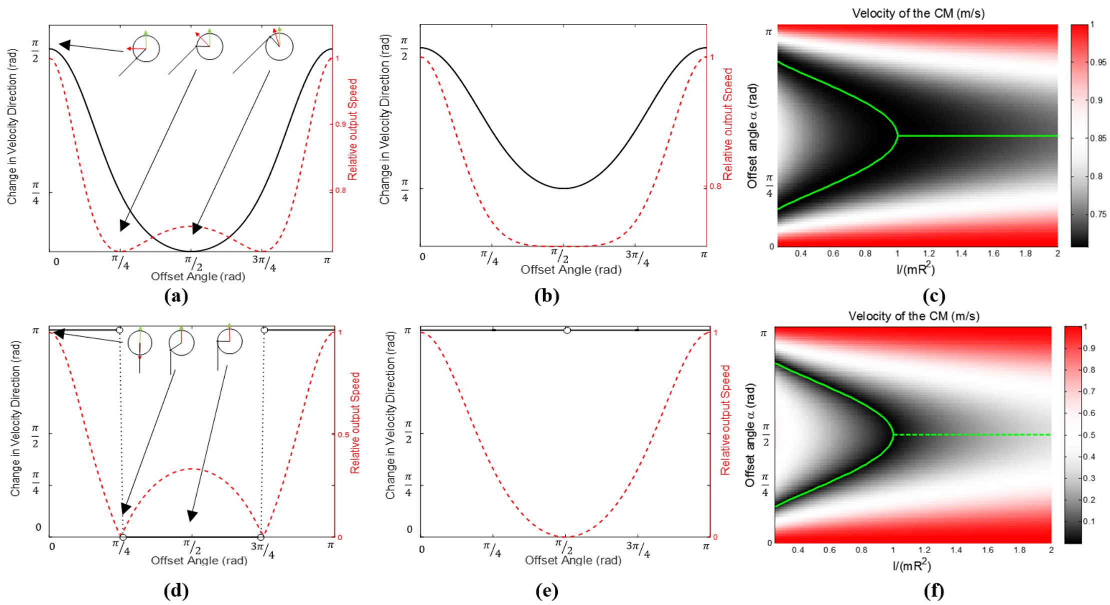

Figure 5.7: Bounce direction and magnitude as a function of tether and offset angle. (a) with a 45° tether angle, the puck experiences maximum deflection (change in direction) when the offset angle is zero, maximum deceleration when the offset angle is $\frac{\pi}{4}$ or $\frac{3\pi}{4}$, and minimum deflection when this angle is $\frac{\pi}{2}$. (b) a puck that is a ring (instead of a solid disk) experiences both maximum deceleration and minimum deflection at an offset angle of $\frac{\pi}{2}$. (c) for inertia ratios of $i/mr^2 < 1$, the maximum deceleration occurs when the tether's line of action is tangent to the radius of gyration. the locus of such points (which satisfies 5.10) has two branches which merge together when the inertial ratio reaches unity. Above this limit, maximum deceleration occurs when the tether's line of action has a maximal moment arm around the center of mass. (d) when the tether is anchored directly behind the impact point, the maximum deceleration removes all translational velocity from the puck, leaving it in a "deadspin." (e) the two deadspin points merge together for a ring. (f) the deadspin points for a 90° tether trace out the same locus as did the maximum-deceleration points of the 45° tether. Note that the maximum-deceleration points for inertia ratios greater than 1 are *not* deadspins.

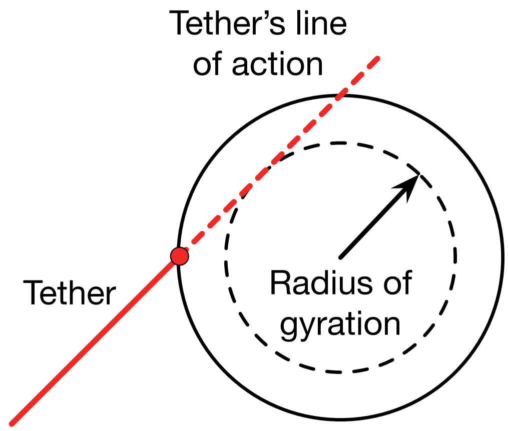

Figure 5.8: The tether impulse most efficiently transfers energy into the system's rotational mode when the tether's line of action is tangent to the puck's radius of gyration (the root-mean-square radius of its mass elements or, equivalently, the radius of a thin ring with the same moment of inertia). This arrangement balances the linear inertia of the puck with its rotational inertia relative to forces acting along the tether.

tia above this merge-point, however, there are no dead-spin solutions: the tether's line of action is always inside the radius of gyration, and cannot transfer energy or momentum into the rotational mode efficiently enough to prevent rebound.

5.6 Visualization method for prediction the velocity and its direction (energy method)

In order to enable better visualization and understanding of the effect of the object's geometry and its inertia on the impact, a mathematical framework that describe the physical motion of the system is proposed. This is achieved by defining the *energy ellipse* and *impact line of action*.

5.6.1 Line of action and energy ellipse

The geometric iterpretation of the energy equation can be represented by the energy ellipse which is defined by the inertia matrix of the object. It states a level set of kinetic energy function of the system and demonstrates how the energy changing from one form to the other form after the impact. Therefore, according to (5.8) we can find the major and minor axis of the energy ellipse

$$a = \sqrt{\frac{2\text{KE}}{m}} \tag{5.11}$$

$$b = \sqrt{\frac{2\text{KE}}{I}} \tag{5.12}$$

The impact line of action describes the states that the momentum changes along that line. This ratio can be written as

$$\tan\gamma = \frac{\Delta\dot{\varphi}}{\Delta v_r} = \frac{mR\sin\alpha}{I} \tag{5.13}$$

Fig. 5.9 illustrates the energy ellipse and line of action of the impact. As shown in Fig. 5.9 the horizontal axis represents the change in velocities and the vertical axis represents the change in angular velocities before and after the impact. The two intersection points of red lines and ellipse correspond to the velocities and rotational velocities of the object before and after the impact. For instance, if the puck moves with translational velocity $v_r^i = 1$ in tether parallel to the tether

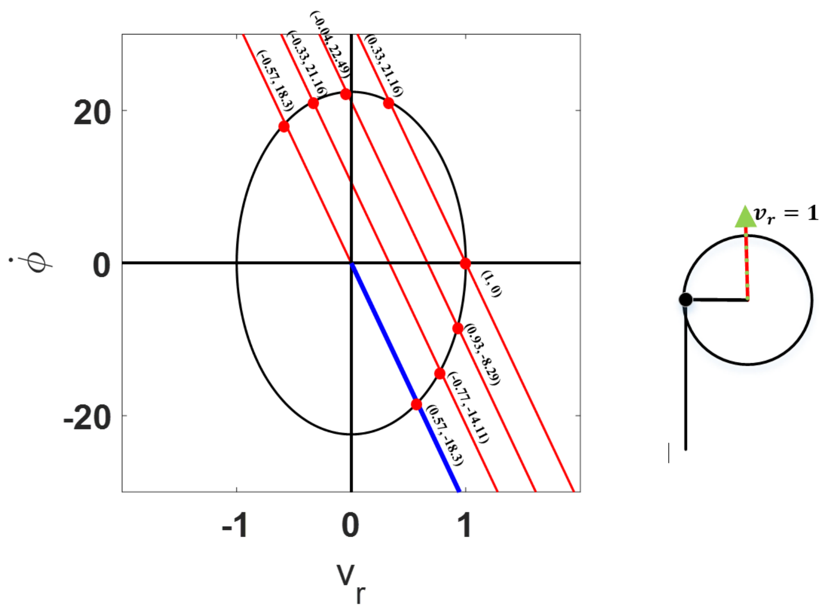

Figure 5.9: Shows the energy ellipse for the puck. The blue line indicates the impact line of action for the tether and offset angles illustrated above. The two intersections of the ellipse with each red line parallel to the blue line indicates the velocities before impact and velocities after impact.

direction while the offset angle is perpendicular to the tether, then the output velocities after the impact are $v_r^i = 0.33$ and $\dot{\varphi}_r^i = 21.16$. Other input velocities also result in corresponding output velocities as it is shown in Fig. 5.9. For instance, by looking at the ellipse, immediately one can observe how the energy is changing from transnational to rotational mode and vice versa without any further need for calculating the equations.

Furthermore, the bouncing direction of the object after the impact can be obtained from following expression

$$\alpha^f = \arctan \frac{v_r^f}{v_\theta^f} \tag{5.14}$$

where $v_{\theta_f} = v_{\theta_i}$ indicating that the velocity in $\theta - direction$ remains unchanged after the impact and α^f is the direction of the puck with respect to the tether line of action after the impact.

5.6.2 Dissipation of Energy

In the previous section, we demonstrated the effect of the geometry and attachment point in the achievable puck velocities. We also showed how to use the energy ellipses to predict the energy transformation after the impact. The question of impact controllability then comes down to determining the transformation of the energy after the bounce while the dissipation of energy also exists. This section considers the condition where the tether attached to the object is not ideal which means some part of energy may dissipate during impact. The dissipation of energy can occur in direction of impact line of action according to the *Newton's kinematic hypothesis* [63]. Regarding the Newton's kinematic hypothesis, the coefficient of restitution can be written as a combination of the velocities before and after the impact.

$$e = \frac{v_r^f}{v_r^i} \tag{5.15}$$

Now a question arises how to use this model in our visualization model? and how the dissipation of energy affect on energy level ellipse? The first attempt was done by multiplying the (5.15) in left side of energy equation (5.8) which results in the wrong solution. The coefficient of restitution is defined in the direction of impact line of action. Since the energy equation has the rotational term, we cannot directly implement the coefficient of restitution into the equation. Therefore, the implementation has to taken into account in a new coordinate frame where the the rotational velocities remain unchanged through the impact.

In order to do so a Jacobian needs to be found that maps the translational and rotational velocities to the new coordinate $(\dot{q}_1, \dot{q}_2)$ where $\dot{q}_1$ is in the direction of impact line of action and $\dot{q}_2$ is orthogonal to $\dot{q}_1$ such that $\Delta\dot{q}_2 = \dot{q}_2{}^f - \dot{q}_2{}^i = 0$. This relationship is given by

$$\begin{bmatrix} \Delta v_r \\ \Delta \dot{\varphi} \end{bmatrix} = \hat{J} \begin{bmatrix} \Delta \dot{q}_1 \\ \Delta \dot{q}_2 \end{bmatrix}, \tag{5.16}$$

where $\Delta \dot{q}_1$ and $\Delta \dot{q}_2$ are the change of translational and rotational velocities before and after the impact respectively. $\hat{J}$ is the Jacobian that maps current coordinate to new coordinate where one axis is along the impact line of action ($\Delta \dot{q}_1$) and $\Delta \dot{q}_2$ is orthogonal to the $\Delta \dot{q}_1$. That means for any line parallel to $\dot{q}_1$ axis, the values in $\dot{q}_2$ axis remains unchanged during the impact. To find the Jacobian, we take the following steps:

From (5.16), we have the following relationships

$$\Delta v_r = \hat{J}_{11} \Delta \dot{q}_1 + \hat{J}_{12} \Delta \dot{q}_2 \tag{5.17}$$

$$\Delta \dot{\varphi} = \hat{J}_{21} \Delta \dot{q}_1 + \hat{J}_{22} \Delta \dot{q}_2 \tag{5.18}$$

Since in new coordinate the rotational velocity doesn't change, $\Delta \dot{q}_2 = 0$. Therefore, from (5.13), and (5.17) we have

$$\frac{\hat{J}_{21}}{\hat{J}_{11}} = \frac{mR \sin \alpha}{I} \tag{5.19}$$

Using this ratio if we assume $\hat{J}_{11} = 1$ then we have

$$\hat{J}_{21} = \frac{mR\sin\alpha}{I} \tag{5.20}$$

From orthogonality law, we can write

$$\begin{bmatrix} \Delta\dot{q}_1 & 0 \end{bmatrix} \begin{bmatrix} \hat{J}_{11} & \hat{J}_{21} \\ \hat{J}_{12} & \hat{J}_{22} \end{bmatrix} \begin{bmatrix} m & 0 \\ 0 & I \end{bmatrix} \begin{bmatrix} \hat{J}_{11} & \hat{J}_{12} \\ \hat{J}_{21} & \hat{J}_{22} \end{bmatrix} \begin{bmatrix} 0 & \Delta\dot{q}_2 \end{bmatrix} = 0 \tag{5.21}$$

where after simplifying it takes the following form

$$\hat{J}_{11}m\hat{J}_{12} + \hat{J}_{21}I\hat{J}_{22} = 0 \tag{5.22}$$

substituting $\hat{J}_{11}$ and $\hat{J}_{21}$ results in

$$\frac{\hat{J}_{12}}{\hat{J}_{22}} = -R\sin\alpha \tag{5.23}$$

Once again using this ratio we can assume $\hat{J}_{22} = 1$ then

$$\hat{J}_{12} = -R\sin\alpha \tag{5.24}$$

which leads to

$$\hat{J} = \begin{bmatrix} 1 & -R\sin\alpha \\ \frac{mR\sin\alpha}{I} & 1 \end{bmatrix} \tag{5.25}$$

Once the Jacobian is obtained, the coefficient of restitution e can be implemented into the energy equation. First, both translational and rotational velocities are calculated in the new coordinate. Then the coefficient of restitution is multiplied by initial velocity before the impact according to the equation below and the result will be transformed back to the old coordinate.

$$\begin{bmatrix} v_r^i \\ \dot{\varphi}^i \end{bmatrix} = \hat{J} \begin{bmatrix} e\dot{q_1}^i \\ \dot{q_2}^i \end{bmatrix}, \tag{5.26}$$

To use the energy ellipse and impact line action for the case with energy loss, we normalize the new coordinate using the *Tissots indicatrix* and plot the energy ellipse and impact line of action with respect to the new coordinate. The Tissots indicatrix is a transformation matrix that illustrates the extent of a maps distortions by showing how the circles transform to the ellipses in parameter space [16]. This transformation is normally used to show the distortion as a field of ellipses over a space. To normalized the coordinates, we obtain this transformation and then multiply the inertia matrix by the inverse of the Tissots transformation matrix to turn the energy ellipse to the circle.

The indicatrix ellipses are derived from the singular value decomposition of the inertia matrix

$$SVD(\mathcal{M}) = U\Sigma U^T \tag{5.27}$$

where the inertia mass matrix in new coordinate is

$$\mathcal{M} = \begin{bmatrix} \hat{J}_{11} & \hat{J}_{21} \\ \hat{J}_{12} & \hat{J}_{22} \end{bmatrix} \begin{bmatrix} m & 0 \\ 0 & I \end{bmatrix} \begin{bmatrix} \hat{J}_{11} & \hat{J}_{12} \\ \hat{J}_{21} & \hat{J}_{22} \end{bmatrix} \tag{5.28}$$

The Σ is a scaling matrix, and U can be viewed as rotation matrix. Now we can define a Tissot transformation matrix T as following form

$$T = U\Sigma^{-\frac{1}{2}}U^T \tag{5.29}$$

that encodes the local deformation produced by the projection. Applying inverse of Tissot transformation to the new coordinates and the energy ellipses shown in Fig. 5.11 results in Fig. 5.10.

As illustrated in Fig. 5.10, the ellipses are circles and the impact line of action only changes horizontally which means the energy only changes the translational velocity inline with impact line of action. Furthermore, it is illustrated that the coefficient of restitution has a direct relationship with the ratio of the velocity after

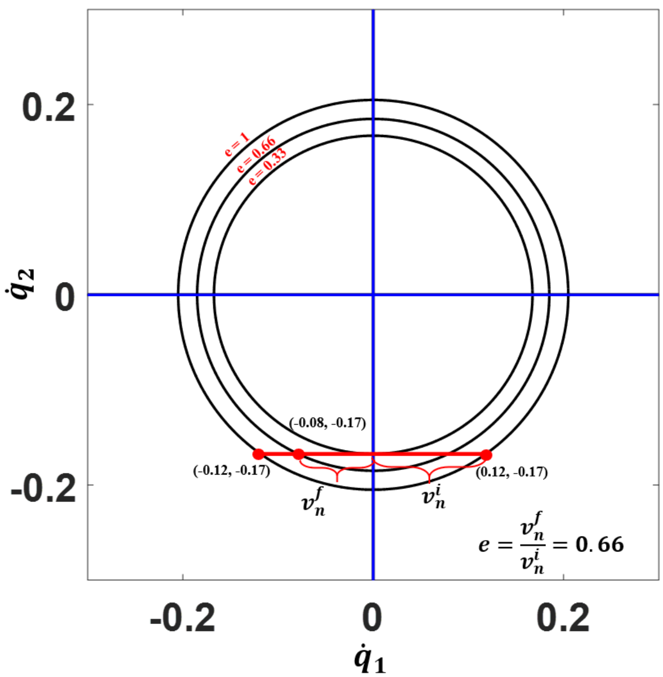

Figure 5.10: In the normalized coordinate the ellipses have transformed to the circle and changing of the momentum occurs in horizontal direction which indicated the angular momentum remains unchanged. The energy loss now is directly related to the translational velocities as demonstrated in the figure.

the impact over the velocity before the impact.

Now, the energy ellipses can be plotted as illustrated in Fig. 5.11 illustrates how the ellipses due to energy loss look like in original coordinate. Each ellipse corresponds to a value of the coefficient of restitution. As shown in Fig. 5.11, the intersection of the impact line of action with the corresponding ellipses, determines the translational and rotational velocities after the impact. For instance, once again if the puck moves with translational velocity $v_r^i = 1$ in tether parallel to the tether direction while the offset angle is perpendicular to the tether, then the

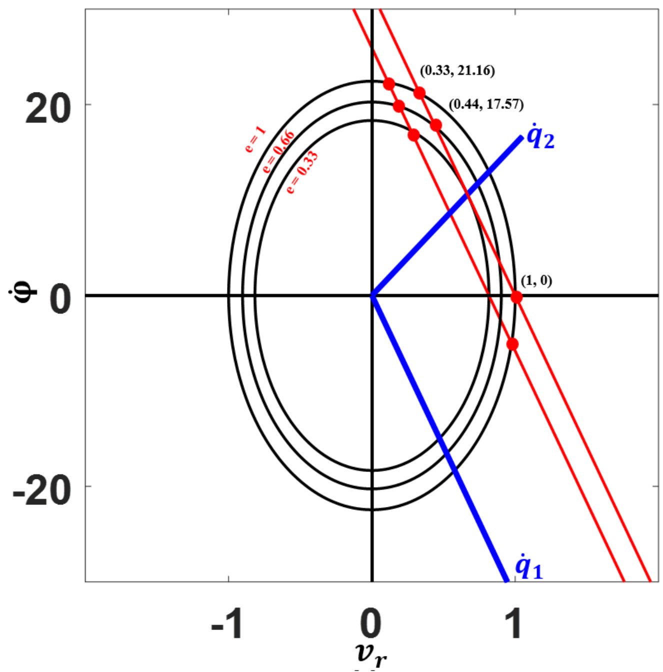

Figure 5.11: The energy ellipses are depicted for three different values of coefficient of restitution. The blue coordinate is the new coordinate where if the coefficient of restitution is implemented, the energy loss only occur in translational direction. The intersections of the ellipses with red lines, show how the energy changes after the impact for different coefficient of restitution.

output velocities after the impact are $v_r^i = 0.33$ and $\dot{\varphi}_r^i = 21.16$ for completely elastic impact whereas for the case of energy loss in system ($e = 0.66$), the output velocities after the impact are $v_r^i = 0.44$ and $\dot{\varphi}_r^i = 17.57$. Therefore, for any given input velocities the corresponding output velocities can be observed as it is shown in Fig. 5.11.

As one can see in the Fig. 5.11, the intersection of impact line action and ellipses occur in two points. As explained earlier, in new coordinate the rotational velocities remain unchanged through the impact therefore, the impact happens

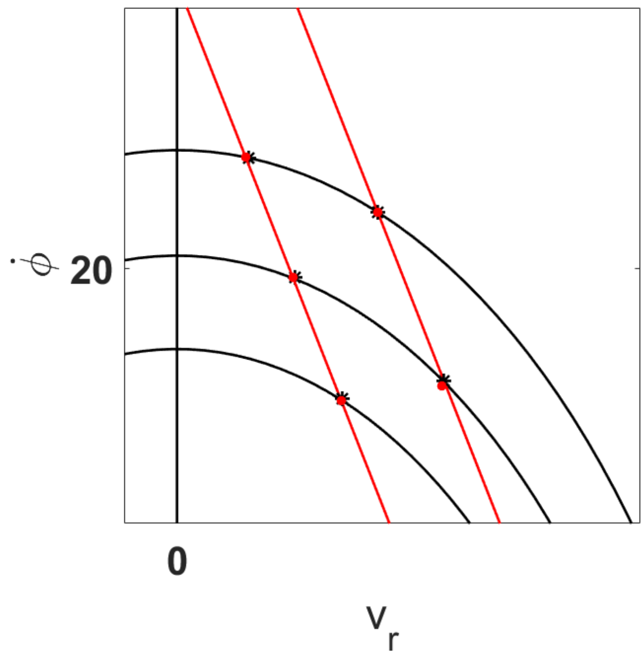

Figure 5.12: The comparison is made between the simulation and analytical solutions which shows that the energy ellipses results are accurate.

as if it is a central impact. In central impact the direction of the velocities will change after the impact, hence, in case of energy ellipse one can see which point has opposite direction in $\dot{q}_1$ direction.

To verify the results from energy ellipses, an equivalent mass-spring-damper model related to the coefficient of restitution is needed. According to [82] the non-dimensional damping ratio can be written as a function of coefficient of restitution.

$$\zeta = -\frac{\ln e}{\sqrt{\pi^2 + (\ln e)^2}} \tag{5.30}$$

hence, the damping coefficient is obtained from

$$c = \zeta\sqrt{km} \tag{5.31}$$

where the k is spring stiffness and m is the effective mass of the puck. This equation provides a good approximate relation between damping ratio and coefficient of restitution. The results are illustrated in Fig. 5.12 which verify the results obtained from the energy ellipses method.

5.7 Error Caused by an Non-ideal Tether

In all above impact study, the tether was assumed an ideal tether such that once the impact occurs the impact point remains steady and no changes happen in the position of the end-effector. In this section, we consider a case where the string is not ideal and the position where impact starts is different from the one after the impact. This error results from the stretch and rotation of the tether during the impact. This can be thought as a spring substitute with the string which only acts as it stretches. Therefore, when spring becomes taut, it will continue to stretch to some extent and while it is stretching the velocity in $\theta - direction$ cause the spring to rotate as shown in Fig. 5.13 which leads to the different velocity direction after the impact. As shown in Fig. 5.13, the error composed of translation, rotation, -rotation and -translation of the puck. Therefore, the error of the end-effector can

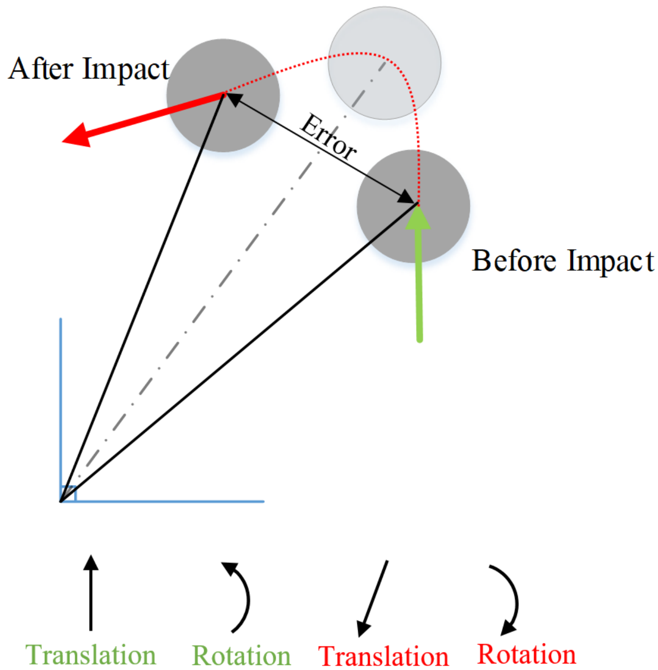

Figure 5.13: The error that an non-ideal tether caused in direction of the movement after impact. The sequences of movement is shown with arrow as illustrated.

be captured approximately by using the Lie bracket rules.

We define two vectors in local coordinate(r, θ as

$$v_r = \begin{bmatrix} 1 \\ 0 \end{bmatrix}, \quad v_\theta = \begin{bmatrix} 0 \\ 1 \end{bmatrix} \tag{5.32}$$

These vectors can be written in world coordinate

$$v_1 = g \begin{bmatrix} 1 \\ 0 \end{bmatrix}, \quad v_2 = g \begin{bmatrix} 0 \\ 1 \end{bmatrix} \tag{5.33}$$

where g is a mapping from local coordinate to world coordinate and it takes the following form

$$g = \begin{bmatrix} \cos\theta & -\sin\theta \\ \sin\theta & \cos\theta \end{bmatrix} \tag{5.34}$$

The Lie bracket of two vectors $v_1, v_2 \in \mathbb{R}^2$ finds the net effect of making sequential, infinitesimal moves in the $v_1, v_2, -v_1, -v_2$ directions and is calculated as

$$[v_1, v_2] = \nabla v_2.v_1 - \nabla v_1.v_2 \tag{5.35}$$

which results in

$$[v_1, v_2] = \begin{bmatrix} -v_r v_\theta \frac{y}{x^2+y^2} \\ v_r v_\theta \frac{x}{x^2+y^2} \end{bmatrix} \tag{5.36}$$

where x and y indicates the position of the center of the puck with respect to the world frame. The x and y components of the Lie bracket capture the net motion of the puck.

To verify the error found from Lie bracket equation, the simulation using full of equation of motion is carried out. To do so, we use the spring to simulate the behavior of an non-ideal string. The error calculated based on the duration of the spring stretch. Once the spring reaches to its free length, the simulation is stopped and the position and the time are recorded. The time obtained from simulation is used to calculate the final position of the puck according to the velocities computed from Lie bracket. The comparison has been done for different tether angle with respect to the initial velocities as well as duration of impact as shown in Fig. 5.14.

The results reveal that the Lie bracket has a good approximation in calculating the error for small deviation of the tether angle. Furthermore, it is shown that as the impact duration increases, the Lie bracket approximation loses its accuracy.

5.8 Experiments

In conjunction with our analytical and numerical investigation of tethered-projectile redirection, we also carried out a series of experimental tests on this process. We attached a lightweight tether to a puck on an air hockey table, then used a pendulum-hammer to apply a repeatable initial velocity to the puck. We then tracked the puck's subsequent motion via a high-speed camera (GoPro, HERO3+, 1080p) at 60 frames per second (fps) and extracted its trajectory by processing the video data. Results from two series of these experiments are presented in Figs. 5.15

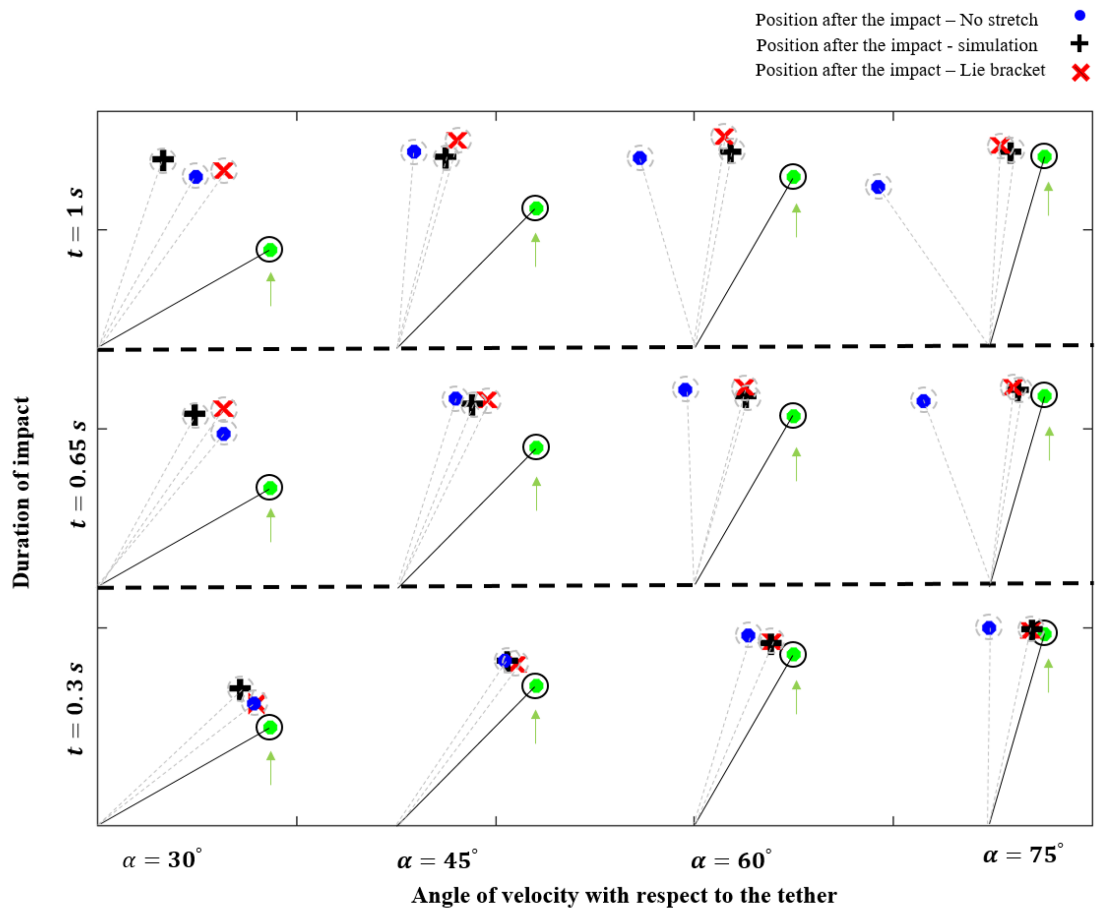

Figure 5.14: The comparison is made using the full equation of motion for different configurations. The results demonstrates the good convergence for small tether angle with respect to the velocity as well as small duration of impact.

and 5.16.

Our first experiment was to test the bounce direction of a puck with a tether attached to the center of mass for different tether angles. The impulse model predicts that there should be a 2:1 linear relationship between the tether angle and the puck deflection, based on the requirement of equal incident and reflection angles. As shown in Fig. 5.15, the measured bounce direction closely matched this prediction. The small negative error in the data is most likely a result of energy dissipation in the tether, which would reduce the rebound component of the final velocity and thus the deflection angle.

In our second experiment, we observed the motion of the puck when the tether was placed at a nominal angle of 45° to the puck's velocity and the tether was attached outboard to the center of mass and at different angles. The data from this experiment is plotted in Figs. 5.16, and once again shows a good correlation to the experiments. We attribute the error in this plot to a combination of energy dissipation in the tether and a small rotational disturbance in the initial conditions set by the pendulum hammer and from drag on the slack tether. We correct for the net rotation from these sources by plotting the puck's deflection relative to the actual measured initial angle, but the spin also adds energy to the system that is more difficult to accurately capture and compensate for.

Finally, in the third experiment, we tested the deadspin effect. A challenge in observing this effect is that unless the string is released from the base after the impulse is finished, the puck will bounce a second time after making a half-revolution. To avoid this second bounce, we constructed a dynamically-equivalent

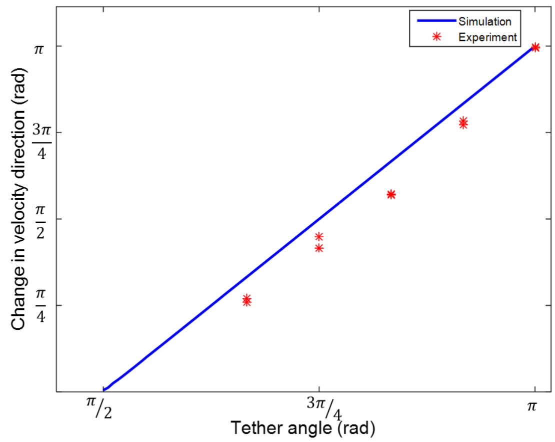

Figure 5.15: Comparison of simulation and experiment in which the tether is attached at the center of mass and its angle is varied with respect to initial velocity direction.

system, illustrated in Figs. 5.17 in which the tether is replaced by an orthogonal wall. The wall is raised slightly to allow the puck to slide beneath it, but to catch against a pin at the puck's "tether attachment point" and provide an equivalent impulse. As can be seen from the captured images and the attached video, the puck indeed goes into the deadspin predicted by the model and makes more than a full revolution without leaving the red area at the center of the air table.

5.9 Discussion

In this chapter, we investigated the direction in which a moving projectile anchored by a tether will bounce when the tether becomes taut. In doing so, we identified five critical points in the puck's dynamics:

1. The puck is *maximally deflected* when the tether's line of action passes

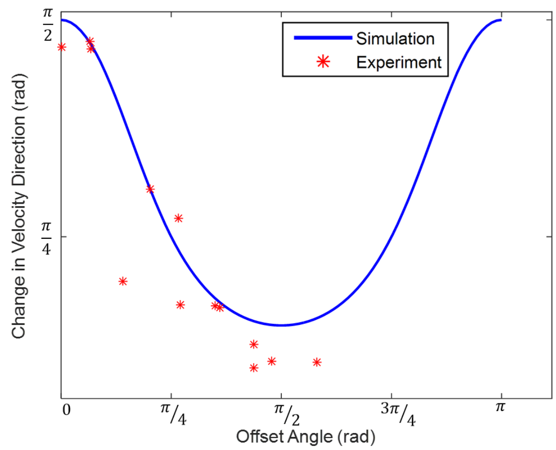

Figure 5.16: Comparison of simulation and experiment in which the tether angle is set at a 45° angle relative to the puck's initial velocity, and the offset angle α is varied.

through the center of mass, and so transfers no energy into the rotational mode.

2. The puck is *minimally deflected* when the tether's line of action is at right angles to the line connecting its attachment point to the center of mass. In this configuration, the impulse's moment-to-force ratio is large, and the puck rotates into the tether (causing it to go slack) before it can fully redirect its linear momentum.

3. The puck is *maximally decelerated* when the tether's line of action is tangent to the puck's radius of gyration, and so optimally transfers energy into the rotational mode and out of the translational modes.

4. The puck's bounce is predicted using the energy ellipse and impact line of action even when puck has *non-zero rotational velocity.*

5. The puck's bounce is predicted considering the effect of *energy dissipation*

on the tether using the family of the energy ellipses intersecting with tether line of action.

In our future work, we aim to build on these results by incorporating the bounce dynamics into a system that can actively change its orientation during flight, e.g., by coupling to a flywheel or other reaction mass. We anticipate that the combination of the bounce and orientation dynamics will lead to the development of mobile systems with novel maneuvering capabilities. We will also be incorporating our bounce analyses into our ongoing work on casting manipulation [83] (interacting with the environment via an end-weighted tether) and spring-mass legged locomotion [84].

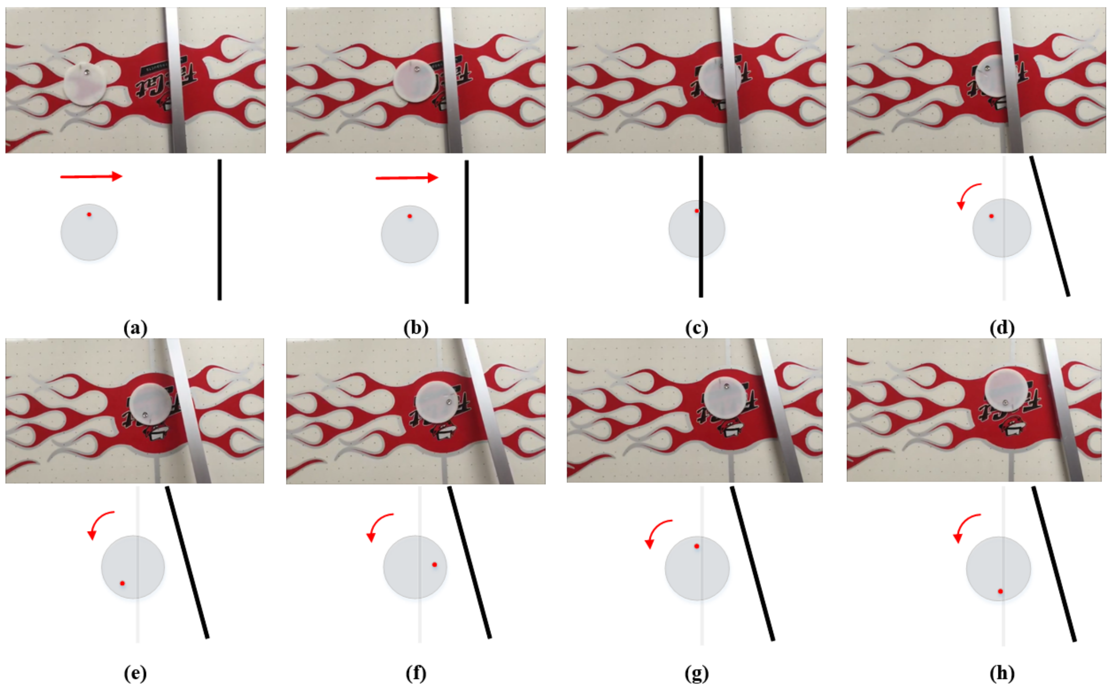

Figure 5.17: Experimental validation of the deadspin effect described in §4.2. The puck can slide under the bar, but has a pin that can catch on the bar, and so is dynamically-equivalent to the tethered puck. With an initial velocity perpendicular to the wall and the pin at the puck's radius of gyration, the puck goes into a deadspin on impact and stops at the same place. We remove the bar after the initial impact—between (c) and (d)—to prevent the puck from experiencing a second bounce between (e) and (f). Note that the camera was angled in the experiment, but the bar is shown correctly in the cartoon as being perpendicular to the velocity direction.

Chapter 6: Geometric Motion Planning for Systems with Fast Energy Release

6.1 Introduction

Jumping can serve multiple functions for animals and robots: Escape from a predator or other dangerous situation, efficient locomotion over rough terrain [2], and launching at a target. Achieving these goals requires a combination of fast energy release and a structure to channel this release in a desired direction. This aiming is especially important for purposeful locomotion and targeted launching.

Jumping spiders provide an interesting example of an aiming mechanism that is employed by animal feeding strategy involves precision pounces on often-airborne insects. The spiders use their legs to adjust the direction and velocity of the jump. The rear legs provide the required reaction force to propel the spider and the front legs in jumping spider act as a lever to control the direction of the jump [2].

In this chapter, we present a simplified model of the jumping spider robot based on the anatomy of the real spider. The main contribution of this chapter is to investigate the geometry of the jump and how the presence of the vaulting leg affects the resulting motion; this focus on how energy is *channeled* is in contrast to most other jumping studies' focus on questions of energy storage capacity and rate of release. In our model we implement the main legs of the spider which

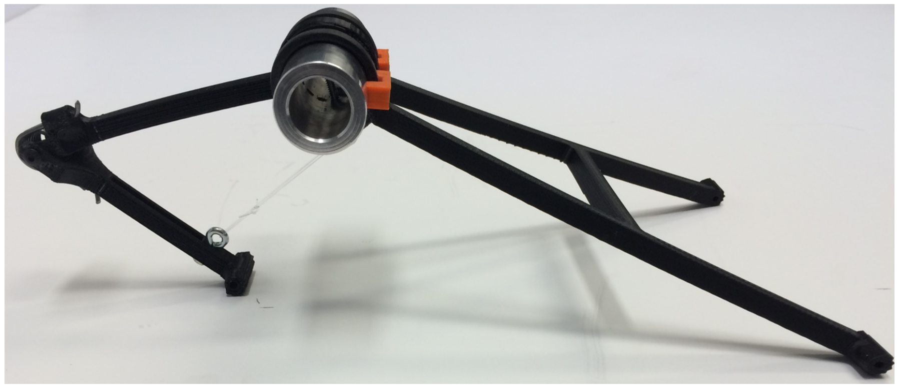

Figure 6.1: The jumping spider mechanism.

can contribute in the targeted jump as identified in [2]: the hind leg that supplies the energy for the jump, and the front leg which acts as a guide for the energy release. We use dynamic simulations to investigate the influence of parameters including front leg angle, front leg length and spring stiffness on the height, travel distance, velocity and direction of the jump. These simulations were corroborated via experiments on a physical implementation of our model, illustrated in Fig. 6.1 and the accompanying video.

A key insight that we gained from this investigation is that the vaulting leg allows the system to jump along flatter trajectories than would be possible with a simpler aiming mechanism. This effect persists even as the spring stiffness is increased, indicating that this increased range of launch angles is a fundamental geometric effect, and not tied to a slow release of jumping energy.

6.2 Literature Review

This chapter draws on prior research efforts regarding jumping spider anatomy and jumping mechanism. Researchers have worked on many robots with jumping ability [85, 86, 87, 88, 89, 90] for which the main concerns are overcoming high obstacles, designing good energy storage mechanisms, and efficiently releasing the energy [91]. In [92], a 7g jumping mechanism was developed to overcome large obstacles. The major focus of that study is on the height and the travel distance of the jumping robot. In order to generate a high jump, Kovac, et.al designed the mechanism such that the force profile starts with small force to prevent the system from launching before the maximum energy has been released from the spring into the system. The 7g jumping mechanism was later improved by adding the ability to steer the take-off in the horizontal plane [93].

Some investigations of jumping designs that have taken advantage of an assistive leg to jump [94, 95]. The assistive leg can help the robot to steer itself and jump with a desired elevation. In recent study of jumping robots, the [95] presented a soft robot which takes advantage of combination of pneumatic and explosive actuators to perform a jump. The robot proposed in study is capable of targeted jump, with the height and travel distance adjustable by its legs. In these works, however, the legs have been treated primarily as an aiming device for the energy release mechanism, and their effects on the launch dynamics have not been considered.

The jumping process also has been studied from biological point of view. Jumping spider characteristics in different jump situations have been considered in [2]. In this research, photographs were used to measure the spider jumps. The focus was mainly on the ability of spiders to select their take-off velocity and direction to account for prey position and gravity. Other related works have studied on hydraulic leg extension. Parry and Brown [96] concentrated on jump mechanism of jumping spiders and mentioned that there are no extensor muscles at the hinge joints of spider leg and the extension is due to haemocoelic blood pressure [97]. The directional jump also has been studied for other insects. Card studied the fruit flies behavior of the jump [98] and showed why they are so hard to swat. She demonstrated that the flies can change the center of mass (COM) of their body by combination of leg placement (changing legs position) and leaning (shifting the body position). This center of mass movement helps them to jump in different directions. Her study revealed that most of the COM repositioning in forward and backward direction comes from leg placement whereas, the leaning movement mostly contributes in lateral repositioning. In the other study, Burrows investigated the grasshopper jump and the role of its legs during the jump [99]. He identified three different phases where the jump takes place and in the second phase the body angle is adjusted by changing the front leg position.

6.3 Spider Anatomy and Modeling

There are two main legs that play key roles in launching the jumping spider. The rear leg (labeled IV in [2] and in Fig. 6.2) provides most of the propulsion force for

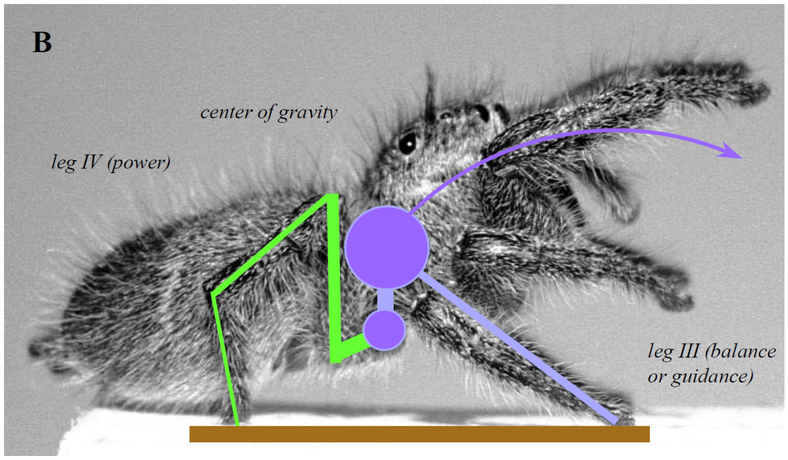

Figure 6.2: Description of fundamental legs of jumping spider for a complete jump [2].

a jump. The front leg (labeled III) contributes a stabilizing force to stop the spider from falling over before the jump and serves to guide the direction of jumping [2]. The rear leg has several links, which straighten from initial folded position under internal pressure [97].

Based on the information gained from the anatomy of the spiders, we model our jumping spider as a planer system consisting of rear and front legs in which both front leg and rear leg have no-slip contact with the ground, and thus serve as pivots while there is a positive reaction force. The, rear leg in our model is composed of two segments which are equal in length and are joined together. The front leg length is equal to the length of summation of rear legs. We model the legs as massless links, corresponding to the concentration of mass in the body of a real spider [97].

The resulting system is a four-bar linkage. We model the body as a point mass, the front leg as freely pivoting around the body, and the leg energy storage as rotational spring at the joint that provides leg extension as shown in Fig. 6.3.

The spiders jump occurs in four phases. Fig. 6.4 shows three stages of jumping and one stage of flying. In each stage, the trajectory of the body mass is displayed as the trailing path.

- Stage (1) is when spring is released from an initial resting configuration.
- Stage (2) shows the spider as it has begun to increase in its velocity in an upward direction, pivoting around the front foot. This stage only appears during vaulting jumps.
- Stage (3) shows when the reaction force of the front leg becomes zero, the system enters into the unsupported phase. In an aiming jump, the system enters this stage directly from stage 1.
- Stage (4) shows the spider at flying phase. When both legs have zero reaction force, the system enters its flight phase.

The jumping spider jumps by starting in a configuration with the back leg spring pre-loaded to jump. When it is released, it continues until the rear leg angle α_2 becomes close to 0°angle (stage 3) and after that it enters to the stage (4) with the initial velocities taken from the previous stage.

Note that the Fig. 6.4 shows a vaulting jump. In some cases (the *unsupported jumps* described below), the mechanism lifts off directly, without pivoting around the front leg.

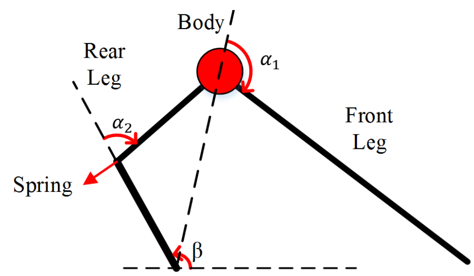

Figure 6.3: The spider model.

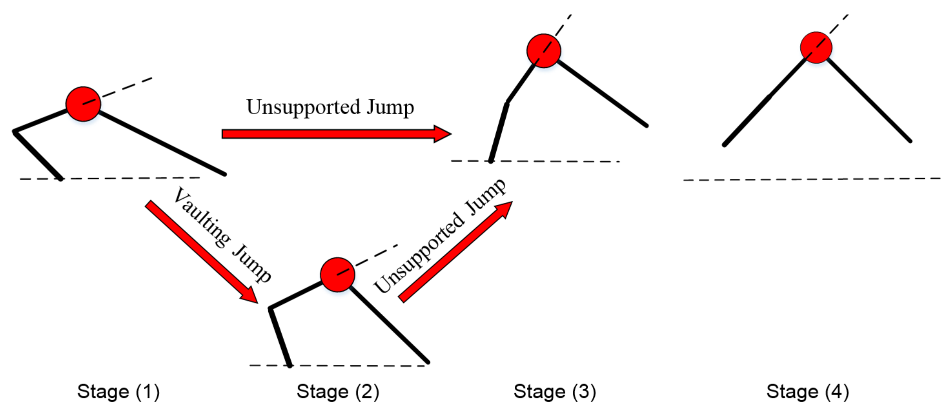

Figure 6.4: Stages of the jump. (1) initial configuration, (2) pivoting around front foot, (3) launching off of rear leg, and (4) flight phase.

6.4 Types of Jump

There are three different jumps may happen for spiders: unsupported Jump, aiming and vaulting.

- **Unsupported Jump:** The initial reaction force is what determines an unsupported jump, and that in the limit of high stiffness, it would be an aiming jump, but that for lower stiffnesses, the jumper would "fall over" as it launches.

- **Aiming jump:** Is the theoretical limit of unsupported jump when the jump occurs very fast. Therefore, the system launches along the initial body angle.
- **Vaulting:** In a vaulting jump, the mechanism pivots around the front foot, re-aligning the rear leg's line of action prior to take-off.

Given this categorization of jumping, we can then ask:

- What is the role of the mechanism's geometry in the jump?
- Under what conditions does an unsupported jump occur?
- Under what conditions does vaulting occur?
- How does vaulting affect the kinds of jumps that the mechanism can make?

6.5 Simulation and Results

To investigate the system's jumping behavior, we carried out a series of simulations. The fixed parameters over these simulations are the lengths of the leg segments, $L_1 = L_2 = \frac{L_3}{2}$ and initial angle of the back leg joint (i.e., the compression of the spring) at $\alpha_2 = 2.2$ radians. In our parameter explorations, we evaluate the effect of initial front leg angle α_1, non-dimensional stiffness

$$\rho = \frac{{\omega_n}^2}{\ddot{\theta}} = \frac{k}{m} \cdot \frac{L_1 + L_2}{g} \tag{6.1}$$

relating the time scale of spring release and falling forward, and front leg length. In each series of simulations, we fixed one of the variables, took a coarse sampling of a second, and a fine sampling of a third, resulting in three plots of data each, as illustrated in Fig. 6.5, 6.6, 6.7 and described below.

6.5.1 Front Leg Angle (α_1) and Stiffness (ρ)

The first set of simulations consider the effect of the front leg angle on the launch angle, at low, medium and high stiffness. As illustrated in Fig. 6.5, increasing the front leg angle increases the launch angle. For low stiffness, the hypothetical unsupported jump is very close to the vaulting jump. As the spring stiffness becomes higher the take-off angle for the unsupported jump approaches that of the aiming jump, while the vaulting jump maintains a significantly lower angle. When the front leg increases, the spider's body tends toward the back leg and causes the reaction force to get close to the vertical direction which decreases the load over the front leg and instead put more load on the back leg. Therefore, the spider experiences unsupported jump.

6.5.2 Spring Stiffness (ρ) and Front Leg Angle (α_1)

The second set of simulations considers the effect of the stiffness on the launch angle, at small, medium and large front leg angle. As shown in Fig. 6.6, increasing the stiffness increases the flying angle to some extent and this is noticeable that the rate of increase in flying angle is much higher when spider is doing aiming jump than when it is doing vaulting jump (Fig. 6.6 *c*). Similar to the results

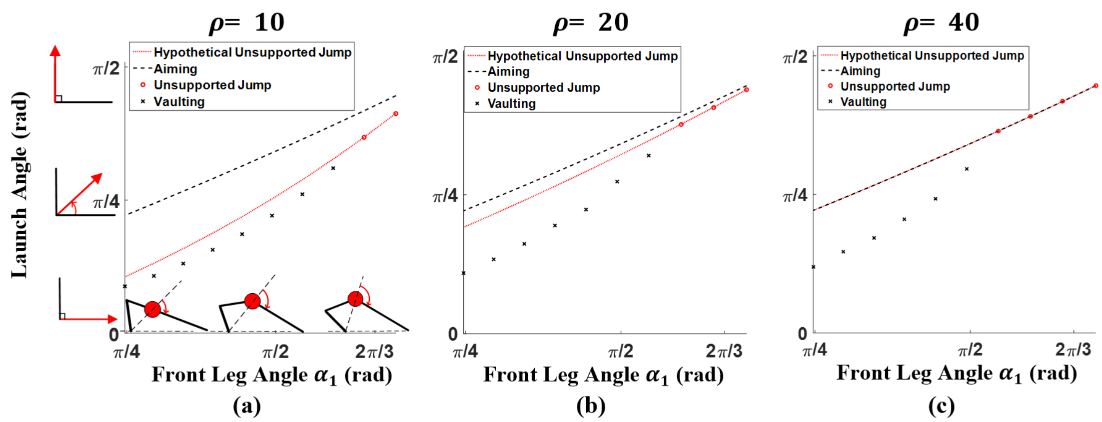

Figure 6.5: Launch angle and type as a function of stiffness and front-leg angle. As the stiffness increases, unsupported jump converges to the aiming jump and vaulting stays as lower launch angle.

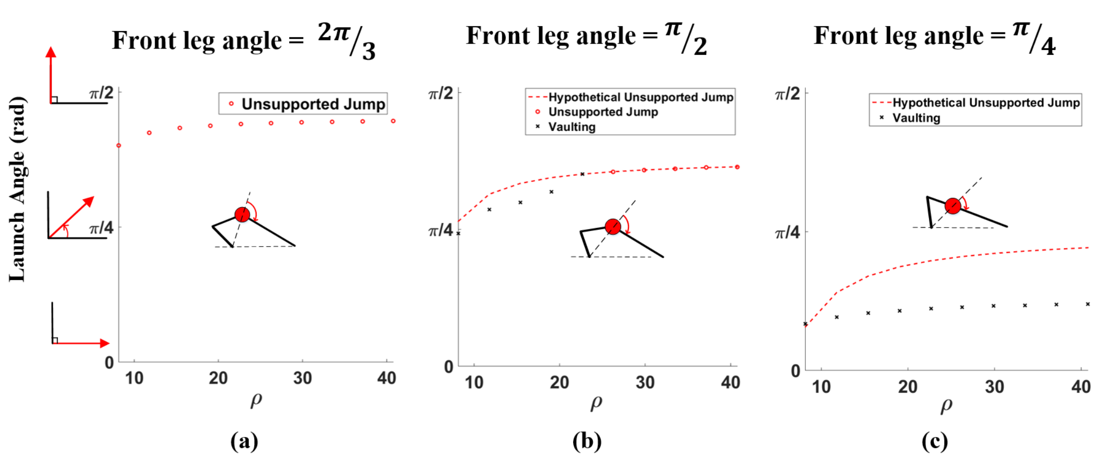

Figure 6.6: Launch angle and type as a function of front leg angle and spring stiffness. Lower stiffness corresponds to the vaulting behavior and the front leg angle decrease results in vaulting behavior over a greater range of stiffnesses.

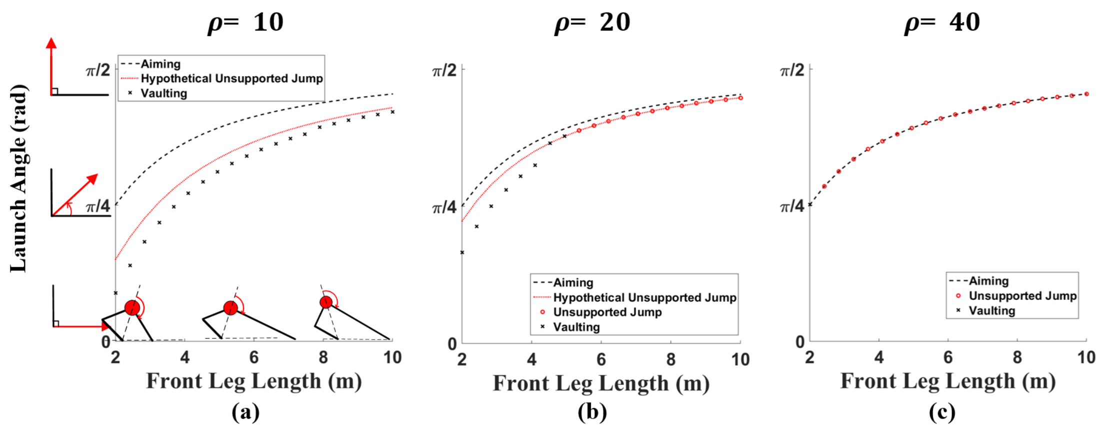

Figure 6.7: The behavior of the jump for $\alpha_1 = 30°$and front leg length variation are depicted. Increasing the front leg length increases the launch angle and can change the type of jump (b).

from the front leg angle, it is shown here that for any given stiffness, in some angle the spider only performs unsupported jump and in some others does the vaulting angle. The figure states that for small front leg angle, the difference of flying angle between hypothetical unsupported jump and vaulting jump is more. That is because vaulting takes longer time before switch to unsupported jump. (Vaulting jump usually starts with vault and then during the jump when spider loses the front leg contact, switches to the unsupported jump). As expected also, increasing the stiffness has a direct effect on the travel distance and the height of the jump regardless of what the front leg angle is, and increases both height and travel distance. Also, as the stiffness increases the speed of the jump increases.

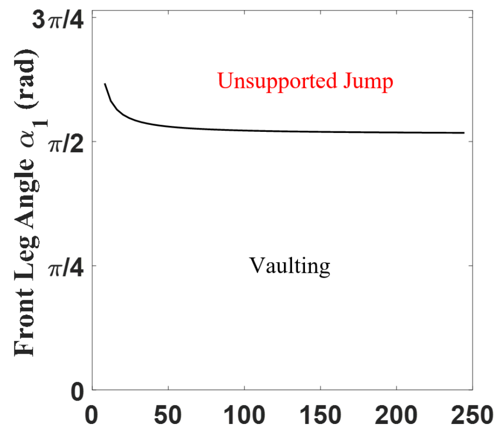

Figure 6.8: Separated regions where the vaulting jump or unsupported jump occurs.

6.5.3 Front Leg Length (L_3) and Spring Stiffness (ρ)

Finally the third set of simulations considers the effect of the front leg length on the launch angle, at low, medium and high stiffness. Increasing the front leg length, increases the flying angle regardless of the type of the jump (Fig. 6.7). For larger front leg angle, higher spring stiffness and larger front leg, the spider does unsupported jump. On the other hand, for smaller front leg angle, lower spring stiffness and smaller front leg, the spider does the vaulting jump. As the leg length increases for the same configuration, the body of spider moves toward the back leg. Therefore, the reaction force on the rear leg tends to the vertical direction which causes the front leg loses its contact with ground at the beginning of the jump and performs unsupported jump.

6.5.4 Analysis of Results

The vaulting and aiming motions are distinguished by the presence or absence of a vertical reaction force on the front foot when the spring is released. We calculate this reaction force by assuming a zero-displacement constraint on the motion of the front foot, and then extracting the vertical reaction force from the resulting trajectory of the body as

$$F_R = \frac{m(\ddot{y}x + g) - m\ddot{x}y}{L} \tag{6.2}$$

where x, y, $\ddot{x}$, $\ddot{y}$ are the position and acceleration of the body respectively. L is the toe's distance of the front and back legs. If $F_R > 0$, then the zero-displacement condition is consistent with the spider vaulting with some weight supported on the front foot. If $F_R \leq 0$, then this means that the spring has sufficient vertical force to immediately lift the spider in an aiming jump.

The Fig. 6.8 illustrates that even for high stiffness spring (explosive-actuated system) the system vaults at some angles, and that the division converges to the angle of α_1 at the initial configuration as ρ increases, where γ is the angle of the reaction force and $(x,\ y)$ is the position of the center of mass. if $\alpha_1 > 90°$, an unsupported aiming jump occurs. On the other hand, if $\alpha_1 \leq 90°$ the system vaults instead (Fig. 6.9).

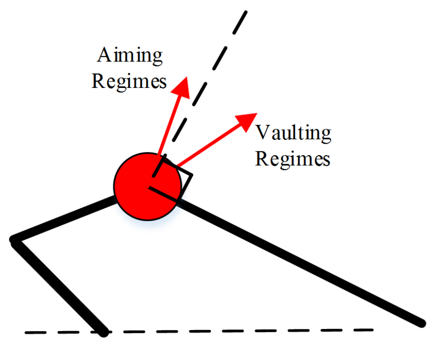

Figure 6.9: Description of aiming and vaulting jump

6.6 Experiments

To demonstrate the aiming and vaulting motions on a physical system, we built a proof-of-concept mechanical model, illustrated in Fig. 6.1. This model consists of four main parts: The front and rear legs, main body, and the leg stoppers. The front and rear legs are of equal length (165mm) and 3D printed with ABS plastic. The main columns of the legs feature a c-channel design in order to save weight and provide the appropriate strength. All three ground contact points for the legs have small extruded spikes to ensure there is no slipping during the jumping motion. The front legs are fixed together with a cross brace to ensure even tracking and increase rigidity. The rear leg features a joint at the midpoint which is fitted with a torsional spring to actuate the jumping motion.

The spring is loaded manually, then secured with fishing line using the 2 eye-bolts located at opposite ends of the rear leg. The string is then cut to release the energy stored in the spring to actuate the jumping motion. The main body of the mechanism was constructed using a single hallow tube of aluminum. The use of aluminum against plastic creates a low friction interface allowing the front legs to rotate, as well as providing enough weight to keep the center of mass close to concentric with main body. The lateral center of the main body features 12 tapped holes that are drilled at 30°degree increments around its circumference. These holes allow for the angle between the front and rear legs to be adjusted by removing the eyebolt at the top of the rear leg, and rotating the leg around the body. The leg stoppers are set at a fixed position on the main body and serve to ensure the front legs are at the proper angle before the jump is executed. Fig. 6.10 and the attached video illustrate the result of our experiment for both vaulting and aiming jump.

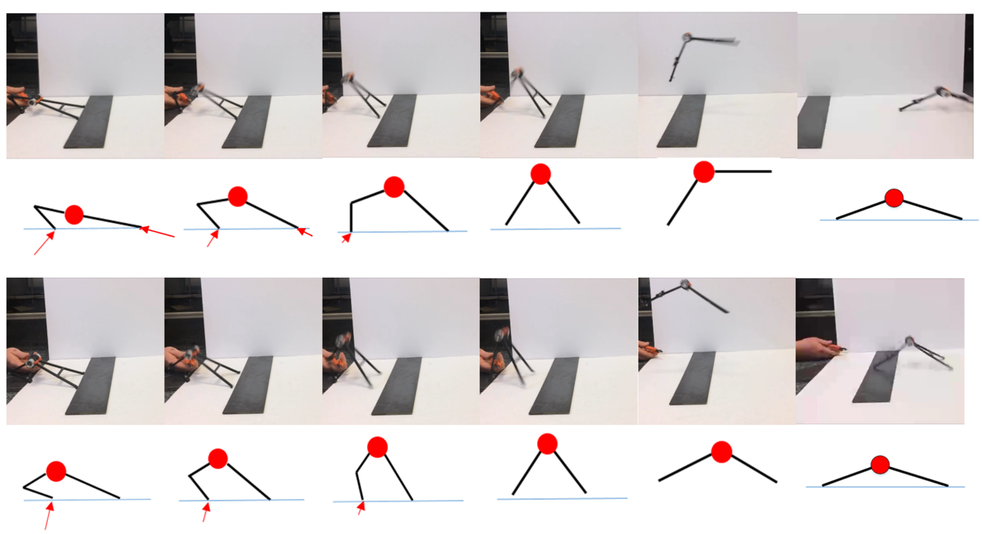

Figure 6.10: Experimental validation with two different front leg angle (0°and 45°) that cause vaulting and aiming respectively. The cartoons below the pictures demonstrate the reaction forces on the feet. In vaulting, the spider start jumping by assisting from the front leg and when the reaction force becomes zero, the jump switch to the aiming jump. For the aiming jump it is shown that there is no reaction force on front leg at the beginning.

6.7 Discussion

In this chapter, we investigated a model of the aiming mechanism used by jumping spiders. Through parameter exploration and dynamic analysis, we identified three critical jumping regimes: unsupported jumps, aiming jumps and vaulting jumps. Unsupported jumps were those for which the front leg lifted off the ground immediately at the beginning of the jump, and for which the final take-off angle was determined by the relative rates of energy release from the spring and the system falling forward under the influence of gravity. In the limit of fast energy release, these unsupported jumps converged on an “aiming” behavior, in which the take-off angle was the same as the initial line of action of the spring.

Vaulting jumps, in which the mechanism pivots around the front leg before launching, exhibited a different, and unexpected convergence behavior. Because the spring force pushes into the front leg during “low-aimed” jumps, its release rate is slowed; this allows the system more time to pivot forward, and results in a trajectory that is even flatter than its initial aimed direction. Unlike the unsupported jumps, these jumps do not converge to the “aiming” behavior with increased stiffness, and so can be considered a distinctly geometric effect.

In our future work, we will seek to enhance our model by adding more segments to the legs and incorporate rotation of the jumper’s body, as observed for spiders in [2]. Jumping spiders have also been observed to use anchored draglines to achieve maneuvering capabilities while in the air [100]; we aim to take advantage of our study of tethered projectiles in [101] to add similar capability to our jumping spider mechanism.

Chapter 7: Empirical Power Metric for Granular Snake

Locomotion over sand and other loose, flowing material is an ongoing challenge in mobile robotics. Snake robots, which can contact the ground along their whole body, have the potential to perform better in these environments than systems relying on wheels, tracks, or even legs for propulsion [1]. A major challenge in controlling snake robots, however, is coordinating their many degrees of freedom into useful motions; on granular media, this challenge is compounded by a lack of fundamental physical models for the robot-environment interaction. In this chapter, we investigate snake robot locomotion over granular surfaces via an empirical-geometric approach that is amenable to analysis and optimization.

7.1 Empirical Derivation of Local Connection and Power Metric

In this chapter, our goal is to characterize and optimize the motion of a snake robot over a bed of granular particles.

To do so we can empirically derive the local connection for an N-link snake robot swimming on a granular surface by (1) sampling a configuration ω, (2) commanding a small shape velocity $\dot{\omega}$ (3) measuring the resultant body velocity $\overset{\circ}{g}$ and power consumption, and (4) fitting the local connection $A(\alpha)$ and power metric to the data. This procedure is repeated over a uniform sampling of the shape space to generate a comprehensive model of the system.

After evaluating body velocity at every sampled shape configuration from experiment setup, the local connection can be derived by linear regression as the best-fit linear map from shape to body velocity. In addition, as explained in §4.3.2 we evaluate curvature of the vector field to derive the empirical height functions, as shown in Fig. 7.1. Red areas indicate that the local connection vector field has positive curvature, while black areas indicate negative curvature. The intensity of either color represents the magnitude of the curvature of the local connection vector field and white regions are where the curvature is zero.

Our model for the energy and power consumed by the snake robot as it changes shape is a dissipative Riemannian metric of the form

$$(\frac{dE}{dt})^2 = P^2 = \begin{bmatrix} \dot{\alpha_1} & \dot{\alpha_2} \end{bmatrix} \mathcal{M}_p \begin{bmatrix} \dot{\alpha_1} \\ \dot{\alpha_2} \end{bmatrix} \tag{7.1}$$

where the metric tensor

$$\mathcal{M}_p = \begin{bmatrix} a & \frac{1}{2}c \\ \frac{1}{2}c & b \end{bmatrix} \tag{7.2}$$

encodes the surrounding medias resistance to motion along different shape directions.[1] The energetic cost of a gait cycle is then

$$E^2_{cost} = \int d\alpha^T \mathcal{M}_p d\alpha \tag{7.3}$$

[1]This model is a Coulomb-friction equivalent to the viscous-friction metric discussed in detail in []

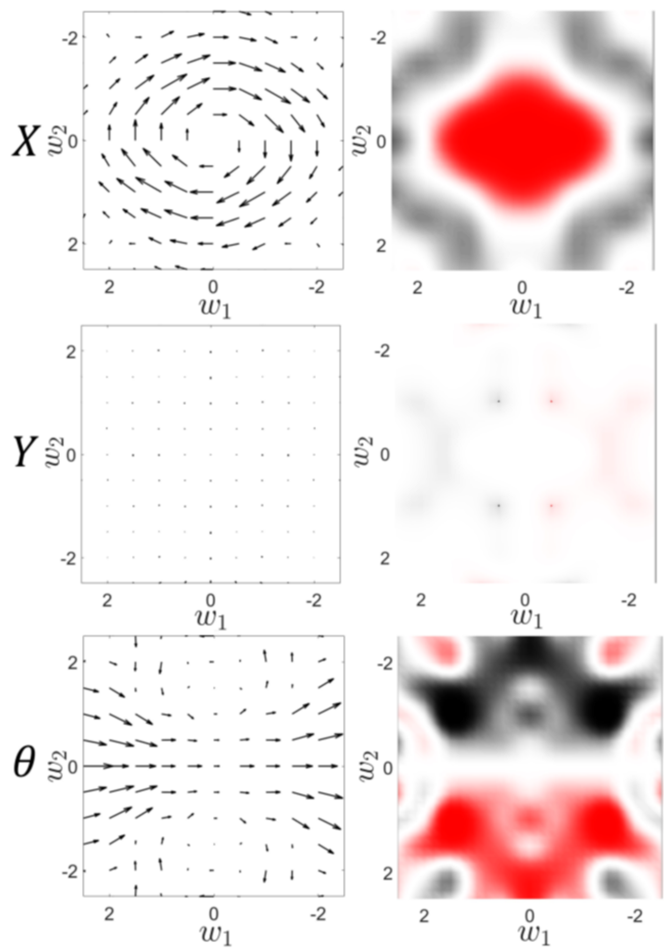

Figure 7.1: Empirical local connection vector field and height function of an 8-link snake robot slithering on the surface of 6mm plastic particles, represented in minimal perturbation body frame. The range of the curvature plots is ± 0.0152 body-lengths or ± 0.0483 radians per square unit of shape. Red, white and black indicate positive, zero and negative values respectively.

which is the pathlength of the cycle in the parameter space, weighted by $\mathcal{M}_p$.

To evaluate $\mathcal{M}_p$ experimentally, we used the high-fidelity joint-torque sensors on the snake robot to measure the mechanical load on the joints during a sequence of test motions. Under our model, we would expect to see the energy consumed for small motions around a given starting shape to fit a conical function whose coefficients correspond to the elements in the metric tensor,

$$a(d\alpha_1^2) + b(d\alpha_2^2) + c(d\alpha_1^2)(d\alpha_2^2) = P^2 dt^2 \tag{7.4}$$

and we find the set of coefficients that best fit our observations using a linear regression of the data: For each set of n values for $d\alpha$, P, and dt around a given starting shape, our model expectation is

$$\begin{bmatrix} (d\alpha_1^2)_1 & (d\alpha_1 d\alpha_2)_1 & (d\alpha_2^2)_1 \\ (d\alpha_1^2)_2 & (d\alpha_1 d\alpha_2)_2 & (d\alpha_2^2)_2 \\ . & . & . \\ . & . & . \\ (d\alpha_1^2)_n & (d\alpha_1 d\alpha_2)_n & (d\alpha_2^2)_n \end{bmatrix} \begin{bmatrix} a \\ b \\ c \end{bmatrix} = \begin{bmatrix} P^2 dt^2{}_1 \\ P^2 dt^2{}_2 \\ . \\ . \\ P^2 dt^2{}_n \end{bmatrix} \tag{7.5}$$

which is over constrained but has a best fit solution via the pseudo-inverse

$$\begin{bmatrix} a \\ b \\ c \end{bmatrix} = \begin{bmatrix} (d\alpha_1^2)_1 & (d\alpha_1 d\alpha_2)_1 & (d\alpha_2^2)_1 \\ (d\alpha_1^2)_2 & (d\alpha_1 d\alpha_2)_2 & (d\alpha_2^2)_2 \\ . & . & . \\ . & . & . \\ (d\alpha_1^2)_n & (d\alpha_1 d\alpha_2)_n & (d\alpha_2^2)_n \end{bmatrix}^+ \begin{bmatrix} P^2 {dt^2}_1 \\ P^2 {dt^2}_2 \\ . \\ . \\ P^2 {dt^2}_n \end{bmatrix} \tag{7.6}$$

giving a set of components for the metric tensor at that shape. The metric tensors at different shapes can be visualized via the Tissot indicatrix [17, 20], which illustrates the extent to which lengths according to the metric are distorted by the working parameterization. In these plots, unit circles according to the metric are displayed as ellipses, with the long axes of the ellipses corresponding to directions in which motion is easiest (i.e., for which a unit amount of effort changes the parameters the most). Fig. 7.2 illustrates the power dissipation metric for the non-linear system and the estimated one obtained from (7.2).

In Fig. 7.2 (A), we can see that moving around the shape space (passing a wave down the body) is easier than crossing the center of the shape space (straightening out the body and then curving it again). We can also see that it is slightly easier to move in the α_1 sine mode direction than the α_2 cosine mode direction, which parallels the observations in [17] that bending into a C shape costs more energy than bending into an S shape because the C motion sweeps the body through more of the surrounding medium. To remove some of the metric distortion captured by the Tissot indicatrices from the shape space, we can use a cartographic reparameterization [17] to find a set of coordinates that match the metric as much as is possible,

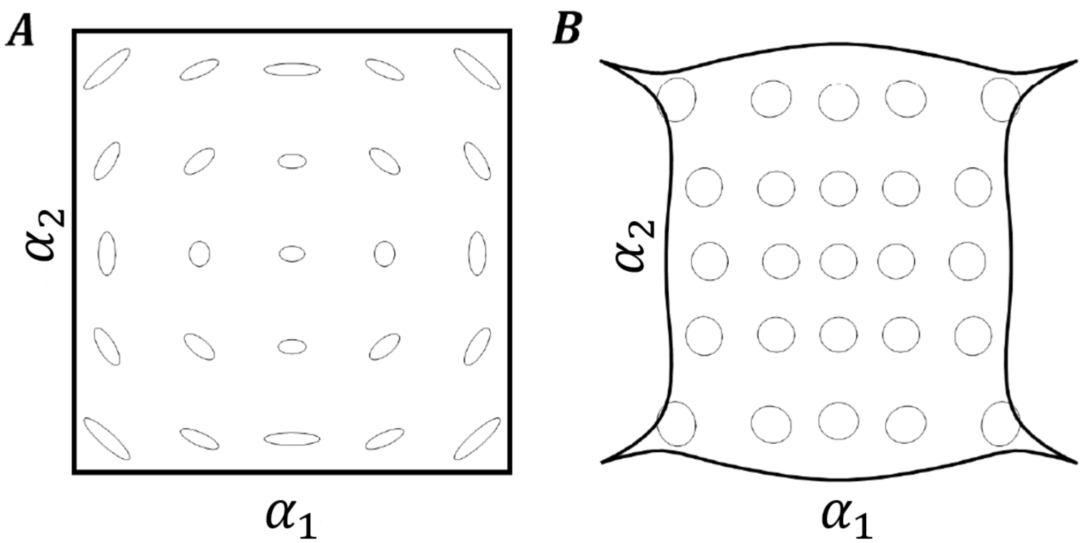

Figure 7.2: (A) Power dissipation metric in shape coordinates is shown. The long axis in the ellipse corresponds to less energy consumption per change in shape. (B) The metric as it appears in under a power-normalizing cartographic reparameterization.

in the same way that a conical map projection is a best-fit flat parameterization of the globe. This operation treats the metric distortions as pre-strains in an elastic sheet and relaxes these strains as much as possible while maintaining continuity in the space. As illustrated in Fig. 7.2 (B), applying this reparameterization to the shape space significantly reduces the distortion.

7.2 Discussion

In this chapter, we showed how to approximately fit a geometric model to a set of small test motions. The results of this chapter was implemented on experimental test data from Carnegie Mellon University which enables us to design a efficient gait for Serpenoid snake robot moving on granular surface. This work resulted in publishing a paper in Robotics Science and Systems (RSS) conference [13].

Chapter 8: Conclusion

In this work, we have incorporated geometric insights to develop a framework for motion planning. This framework, is built to facilitate studying, understanding and designing a gait for robotic locomotion.

We built the cost function for inertial systems based on the concept of geodesic and metric in differential geometry to find an effective and efficient way for robots to move and show how the motion is connected to the system geometry and inertia. In fact, we introduced curvature and acceleration as general characteristics of the system that describe the properties of the system in a meaningful way and with fewer terms.

These concepts were used to demonstrate that start-stop paths following geodesics are not in general torque-squared-optimal for robotic manipulators. We introduced a novel "biased geodesic curvature" takes into account the leverage that the actuators have on the system motion via their projection on the system's dynamic manifold, such that the minimum-torque-squared trajectories for the manipulator are those that minimize the biased geodesic curvature.

To demonstrate the principle that start-stop motion along geodesic paths is not torque-optimal, we conducted an experiment using a parallel actuator (a Minitaur leg). For the sake of simplification, we added a point-mass to the end-effector of a lightweight parallel mechanism, making the geodesics simple straight-line motions.

For start-stop motions, Moving in an arc that used the biased geodesic curvature to take into account leverage of the motors on the system dynamics required less torque-squared than did moving along the geodesic.

Furthermore, we have incorporated geometric insights to develop a framework for motion planning of crawling systems. This framework, is built to facilitate studying, understanding and designing a gait for robotic locomotion.We modified the torque-squared cost function to be proportional to the change of the gait's size. Utilizing this cost function, we demonstrated the results of our optimizer for floating snake, the three-link and Serpenoid swimmers in the high Reynolds fluid which has metric induced by inertia and compared the results with the results obtained from pathlength cost function. The results revealed that, the gaits found from the inertia based optimizer are a little larger than the gaits found by drag based optimizer which matches with the mathematical equation we derived (the inertial cost is proportional to square root of the size of the gait whereas the drag cost is proportional to the size of the gait). Furthermore, we demonstrated the pacing effect for inertial systems and how the way-points are distributed through the gait. The results revealed a structure for the optimal solution for these types of robots.

The concept of inertia and natural dynamic in impact dynamics was studied and a framework for understanding the impact dynamics was developed. We investigated the direction in which a moving projectile anchored by a tether will bounce when the tether becomes taut. In doing so, we identified five critical points in the puck's dynamics: The puck is *maximally deflected* when the tether's line of action passes through the center of mass, and so transfers no energy into the rotational mode. The puck is *minimally deflected* when the tether's line of action is at right angles to the line connecting its attachment point to the center of mass. In this configuration, the impulse's moment-to-force ratio is large, and the puck rotates into the tether (causing it to go slack) before it can fully redirect its linear momentum. The puck is *maximally decelerated* when the tether's line of action is tangent to the puck's radius of gyration, and so optimally transfers energy into the rotational mode and out of the translational modes. The puck's bounce is predicted using the energy ellipse and impact line of action even when puck has *non-zero rotational velocity*. The puck's bounce is predicted considering the effect of *energy dissipation* on the tether using the family of the energy ellipses intersecting with tether line of action.

The system with fast energy release such as jumping robots were studied and investigated specifically a model of the aiming mechanism used by jumping spiders. Through parameter exploration and dynamic analysis, we identified three critical jumping regimes: unsupported jumps, aiming jumps and vaulting jumps. Unsupported jumps were those for which the front leg lifted off the ground immediately at the beginning of the jump, and for which the final take-off angle was determined by the relative rates of energy release from the spring and the system falling forward under the influence of gravity. In the limit of fast energy release, these unsupported jumps converged on an "aiming" behavior, in which the take-off angle was the same as the initial line of action of the spring.

Vaulting jumps, in which the mechanism pivots around the front leg before launching, exhibited a different, and unexpected convergence behavior. Because the spring force pushes into the front leg during “low-aimed” jumps, its release rate is slowed; this allows the system more time to pivot forward, and results in a trajectory that is even flatter than its initial aimed direction. Unlike the unsupported jumps, these jumps do not converge to the “aiming” behavior with increased stiffness, and so can be considered a distinctly geometric effect.

APPENDICES

Appendix A: Effect of Contact Regions on Locomotion of Snake Robots

A.1 Introduction

Robot locomotion is a method that a robot uses to move from one point to another point and consists of interaction forces, mechanism, an actuator that generate forces. Snakes locomotion has gained researchers attention since they can move large distance with consuming very little energy. In addition, wheeled robots have fundamental problems to perform over rough terrains. Legged robots have better functionality over irregularities; however, they have stability problem as well as a limited capability to move. Because of the high level of redundancy in snakes, they are very stable and reliable in moving.

Snake locomotion through lateral undulation is based on a continuous interaction of the snake's entire body with its environment. The snake bends its body so that it could push against the environment's obstacles. Reaction forces from the so-called push-points constitute together the total propulsive force required for progression in a given direction [102]. Most of the researches who have been working on snake robots, use the passive wheels to decreases the friction in the longitudinal direction and cause the resultant friction forces of both lateral and longitudinal in the forward direction which make the snake propel forward [103].

However as aforementioned, wheeled robots cannot operate in an uncertain or irregular environment. On the other hand, observing the real snake locomotion reveals that while performing the lateral undulation, the snake‘s body is not completely in contact with ground, but snake lifts some parts of its body and concentrates its body weight only on few points touching the ground, so that it can create push points and it helps snake to propel forward more efficiency.

This work addresses this crucial behavior that has been paid less attention in previous studies. We are considering three different scenarios in snake serpentine locomotion and will consider the efficiency of the cost of transport for each of them. We are considering the robot locomotion in low Reynolds numbers similar to the three-link swimmer [104] to take advantage of the swimming dynamic.

A.2 Literature Review

Snake robots have been studied since 1971, with Hiroses well-known work on the Active Cord Mechanism (ACM) [105]. Recent effort has been directed towards mechanisms that can assume full three-dimensional shapes. Mori and Hiroses ACM-R3 [106], modular snakes (modsnakes) [107], and Goldman and Hongs HyDRAS [108].

Hiroses early work on snake robots identified the Serpenoid curve (Hirose 1993) as the fundamental shape function simulating the backbones resembling the biological snakes while executing common gaits and used this curve as the basis for robotic gaits. Chirikjian and Burdick [109, 110] developed modal functions for describing arbitrary backbone curves and algorithms for fitting discrete serial mechanisms to these curves.

The second branch of gait development, also inspired by Hiroses work, has taken a lower-level, wave-based approach. The joint angles in a serpenoid-curve gait are specified by a sinusoidal traveling wave function, and, by extension, other gaits can be produced by modifying the form of this wave [111]. In our work, we are focusing on the extension of serpenoid motion utilized with a biological snake which basically is carried out when the snake lifts some parts of its body to create push points.

A.3 Geometric Modeling and Analysis of Locomotion

To model the locomotion system we divide the configuration space Q into a position space G and shape space M, such that the position $g \in G$ locates the system in the world, and the shape $r \in M$ gives the relative arrangements of its bodies (Fig. 3.4). This separation is a means that demonstrates that how the change in shape effects on the displacement of the body. In geometric mechanic, there exists a linear relationship between changes in shape velocity $\dot{r}$ and body velocity $\mathring{g}$,

$$\mathring{g} = -A(r)\dot{r} \tag{A.1}$$

where $A(r)$ is the local connection matrix and acts like a Jacobian that maps shape velocity to the body velocity [7]. This can be used as a tool to find an optimize gate for the snake robot. This equation is a reconstruction equation in

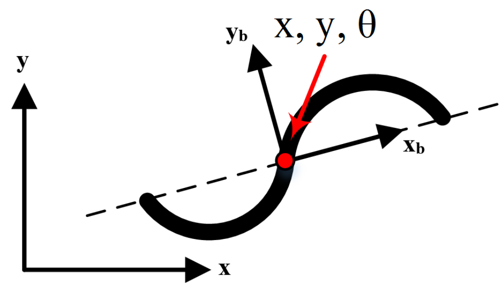

Figure A.1: Serpenoid model.

which it can be integrated to reconstruct the position trajectory from given shape changes.

The connection vector can be considered a gradient of the body velocity with respect to the shape velocity. The Stokes theorem is a mean that can be used to approximate the net displacement over specified gaits. The Stokes theorem equates the line integral along a closed curve on a vector field V on a space U to the integral of the curl of that vector field over a surface bounded by the curve. Therefore, by integrating the curvature of A we can find the net displacement and applying the Stokes theorem covert this line integral to into an area integral.

$$\Delta g = \oint_{\phi} -A(r)dr \approx \iint_{\phi} \overbrace{-curl A + [A_1, A_2]}^{curvature} dr \tag{A.2}$$

The Lie bracket of the local connection measures the net translation that is induced by a differential oscillation in the system's shape and prevent the net integral from being self-canceling [55]. This effect corresponds to the noncommutativity of the system's position.

According to [55], the noncommutativity approximation is most accurate in minimum perturbation coordinates which is the mean orientation of the individual links and the center of mass location space and can be completely identified through a Hodge-Helmholtz decomposition of the system dynamics.

A.3.1 The low Reynolds and its characteristic

In this research, we are taking advantage of the dynamic of low Reynolds number. In the low Reynolds number the drag forces dominate the inertial forces because the inertia forces are very small in comparison to the drag forces, and can be neglected, therefore the net drag forces on the system are zero. The equations of drag forces are a linear function of body velocity, shape velocity, and shape changes. The drag forces and moments on the *ith* link are based on a principle of lateral drag forces being approximately twice the longitudinal forces [104], with the moment around the center of the link found by assuming the lateral drag forces to be linearly distributed along the link according to its rotational velocity

$$F_{i,x} = \int_{-L}^{L} cL\zeta_{i,x}dl \tag{A.3}$$

$$F_{i,y} = \int_{-L}^{L} 2cL\zeta_{i,y}dl \tag{A.4}$$

$$M_i = \int_{-L}^{L} \frac{2}{3}cL(l\zeta_{i,\theta})dl \tag{A.5}$$

where $F_{i,x}$ and $F_{i,y}$ are respectively the longitudinal and lateral forces, M_i the moment, c is the differential viscous drag constant, an ζ_i 's are the body velocities of the i_{th} segments.

The net forces can be expressed in the term of velocities

$$F = \omega(\alpha) \begin{bmatrix} \zeta \\ \dot{\alpha} \end{bmatrix} \tag{A.6}$$

where ω is a 3x5 matrix. As it was explained before in low Reynolds number, the net forces and moments on an isolated system should be zero. Therefore, we can write the A.6 as below:

$$\begin{bmatrix} 0 \\ 0 \\ 0 \end{bmatrix} = \begin{bmatrix} {\omega_g}^{3x3} \; {\omega_r}^{3x2} \end{bmatrix} \begin{bmatrix} \zeta \\ \dot{\alpha} \end{bmatrix} \tag{A.7}$$

Therefore, the local connection takes the following form

$$A = -{\omega_g}^{-1} \omega_r \dot{\alpha} \tag{A.8}$$

A.3.2 Constraint Curvature Function and Power Metric

The constraint curvature functions (CCFs) in the shape space is a tool that can capture the net motion resulting from an arbitrary choice of the gaits. However, CCF doesn't determine the efficiency of the movement. To find the optimal path, the cost of the gait through the shape change space of the system needs to be calculated. As stated in [40], the cost of a gait can be captured by its path-length according to a power-consumption distance metric on the space by showing the circle distortion to an ellipse. Path-length closely corresponds to energy usage. Then by normalizing the coordinate according to power metric, one can see the effort which corresponds closely to arc-length.

To normalize the height function regarding the power metric, we consider our shape space as an elastic sheet in which in the current shape it corresponds to the current configuration and in relaxes case it corresponds to minimum energy configuration. The relaxation is done based on Airy criterion as explained in [40]. As the sheet relaxes, the points in the initial coordinate, move to the new positions which are consistent with the distance metric we calculated.

A.3.3 Backbone Curve

A fundamental tool for creating a gait of the snake robot is a backbone curve which can capture the infinitesimal shape of the snake robot and produce the desired gait [109, 112]. Although backbone curves are geometrically intuitive, they cannot be used directly for generating the control inputs. The backbone curve allows to access to the underlying physics of serpenoid motion and also, it helps to apply the analysis to snake robots with different actuation.

In the continuous backbone curve the Cartesian position of points on a nonextensible backbone curve can be intrinsicly parameterized by:

$$x(s,t) = \int_0^s sin(\int_0^\sigma k(\mu,t)d\mu)d\sigma \tag{A.9}$$

where $k(s,t)$ is the curvature function and defined in the way that a positive curvature means bending in a clockwise sense.

$$\kappa = \alpha(t)k(s) \tag{A.10}$$

where $k(s)$ is a curvature mode and $a_s(t)$ is the modal participation factor. In order to, have the locomotion travel forward, it is required to choose $\alpha(t)$ to be a cyclic function to cause the robots curvature changes. Therefore, the Serpenoid traveling wave can be described as weighted sums of sine and cosine mode that is described in Fig. A.2 and the curvature is defined as:

$$\kappa = \begin{bmatrix} sin(s) & cos(s) \end{bmatrix} \begin{bmatrix} \alpha_1 \\ \alpha_2 \end{bmatrix} \tag{A.11}$$

A.3.4 Gaussian Function

There are two different scenarios we are considering: first is when the drag forces are maximum in the area with the highest curvature and zero where curvature of the body is zero (This is called elbow down which means snake uses the push points at the curve parts by lifting the other parts of its body up and propels its body forward). Second is when the maximum drag force occurs in the parts where the

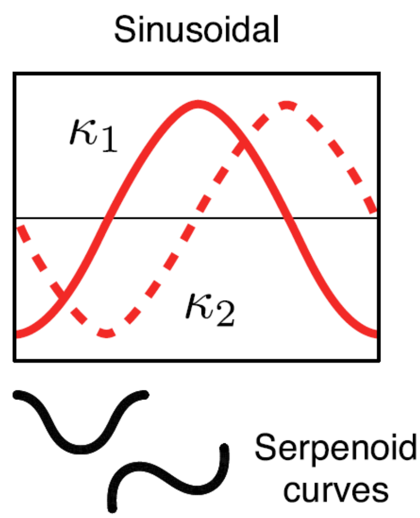

Figure A.2: Serpenoid locomotion is produced by combining the two different mode shapes.

curvature of the body is zero and parts with maximum curvature has almost zero or close to the zero drag forces (This is called elbow up which means snake pushes the point along the straight body line to produce the push points). To apply this effects to the system, we use the Gaussian distribution function as a coefficient of drag constant to form the variable contact area on the snakes body

$$GDF_{eu} = e^{-a\|K\|^2} \tag{A.12}$$

$$GDF_{ed} = \begin{cases} e^{-a(\|K\|-1)^2} & \text{if } \|K\| < 0 \\ e^{-a(\|K\|+1)^2} & \text{if } \|K\| > 0 \\ 0 & \text{if } \|K\| = 0 \end{cases} \tag{A.13}$$

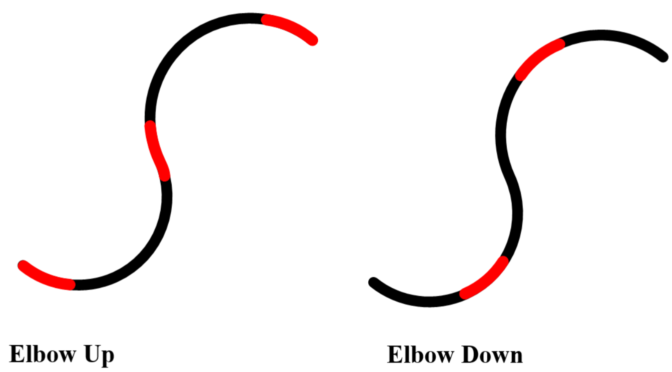

Figure A.3: The contact area for elbow up and elbow down.

The first equation is used for elbow up and the second one is used for elbow down configuration. Where a is the participation coefficient of the curvature function and K is the normalized curvature function calculated as the following equation,

$$\|K\| = \frac{\begin{bmatrix} k_1(s) & k_2(s) \end{bmatrix} \begin{bmatrix} \alpha_1 \\ \alpha_2 \end{bmatrix}}{\sqrt{\begin{bmatrix} \alpha_1 & \alpha_2 \end{bmatrix} \begin{bmatrix} \alpha_1 \\ \alpha_2 \end{bmatrix} \begin{bmatrix} k_1(s) & k_2(s) \end{bmatrix} \begin{bmatrix} k_1(s) \\ k_2(s) \end{bmatrix}}} \tag{A.14}$$

Fig. A.3 illustrates how the Gaussian distribution function effects on area of the contact.

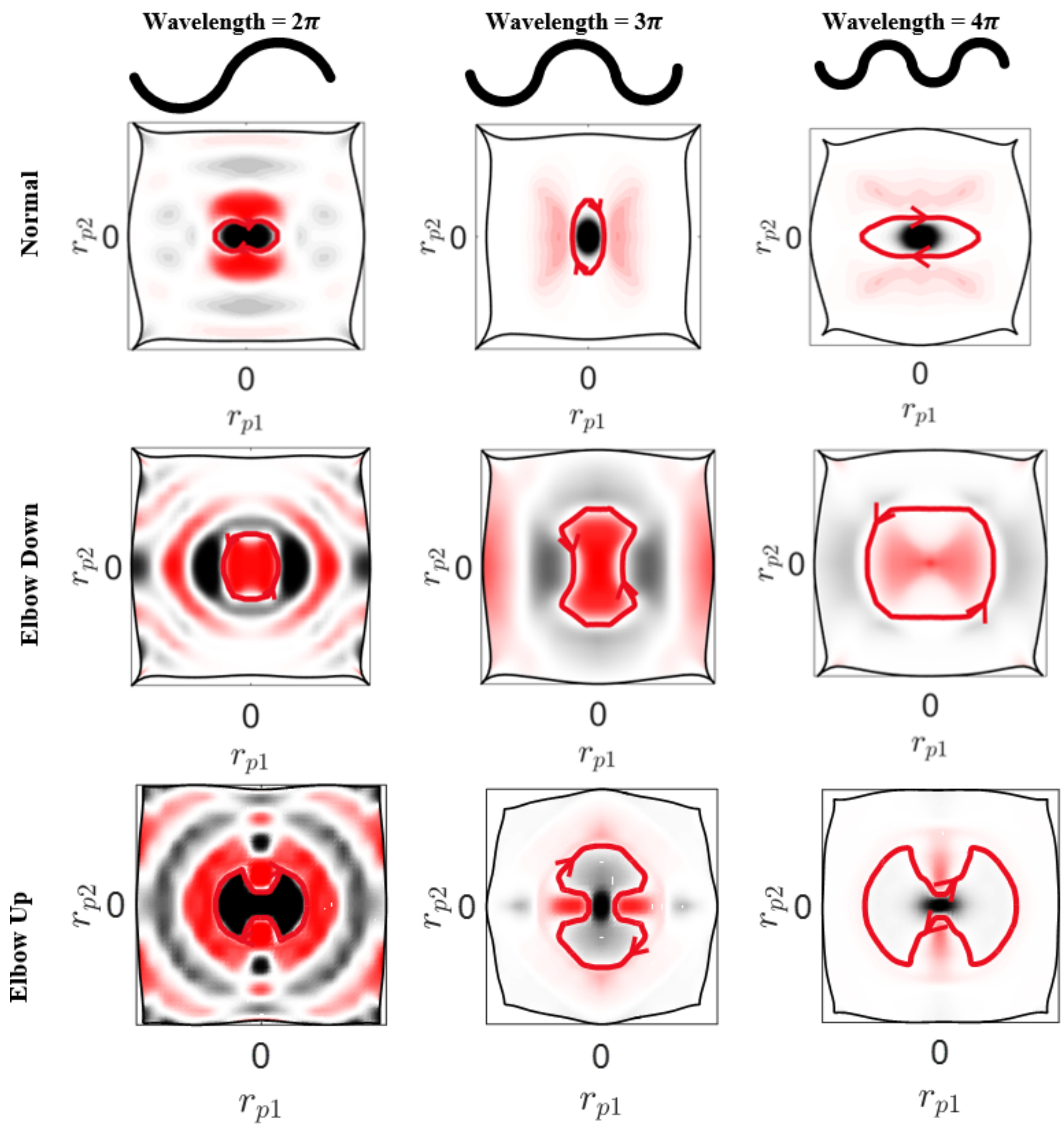

Figure A.4: X height function for the low Reynolds number of a swimmer continuous snake robot

A.4 Analysis and Results

The amplitude of the curvature can be represented by the gait in the shape space. This gait can be a circle and it will produce the serpenoid locomotion. Therefore, the radius of the circle is the curvature amplitude. Increasing the amplitude of the gait such that it encircles the maximum red area, increases the displacement. That observation declares that the displacement is a function of the curvature and amplitude. In addition to the circle gait, based upon the maximum efficiency and displacement, gaits may have different shapes. Maximum displacement gait occurs where there is a zero contour in height function. Fig. A.4 shows the X- height function in minimal perturbation body frame. In order to have a better visualization, the height function are represented in normalized coordinate as explained in section A.3.2. The plot illustrates the height function and zero contour for the different number of wavelength.

Fig. A.5 shows the behavior of different number of wave lengths over max displacement and efficiency for all three scenarios.

For elbow up, increasing the number of wavelengths, decreases both the displacement and increases the efficiency to some extent, then it starts to lose the efficiency as well. That is because the main push points are created at the center line of the direction of motion and lower wavelength means having bigger arc shape which contributes in greater displacement in each cycle and it requires more effort. Likewise, the same pattern is observed for the normal case which results from the existence of the higher drag forces in the lateral direction than the longitudinal

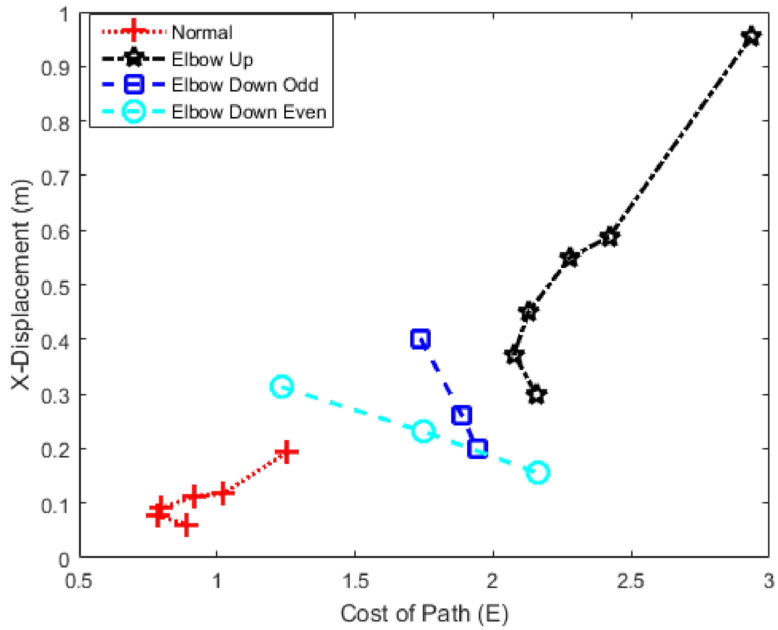

Figure A.5: Displacement and efficiency for normal, elbow up and elbow down.

one.

For the elbow down case, by observing the behavior of the odd and even modes individually one can see that increasing the number of wavelengths decreases both the displacement and cost of the path. That means, bigger arc in the body is more efficient. Comparing the results of the odd and even wavelengths, it can be seen that increasing the wavelength has a faster rate in decreasing the efficiency in even wavelengths. Also, the displacement for the odd number of wavelengths is greater than the even wavelengths and that is because as it is shown in figure Fig. A.6 for odd wavelengths, the forces are balanced at the side of the snake which leads to less wobbling motion.

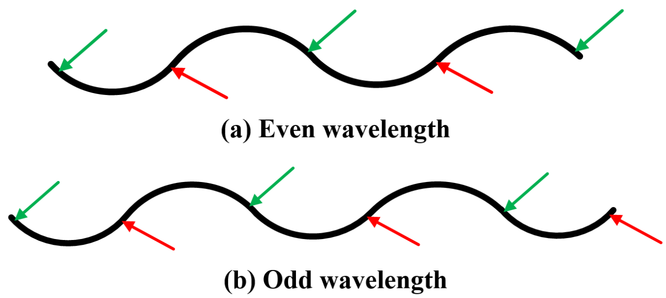

(a) Even wavelength

(b) Odd wavelength

Figure A.6: Distribution of drag forces for even and odd wavelength are shown.

Furthermore, we examined the influence of the contact area for both elbow up/down cases. As the contact area becomes pointier, it gets better in term of displacement and the cost of the gait. That is because fewer points of the body are in contact with the ground which means less drag forces in the longitudinal direction. Furthermore, in elbow down locomotion when the area with more curvature becomes close to the point, the longitudinal drag force on that point contributes in forward locomotion.

A.5 Conclusions

We proposed an improvement for serpentine locomotion for a snake robot that makes it able to move in the flat surface without aiming the obstacles. We simulated three possible different scenarios for modeling the contact points through the snake's body. Then we find the zero contour on height function which represents the maximum displacement. Afterward, we showed that the elbow up case is more efficient in both terms of displacement and efficiency. The efficiency for elbow up case increased by increasing the number of wavelength to some extent and then start to reduce. For elbow down case, it was shown that the more efficient case occurs in a lower number of wavelengths and the rate of changes for even and odd wavelengths are different. For the future work, we are planning to compare the current results with the triangular traveling wave.

Bibliography

[1] S. Ramasamy and R. L. Hatton, "Soap-bubble optimization of gaits," in *Decision and Control (CDC), 2016 IEEE 55th Conference on*, pp. 1056–1062, IEEE, 2016.

[2] D. E. Hill, "Targeted jumps by salticid spiders," in *2006*, pp. 1–28.

[3] A. Piazzi and A. Visioli, "Global minimum-jerk trajectory planning of robot manipulators," *IEEE transactions on industrial electronics*, vol. 47, no. 1, pp. 140–149, 2000.

[4] A. Aloulou and O. Boubaker, "Minimum jerk-based control for a three dimensional bipedal robot," *Intelligent Robotics and Applications*, pp. 251–262, 2011.

[5] S. Lu and Y. Li, "Minimum-jerk trajectory planning of a 3-dof translational parallel manipulator," in *ASME 2015 International Design Engineering Technical Conferences and Computers and Information in Engineering Conference*, pp. V05CT08A009–V05CT08A009, American Society of Mechanical Engineers, 2015.

[6] V. Kumar, M. Zefran, and J. P. Ostrowski, *Motion planning and control of robots*. New York: Wiley, 1999.

[7] R. L. Hatton and H. Choset, "Geometric motion planning: The local connection, stokes theorem, and the importance of coordinate choice," vol. 30, no. 8, pp. 988–1014.

[8] S. E. Engelbrecht, "Minimum principles in motor control," *Journal of Mathematical Psychology*, vol. 45, no. 3, pp. 497–542, 2001.

[9] M. D. K. Breteler, R. G. Meulenbroek, and S. C. Gielen, "An evaluation of the minimum-jerk and minimum torque-change principles at the path, trajectory, and movement-cost levels," *Motor Control*, vol. 6, no. 1, pp. 69–83, 2002.

[10] A. Biess, D. G. Liebermann, and T. Flash, "A computational model for redundant human three-dimensional pointing movements: integration of independent spatial and temporal motor plans simplifies movement dynamics," *Journal of Neuroscience*, vol. 27, no. 48, pp. 13045–13064, 2007.

[11] A. Biess, T. Flash, and D. G. Liebermann, "Riemannian geometric approach to human arm dynamics, movement optimization, and invariance," *Physical Review E*, vol. 83, no. 3, p. 031927, 2011.

[12] A. Biess, "Shaping of arm configuration space by prescription of non-euclidean metrics with applications to human motor control," *Physical Review E*, vol. 87, no. 1, p. 012729, 2013.

[13] J. Dai, H. Faraji, C. Gong, R. L. Hatton, D. I. Goldman, and H. Choset, "Geometric swimming on a granular surface,"

[14] L. N. Hand and J. D. Finch, *Analytical mechanics*. Cambridge University Press, 1998.

[15] J. P. Richard Koch, *Differential Geometry Notes - University of Oregon*. 2004.

[16] R. L. Hatton, T. Dear, and H. Choset, "Kinematic cartography and the efficiency of viscous swimming," *IEEE Transactions on Robotics*, 2017.

[17] R. L. Hatton, Y. Ding, H. Choset, and D. I. Goldman, "Geometric visualization of self-propulsion in a complex medium," *Physical review letters*, vol. 110, no. 7, p. 078101, 2013.

[18] G. Rodnay and E. Rimon, "Isometric visualization of configuration spaces of two-degrees-of-freedom mechanisms," *Mechanism and machine theory*, vol. 36, no. 4, pp. 523–545, 2001.

[19] L. Zhang and C. Zhou, "Smooth and energy saving gait planning for humanoid robot using geodesics," *Applied Bionics and Biomechanics*, vol. 9, no. 4, pp. 457–467, 2012.

[20] L. Zhang and C. Zhou, "Robot optimal trajectory planning based on geodesics," in *Control and Automation, 2007. ICCA 2007. IEEE International Conference on*, pp. 2433–2436, IEEE, 2007.

[21] L. Zhang and C. Zhou, "Kuka youbot arm shortest path planning based on geodesics," in *Robotics and Biomimetics (ROBIO), 2013 IEEE International Conference on*, pp. 2317–2321, IEEE, 2013.

[22] J. M. Hollerbach and T. Flash, "Dynamic interactions between limb segments during planar arm movement," *Biological cybernetics*, vol. 44, no. 1, pp. 67–77, 1982.

[23] J. Boessenkool, E.-J. Nijhof, and C. Erkelens, "A comparison of curvatures of left and right hand movements in a simple pointing task," *Experimental Brain Research*, vol. 120, no. 3, pp. 369–376, 1998.

[24] K. C. Nishikawa, S. T. Murray, and M. Flanders, "Do arm postures vary with the speed of reaching?," *Journal of Neurophysiology*, vol. 81, no. 5, pp. 2582–2586, 1999.

[25] G. Kenneally, A. De, and D. E. Koditschek, "Design principles for a family of direct-drive legged robots," *IEEE Robotics and Automation Letters*, vol. 1, no. 2, pp. 900–907, 2016.

[26] L. Zhang and C. Zhou, "Optimal three-dimensional biped walking pattern generation based on geodesics," *International Journal of Advanced Robotic Systems*, vol. 14, no. 2, p. 1729881417696235, 2017.

[27] B. Berret, E. Chiovetto, F. Nori, and T. Pozzo, "Evidence for composite cost functions in arm movement planning: an inverse optimal control approach," *PLoS computational biology*, vol. 7, no. 10, p. e1002183, 2011.

[28] T. Flash and N. Hogan, "The coordination of arm movements: an experimentally confirmed mathematical model," *Journal of neuroscience*, vol. 5, no. 7, pp. 1688–1703, 1985.

[29] B. K. Horn, "The curve of least energy," *ACM Transactions on Mathematical Software (TOMS)*, vol. 9, no. 4, pp. 441–460, 1983.

[30] X. Li and J. Xue, "Complex quadratic bézier curve on unit circle," in *International Conference on Logistics Engineering, Management and Computer Science (LEMCS 2014)*, Atlantis Press, 2014.

[31] B. Ravani, "Bezier curves on riemannian manifolds and lie groups witli kinematics applications," 1995.

[32] M. Hofer and H. Pottmann, "Energy-minimizing splines in manifolds," *ACM Transactions on Graphics (TOG)*, vol. 23, no. 3, pp. 284–293, 2004.

[33] M. Hofer, "Constrained optimization with energy-minimizing curves and curve networks: a survey," in *Proceedings of the 23rd Spring Conference on Computer Graphics*, pp. 27–35, ACM, 2007.

[34] L. Noakes, G. Heinzinger, and B. Paden, "Cubic splines on curved spaces," *IMA Journal of Mathematical Control and Information*, vol. 6, no. 4, pp. 465–473, 1989.

[35] P. Crouch and F. S. Leite, "Geometry and the dynamic interpolation problem," in *American Control Conference, 1991*, pp. 1131–1136, IEEE, 1991.

[36] S. Kadam and R. N. Banavar, "Variational dynamic interpolation for kinematic systems on trivial principal bundles," *arXiv preprint arXiv:1808.00414*, 2018.

[37] A. Borum, D. Matthews, and T. Bretl, "State estimation and tracking of deforming planar elastic rods," in *Robotics and Automation (ICRA), 2014 IEEE International Conference on*, pp. 4127–4132, IEEE, 2014.

[38] M. W. Spong, S. Hutchinson, M. Vidyasagar, *et al.*, *Robot modeling and control*, vol. 3. Wiley New York, 2006.

[39] S. Ramasamy and R. L. Hatton, "Geometric gait optimization beyond two dimensions," in *American Control Conference (ACC), 2017*, pp. 642–648, IEEE, 2017.

[40] R. Hatton and H. Choset, "Kinematic cartography for locomotion at low reynolds numbers,"

[41] S. D. Kelly, "The mechanics and control of driftless swimming," *SIAM J. of Control and Optimization*, 2011.

[42] J. B. Melli, C. W. Rowley, and D. S. Rufat, "Motion planning for an articulated body in a perfect planar fluid," *SIAM Journal on applied dynamical systems*, vol. 5, no. 4, pp. 650–669, 2006.

[43] A. Shapere and F. Wilczek, "Geometry of self-propulsion at low reynolds number," *Journal of Fluid Mechanics*, vol. 198, pp. 557–585, 1989.

[44] R. M. Murray and S. S. Sastry, "Nonholonomic motion planning: Steering using sinusoids," *IEEE Transactions on Automatic Control*, vol. 38, no. 5, pp. 700–716, 1993.

[45] S. D. Kelly and R. M. Murray, "Geometric phases and robotic locomotion," *Journal of Robotic Systems*, vol. 12, no. 6, pp. 417–431, 1995.

[46] G. C. Walsh and S. S. Sastry, "On reorienting linked rigid bodies using internal motions," *IEEE Transactions on Robotics and Automation*, vol. 11, no. 1, pp. 139–146, 1995.

[47] G. C. Walsh and S. S. Sastry, "On reorienting linked rigid bodies using internal motions," *Proceedings of the 30th*, no. 1, 1991.

[48] E. Kanso, J. E. Marsden, C. W. Rowley, and J. B. Melli-Huber, "Locomotion of articulated bodies in a perfect fluid," *Journal of Nonlinear Science*, vol. 15, no. 4, pp. 255–289, 2005.

[49] J. P. Ostrowski, *The mechanics and control of undulatory robotic locomotion.* PhD thesis, California Institute of Technology, 1996.

[50] J. P. Ostrowski, J. P. Desai, and V. Kumar, "Optimal gait selection for nonholonomic locomotion systems," *The International journal of robotics research*, vol. 19, no. 3, pp. 225–237, 2000.

[51] E. Shammas, K. Schmidt, and H. Choset, "Natural gait generation techniques for multi-bodied isolated mechanical systems," in *Robotics and Automation, 2005. ICRA 2005. Proceedings of the 2005 IEEE International Conference on*, pp. 3664–3669, IEEE, 2005.

[52] E. A. Shammas, H. Choset, and A. A. Rizzi, "Geometric motion planning analysis for two classes of underactuated mechanical systems," *The International Journal of Robotics Research*, vol. 26, no. 10, pp. 1043–1073, 2007.

[53] E. A. Shammas, H. Choset, and A. A. Rizzi, "Towards a unified approach to motion planning for dynamic underactuated mechanical systems with non-holonomic constraints," *The International Journal of Robotics Research*, vol. 26, no. 10, pp. 1075–1124, 2007.

[54] J. E. Marsden, "Geometric foundations of motion and control," in *Motion, Control, and Geometry: Proceedings of a Symposium, Board on Mathematical Science, National Research Council Education, National Academies Press, Washington, DC*, 1997.

[55] R. Hatton and H. Choset, "Nonconservativity and noncommutativity in locomotion," *The European Physical Journal Special Topics*, vol. 224, no. 17-18, pp. 3141–3174, 2015.

[56] R. L. Hatton and H. Choset, "Geometric swimming at low and high reynolds numbers," *IEEE Transactions on Robotics*, vol. 29, no. 3, pp. 615–624, 2013.

[57] Y.-K. Chen, C.-P. Liao, F.-Y. Tsai, and K.-J. Chi, "More than a safety line: jump-stabilizing silk of salticids," *Journal of the Royal Society: Interface*, vol. 10, no. 87, p. 20130572, 2013.

[58] "http://history.nasa.gov/apollo204/zorn/white.htm."

[59] G. Gilardi and I. Sharf, "Literature survey of contact dynamics modelling," vol. 37, no. 10, pp. 1213–1239.

[60] E. T. Whittaker and S. W. McCrae, *A Treatise on the Analytical Dynamics of Particles and Rigid Bodies.* Cambridge University Press, 4 edition ed.

[61] E. Routh, *Dynamics of a System of Rigid Bodies.* MacMillan, Co, London.

[62] R. M. Brach, "Formulation of rigid body impact problems using generalized coefficients," vol. 36, no. 1, pp. 61–71.

[63] R. M. Brach, "Rigid body collisions," vol. 56, no. 1, pp. 133–138.

[64] J. B. Keller, "Impact with friction," vol. 53, no. 1, pp. 1–4.

[65] Y. Wang and M. T. Mason, "Two-dimensional rigid-body collisions with friction," vol. 59, no. 3, pp. 635–642.

[66] Y. Hurmuzlu and T.-H. Chang, "Rigid body collisions of a special class of planar kinematic chains," vol. 22, no. 5, pp. 964–971.

[67] I. Han and B. J. Gilmore, "Multi-body impact motion with frictionanalysis, simulation, and experimental validation," vol. 115, no. 3, pp. 412–422.

[68] H. Arisumi, K. Yokoi, and K. Komoriya, “Casting manipulation #x2014;midair control of a gripper by impulsive force,” vol. 24, no. 2, pp. 402–415.

[69] H. Arisumi, K. Yokoi, and K. Komoriya, “Kendama game by casting manipulator,” in *2005 IEEE/RSJ International Conference on Intelligent Robots and Systems, 2005. (IROS 2005)*, pp. 3187–3194.

[70] H. Arisumi, K. Yokoi, and K. Komoriya, “Casting manipulation (braking control for catching motion),” in *IEEE International Conference on Robotics and Automation, 2000. Proceedings. ICRA '00*, vol. 2, pp. 1961–1968 vol.2.

[71] H. Arisumi and K. Komoriya, “Catching motion of casting manipulation,” in *2000 IEEE/RSJ International Conference on Intelligent Robots and Systems, 2000. (IROS 2000). Proceedings*, vol. 3, pp. 2351–2357 vol.3.

[72] V. Ciocanel and W. T., “Modeling and numerical simulation of the nonlinear dynamics of the parametrically forced string pendulum,” in *Society for Industrial and Applied Mathematics 2012*, June 2012.

[73] R. Cross, “The bounce of the ball,” in *American Association of Physics Teachers 1998.*, pp. 222–227, Oct. 1998.

[74] R. Cross, “Bounce of a spinning ball near normal incidence,” in *American Association of Physics Teachers 2005.*, pp. 914–920, Mar. 2005.

[75] M. W. Spong, “Impact controllability of an air hockey puck,” *Systems & Control Letters*, vol. 42, no. 5, pp. 333–345, 2001.

[76] A. Chatterjee, *Rigid body collisions: some general considerations, new collision laws, and some experimental data*. Cornell University, January.

[77] W. F. R. L. D. Sturges, *W. F. Riley's L.D. Sturges's Engineering Mechanics 2nd(Second) edition(Engineering Mechanics, Statics*. Wiley, 2 edition edition ed.

[78] P. Flores, J. Ambrsio, J. C. P. Claro, and H. M. Lankarani, “Influence of the contactimpact force model on the dynamic response of multi-body systems,” vol. 220, no. 1, pp. 21–34.

[79] Y. A. Khulief, “Modeling of impact in multibody systems: An overview,” vol. 8, no. 2, pp. 021012–021012.

[80] W. Goldsmith, “Impact: The theory and physical behavior of colliding solids,”

[81] P. Ferdinand and R. Johnston Jr, *Vector Mechanics for Engineers (Dynamics)*.

[82] M. Nagurka and S. Huang, “A mass-spring-damper model of a bouncing ball,” in *Proceedings of the 2004 American control conference*, vol. 1, pp. 499–504, IEEE, 2004.

[83] L. Hill, T. Woodward, H. Arisumi, and R. Hatton, “Wrapping a target with a tethered projectile,” in *2015 IEEE International Conference on Robotics and Automation*, pp. 1442–1447, May 2015.

[84] A. Abate, R. Hatton, and J. Hurst, “Passive-dynamic leg design for agile robots,” in *2015 IEEE International Conference on Robotics and Automation*, pp. 4519–4524, May 2015.

[85] M. Noh, S.-W. Kim, S. An, J.-S. Koh, and K.-J. Cho, “Flea-inspired catapult mechanism for miniature jumping robots,” in *2012 IEEE Transactions on Robotics*, vol. 28, pp. 1007–1018.

[86] B. Lambrecht, A. D. Horchler, and R. Quinn, “A small, insect-inspired robot that runs and jumps,” in *Proceedings of the 2005 IEEE International Conference on Robotics and Automation, 2005. ICRA 2005*, pp. 1240–1245.

[87] H. Tsukagoshi, M. Sasaki, A. Kitagawa, and T. Tanaka, “Design of a higher jumping rescue robot with the optimized pneumatic drive,” in *Proceedings of the 2005 IEEE International Conference on Robotics and Automation, 2005. ICRA 2005*, pp. 1276–1283.

[88] U. Scarfogliero, C. Stefanini, and P. Dario, “Design and development of the long-jumping ”grillo” mini robot,” in *2007 IEEE International Conference on Robotics and Automation*, pp. 467–472.

[89] S. Stoeter and N. Papanikolopoulos, “Kinematic motion model for jumping scout robots,” in *2006 IEEE Transactions on Robotics*, pp. 397–402.

[90] J. Aguilar, A. Lesov, K. Wiesenfeld, and D. I. Goldman, “Lift-off dynamics in a simple jumping robot,” in *2012 Physical Review Letters*, vol. 109, p. 174301.

[91] M. A. Woodward and M. Sitti, "MultiMo-bat: A biologically inspired integrated jumpinggliding robot," in *2014 The International Journal of Robotics Research*, vol. 33, pp. 1511–1529.

[92] M. Kovac, M. Fuchs, A. Guignard, J.-C. Zufferey, and D. Floreano, "A miniature 7g jumping robot," in *2008 IEEE International Conference on Robotics and Automation. ICRA 2008*, pp. 373–378.

[93] M. Kova, M. Schlegel, J.-C. Zufferey, and D. Floreano, "Steerable miniature jumping robot," in *2009 Autonomous Robots*, vol. 28, pp. 295–306.

[94] J. Zhao, J. Xu, B. Gao, N. Xi, F. Cintron, M. Mutka, and L. Xiao, "MSU jumper: A single-motor-actuated miniature steerable jumping robot," in *2013 IEEE Transactions on Robotics*, vol. 29, pp. 602–614.

[95] M. Tolley, R. Shepherd, M. Karpelson, N. Bartlett, K. Galloway, M. Wehner, R. Nunes, G. Whitesides, and R. Wood, "An untethered jumping soft robot," in *2014 IEEE/RSJ International Conference on Intelligent Robots and Systems (IROS 2014)*, pp. 561–566.

[96] D. A. Parry and R. H. J. Brown, "The jumping mechanism of salticid spiders," in *1959 Journal of Experimental Biology*, vol. 36, pp. 654–664.

[97] S. Reuenzehn, "Mechanical design of the legs of dolomedes aquaticus - novel approaches to quantify the hydraulic contribution to joint movement and to create a segmented 3d spider model."

[98] G. Card and M. H. Dickinson, "Visually mediated motor planning in the escape response of drosophila," in *2008 Current Biology*, vol. 18, pp. 1300–1307.

[99] M. Burrows, "Kinematics of jumping in leafhopper insects (hemiptera, auchenorrhyncha, cicadellidae)," in *2007 Journal of Experimental Biology*, vol. 210, pp. 4065–4065.

[100] Y.-K. Chen, C.-P. Liao, F.-Y. Tsai, and K.-J. Chi, "More than a safety line: jump-stabilizing silk of salticids," in *2013 Journal of The Royal Society Interface*, vol. 10, p. 20130572.

[101]

[102] C. Gans, "Terrestrial locomotion without limbs," vol. 2, no. 2, pp. 167–182.

[103] M. Sato, M. Fukaya, and T. Iwasaki, "Serpentine locomotion with robotic snakes," vol. 22, no. 1, pp. 64–81.

[104] R. L. Hatton and H. Choset, *Connection Vector Fields and Optimized Coordinates for Swimming Systems at Low and High Reynolds Numbers*.

[105] S. Hirose, *Biologically inspired robots: snake-like locomotors and manipulators*. Oxford University Press.

[106] M. Mori and S. Hirose, "Three-dimensional serpentine motion and lateral rolling by active cord mechanism ACM-r3," in *IEEE/RSJ International Conference on Intelligent Robots and Systems, 2002*, vol. 1, pp. 829–834 vol.1.

[107] C. Wright, A. Johnson, A. Peck, Z. McCord, A. Naaktgeboren, P. Gianfortoni, M. Gonzalez-Rivero, R. Hatton, and H. Choset, "Design of a modular snake robot," in *IEEE/RSJ International Conference on Intelligent Robots and Systems, 2007. IROS 2007*, pp. 2609–2614.

[108] G. Goldman and D. Hong, "Considerations for finding the optimal design parameters for a novel pole climbing robot," pp. 859–866.

[109] J. Burdick, J. Radford, and G. Chirikjian, "A 'sidewinding' locomotion gait for hyper-redundant robots," in *, 1993 IEEE International Conference on Robotics and Automation, 1993. Proceedings*, pp. 101–106 vol.3.

[110] G. Chirikjian and J. Burdick, "Kinematics of hyper-redundant robot locomotion with applications to grasping," in *, 1991 IEEE International Conference on Robotics and Automation, 1991. Proceedings*, pp. 720–725 vol.1.

[111] M. Sfakiotakis and D. P. Tsakiris, "Biomimetic centering for undulatory robots," vol. 26, no. 11, pp. 1267–1282.

[112] R. L. Hatton and H. Choset, "Generating gaits for snake robots by annealed chain fitting and keyframe wave extraction," in *IEEE/RSJ International Conference on Intelligent Robots and Systems, 2009. IROS 2009*, pp. 840–845.